

ABSTRACT

Title of dissertation: NEAR-GRAZING AND NOISE-INFLUENCED
DYNAMICS OF ELASTIC CANTILEVERS
WITH NONLINEAR TIP INTERACTION FORCES

Ishita Chakraborty, 2012

Dissertation directed by: Professor Balakumar Balachandran
Department of Mechanical Engineering

Within this dissertation work, numerical, analytical, and experimental studies are conducted with macro-scale and micro-scale elastic structures in the presence of nonlinear force interactions. The specific physical systems explored within this work are an atomic force microscope (AFM) micro-cantilever and a macro-scale cantilever experiencing similar tip interaction forces as the AFM cantilever operated in tapping mode. The tip sample forces in an AFM operation are highly nonlinear, with long-range attractive forces and short-range repulsive forces. In the macro-scale case, magnetic attractive forces and repulsive forces, which arise due to impacts with a compliant surface are used to generate similar nonlinear tip interaction forces. For elastic structures subjected to off-resonance base excitations, bifurcations close to grazing events are studied in detail, and the observed nonlinear phenomena are found to be common across the considered length scales. The dynamics of the considered systems are studied with a reduced-order computational model based on Galerkin projection with a single mode approximation. Along with studies on the bifurcation

behavior, the effects of added Gaussian white noise on the system dynamics are also examined. Non-smooth system dynamics is studied by constructing local maps near the discontinuity. Period-doubling events are examined by using Poincaré maps and discontinuity mapping analysis. An important component of this dissertation research is the investigations into the effects of noise on the dynamics of these structures. Experimental and numerical efforts are used to examine the stochastic dynamics of the cantilever structures when a random component is added to the harmonic input. The noise effects are studied when the excitation frequency is close to a system resonance as well as when it is off-resonance. An analytical-numerical method with moment evolution equations is used to study the effects of noise. The effects of noise on contact and adhesion phenomena are explored. Through this dissertation work, the importance of considering noise-influenced dynamics in micro-scale applications such as AFM operations is illustrated. In addition, this work helps shed light on universality of nonlinear phenomenon across different length scales.

NEAR-GRAZING AND NOISE-INFLUENCED
DYNAMICS OF ELASTIC CANTILEVERS WITH
NONLINEAR TIP INTERACTION FORCES

by

Ishita Chakraborty

Dissertation submitted to the Faculty of the Graduate School of the
University of Maryland, College Park in partial fulfillment
of the requirements for the degree of
Doctor of Philosophy
2012

Advisory Committee:

Professor Balakumar Balachandran, Chair and Advisor

Professor Amr Baz, Department of Mechanical Engineering

Assistant Professor Nikhil Chopra, Department of Mechanical Engineering

Assistant Professor Santiago Solares, Department of Mechanical Engineering

Professor Rajarshi Roy, Department of Physics and IPST (Dean's Representative)

© Copyright by
Ishita Chakraborty
2012

Acknowledgments

First of all, I want to express my sincere gratitude towards my advisor Prof. Balakumar Balachandran for his insightful guidance, patience, and support throughout my Ph.D. research work. His ideas and inputs have been most important for the completion of this dissertation.

I want to thank Professors Amr Baz, Rajarshi Roy, Santiago Solares, and Nikhil Chopra for serving in my committee. I would also like to thank Prof. Santiago Solares and Dr. Gaurav Chawla for helping me with the AFM experiments.

The financial support for this research received through National Science Foundation CMMI-0800741 is gratefully acknowledged. I am also grateful for the support provided by the Graduate School through the Ann G. Wylie Dissertation Fellowship during the Fall semester of 2011.

I want to thank all the members of the Dynamics and Vibrations Group for their help, support, and friendship. The atmosphere of learning, cooperation, and fun within the research group has made my journey a truly memorable one.

I will take this opportunity to thank my family for always being extremely supportive in all my endeavors. Finally, I would like to thank Baidurja for being such a huge support throughout these years. His constant encouragement, patience, and help have been my greatest source of strength.

Table of Contents

List of Tables	v
List of Figures	vi
1 Background and Motivation	1
1.1 Introduction	1
1.2 Literature review	5
1.3 Dissertation objectives	8
1.4 Contributions	9
1.5 Organization of dissertation	10
2 Dynamics of Elastic Cantilevers for Off-resonance Excitations	12
2.1 Tip-sample forces in dynamic AFM operations	13
2.2 Macro-scale experimental arrangement	16
2.2.1 Tip interaction forces	16
2.2.2 Experimental arrangement and results	19
2.3 Computational modeling and numerical results	23
2.3.1 Model development	25
2.3.2 Nondimensionalization and discretization	26
2.3.3 Numerical results	32
2.4 Summary	34
3 AFM Experimental and Numerical Studies	35
3.1 Dynamic mode operation of AFM	36
3.2 Experimental arrangement and observations	37
3.3 Numerical studies	41
3.4 Operations with soft samples	49
3.5 Summary	50
4 Discontinuity Induced Bifurcations	51
4.1 Piecewise nonlinear force model	52
4.2 Discontinuity maps near grazing	57
4.3 Experimental study of stability	67
4.4 Summary	70
5 Effects of Noise	72
5.1 Experimental studies and results	75
5.2 Numerical studies and results	77
5.3 Analytical framework for stochastic dynamics	79
5.3.1 Stochastic differential equation	82
5.3.2 Fokker-Planck equation	82
5.3.3 Moment evolution equations	83
5.4 Numerical studies with the moment evolution equations	88

5.5	Application to atomic force microscopy	90
5.6	Analysis with moment equations	95
5.7	Numerical solutions of the moment evolution equations	99
5.8	Summary	101
6	Effects of Noise on Sticking Motions	103
6.1	Experimental studies	104
6.2	Numerical studies	108
6.3	Analytical framework and numerical results	113
6.4	Summary	118
7	Summary and Recommendations for Future Work	119
7.1	Summary	119
7.2	Recommendations for future work	121
A	Computational Modeling with Multiple Modes	123
B	Derivation of Moment Evolution Equations	125
C	Matlab Codes	128
C.1	Representative Matlab code for macro-scale system	128

List of Tables

2.1	Tip-sample properties	14
2.2	Simulation parameter values.	29
3.1	Simulation parameter values.	42
4.1	Nondimensional parameter values used in simulations	56
6.1	Simulation parameter values.	112

List of Figures

1.1	Schematic of an atomic force microscope. The micro-cantilever is generally a few hundred μm long.	2
1.2	Variation of representative tip sample force with oscillation of the cantilever.	3
2.1	Different models to represent tip-sample interaction force variation with distance between the tip and the sample - (a) combination of van der Waals and Derjaguin-Muller-Toporov forces, (b) force derived from Lennard-Jones potential, and (c) piecewise linear force profile.	13
2.2	Representative tip-sample forces in an AFM operation.	15
2.3	(a) Tip-surface arrangement in macro-scale. (b) Tip-sample arrangement in micro-scale AFM.	16
2.4	Variation of nonlinear force with the distance between the tip and surface for the macro-scale system.	17
2.5	Schematic of experimental arrangement at macro-scale.	18
2.6	Details at the tip in the context of the experimental arrangement.	19
2.7	Experimentally obtained diagram of qualitative changes on Poincaré section for excitation frequencies higher than the system's first natural frequency. Here, the scalar control parameter is the excitation frequency. The Poincaré sections are constructed by using the excitation frequency as the clock frequency.	20
2.8	Experimentally obtained cantilever tip displacement history for excitation at 15.4 Hz: (a) unconstrained motions (motions without contact) and (b) constrained motions.	21
2.9	Experimentally obtained response spectra for excitation at 15.4 Hz: (a) unconstrained motions (motions without contact) and (b) constrained motions.	22
2.10	Experimentally obtained diagram of qualitative changes on Poincaré section when excitation frequency is 2.24 times the system's first natural frequency. Here, the scalar control parameter is the distance between the tip and sample. A transition to aperiodic motion from the period-doubled response at near-grazing condition is observed as the separation between the cantilever tip and the compliant material is decreased.	23
2.11	Experimentally obtained phase portrait for aperiodic response.	24
2.12	Plot of $\ln C_r$ versus $\ln r$ for aperiodic data for different embedding dimensions.	24
2.13	Model of a base excited cantilever beam subjected to impacts at the free end.	25
2.14	Numerically obtained phase portraits for the excitation frequency of 15.4 Hz. Unconstrained motions correspond to the smaller orbit and constrained motions correspond to the larger orbit.	29

2.15	Experimentally obtained phase portraits for the excitation frequency of 15.4 Hz. Unconstrained motions correspond to the smaller orbit and constrained motions correspond to the larger orbit.	30
2.16	Response spectra for unconstrained motions (top) and constrained motions (bottom) at 15.4 Hz.	30
2.17	Numerically obtained phase portraits for excitation frequency of 16.1 Hz. Unconstrained motions correspond to the smaller orbit and constrained motions correspond to the larger orbit.	31
2.18	Experimentally obtained phase portrait for excitation frequency of 16.1 Hz. Unconstrained motions correspond to the smaller orbit and constrained motions correspond to the larger orbit.	31
3.1	Snapshot of the experimental arrangement located in the AFM lab at the Department of Mechanical Engineering at the University of Maryland. An Asylum Research MFP3D AFM is connected to a Tektronix signal analyzer to locate the period-two response for near-grazing impacts.	37
3.2	Power spectrum of the response of the cantilever tip when the tip makes near-grazing contact with the sample. The peak located at half the excitation frequency is indicative of the period-two response of the cantilever.	38
3.3	Power spectrum of the response of the cantilever tip when the excitation amplitude is higher, for the same excitation frequency as used in Fig. 3.2. Higher harmonics are seen for harder impacts.	39
3.4	Experimentally obtained phase portrait for Si cantilever and Si(100) sample combination, before the tip makes grazing impacts with the sample. The vertical line signifies the location of the sample.	40
3.5	Experimentally obtained period-two phase portrait for Si cantilever and Si(100) sample combination, after the tip makes grazing impacts with the sample. The vertical line signifies the location of the sample	41
3.6	Tip-sample force curve for a Si cantilever and a Si(100) sample. . . .	43
3.7	Phase portrait of the AFM cantilever tip when the tip does not make intermittent contact with the sample. The solid vertical line represents the location of the sample.	44
3.8	Response spectrum of the cantilever tip response when the tip is not making contact with the sample. A single peak is seen at the frequency of excitation.	45
3.9	Force on the cantilever tip when the tip is not making contact with the sample. The forces are always attractive due to long-range forces.	45
3.10	Phase portrait of the AFM cantilever tip when the tip makes intermittent contact with the sample. The solid vertical line represents the location of the sample.	46
3.11	Response spectrum of the cantilever tip response when the tip makes contact with the sample. A peak is seen at half the frequency of excitation.	46

3.12	Force on the cantilever tip when the tip is making contact with the sample. Both attractive and repulsive interaction forces come into play.	47
3.13	Force curve obtained from molecular dynamic simulations (Solares, 2007).	47
3.14	Tip-sample force profiles and the location of the maximum repulsive force for contact is presented in (a), (d), and (g). Response spectra are presented in (b), (e), and (h). The corresponding phase portraits are presented in (c), (f), and (i).	48
4.1	Comparison of force profiles in macro-scale system.	54
4.2	Comparison of force profiles in micro-scale AFM operation.	54
4.3	Illustration of grazing bifurcation. Orbits A , B and C are representative system responses, when a scalar control parameter is quasi-statically varied.	57
4.4	Illustration of discontinuity map near the grazing point.	59
4.5	(a)Illustration of discontinuity map near the grazing bifurcation point for macro-scale system. (b)Illustration of discontinuity map near the grazing bifurcation point for micro-scale system.	66
4.6	Experimentally obtained phase portraits for the perturbed system (dashed line), and the unperturbed system (solid line): (a)unconstrained motion and (b) constrained motion. Iterations of Poincaré map: (c) unconstrained motion and (d) constrained motion. The experimentally obtained points are connected by solid lines and the points obtained from the linear curve fit are joined by dashed lines.	68
5.1	Potential sources of noise in an AFM system, which can be attributed to the controller, optical system, or a fabrication irregularity. Noise effects are important to understand due to the presence of the double-well potential in the cantilever-sample system.	72
5.2	(a) Harmonic input from the shaker, (b) response phase portrait of the cantilever's tip, and (c) response spectrum. A single peak can be seen at the excitation frequency.	77
5.3	(a) Combined harmonic and noise input from the shaker, (b) response phase portrait, and (c) response spectrum. A dominant peak at half the excitation frequency can be seen along with a peak at the excitation frequency.	78
5.4	The schematic of the elastic structure and the tip sample arrangement.	79
5.5	(a) Harmonic excitation input from the shaker, (b) response phase portrait of cantilever tip, and (c) response spectrum. A single peak can be seen at the excitation frequency.	80
5.6	(a) Combined harmonic and noise input from the shaker, (b) response phase portrait, and (c) response spectrum. A dominant peak at half the excitation frequency can be seen along with a peak at the excitation frequency.	81

5.7	(a) Comparison between the combination of the magnetic attractive and DMT forces, and the assumed force profile. (b) Expanded view of the comparison for the boxed portion in Fig. 5.7(a)).	84
5.8	Comparisons of the evolutions of the mean displacement for different moment equation truncations.	87
5.9	Evolution of mean value of displacement with time when $\sigma = 0$. The solid line at the bottom signifies the location of the compliant material surface.	88
5.10	Evolution of mean value of displacement with time when $\sigma = 0.0004$. The solid line at the bottom signifies the location of the compliant material surface.	89
5.11	Evolution of mean value of displacement with time when $\sigma = 0.0010$. The solid line at the bottom signifies the location of the compliant material surface.	89
5.12	Variation of the potential function for the considered the tip-sample combination with the radius of the tip R	91
5.13	Potential function for AFM cantilever. A magnified view of the second potential well is shown on the right.	92
5.14	(a) Phase portrait of the cantilever tip response when there is no noise addition in the base input. (b) The response spectrum. The vertical line at 100 nm corresponds to the location of the sample in the phase portrait. A dominant peak at the excitation frequency can be seen in the response spectrum.	93
5.15	(a) Phase portrait of the cantilever tip response when there is noise added to the base input. The signal to noise ratio is 100. (b) The response spectrum. The vertical line at 100 nm corresponds to the location of the sample. A dominant peak at one half of the excitation frequency can be seen in the response spectrum.	94
5.16	(a) Attractive and repulsive force interaction in the van der Waals and DMT force combination. (b) Comparison of the assumed force profile with tip-sample force given in (a) near the contact point.	96
5.17	Comparisons of the evolutions of the mean displacement for different truncations of moment evolution equations.	98
5.18	Time evolution of the first moment (mean displacement) for $\sigma = 0$. The solid line at the bottom represents the sample location.	99
5.19	Time evolution of the first moment (mean displacement) for $\sigma = 0.03$. The solid line at the bottom represents the sample location.	100
5.20	Time evolution of the first moment (mean displacement) for $\sigma = 0.04$. The solid line at the bottom represents the sample location.	100
6.1	Experimental arrangement. Details of the tip arrangement are shown in the inset.	105
6.2	(a) Purely harmonic input excitation from the shaker. (b) Snapshot of the experimental system depicting the tip magnet sticking with the base magnet.	106

6.3	(a) Representative combination of white noise and harmonic component used for base excitation in the experiments. SNR for this input is 50.64. (b) Cantilever tip displacement showing intermittent contact between the tip and the base magnet. (c) Response spectrum of the displacement data showing a peak at the excitation frequency. . .	107
6.4	Variation of nonlinear tip interaction forces with the cantilever tip displacement.	108
6.5	Variation of potential function with the cantilever tip displacement. The ellipse and dotted line denote the relative response locations for a harmonic excitation and a combination of harmonic excitation and noise, respectively.	109
6.6	Numerically obtained displacement data for a purely harmonic excitation. The dashed horizontal line represents the base magnet location.	110
6.7	Numerically obtained displacement data when noise of SNR 51.00 is added to a harmonic base excitation. The dashed horizontal line represents the base magnet location.	111
6.8	Response spectrum for the numerically obtained displacement data given in Fig. 6.7.	111
6.9	Comparison of the assumed force profile with the DMT and magnetic attractive force profile.	114
6.10	Evolution of the first moment with time when $\sigma = 0.00$. The solid horizontal line represents the base magnet location.	116
6.11	Evolution of the first moment with time when $\sigma = 0.06$. The solid horizontal line represents the base magnet location.	117
A.1	Comparison of displacements with a single mode and a two-mode approximation for computational studies in macro-scale.	124
A.2	Comparison of velocities with a single mode and a two-mode approximation for computational studies in macro-scale.	124

Chapter 1

Background and Motivation

In this chapter, background for the research undertaken in this dissertation is presented. Along with a presentation of the existing literature, existing gaps in the literature are identified and the issues to be addressed in the present effort are outlined.

The physical problem of interest for this work is the dynamics of cantilever structures subjected to the influence of nonlinear attractive-repulsive forces at its tip. Specific attention is paid to address the near-grazing dynamics related to off-resonance excitation frequencies and to study the effects of noise on system dynamics. This problem has relevance to tapping mode atomic force microscope (AFM) operation. A motivation is to develop a fundamental understanding of the nonlinear dynamics of tapping mode AFM cantilevers when they are operated at frequencies away from the system's fundamental frequency, and to explore the effects of stochastic components in macro-scale and micro-scale applications.

1.1 Introduction

Since the invention of Atomic Force Microscope (AFM) by Binnig, Quate, and Gerber (1987), it has become a useful tool for material characterization. AFM has different modes of operation, such as the contact mode (the tip is always in contact

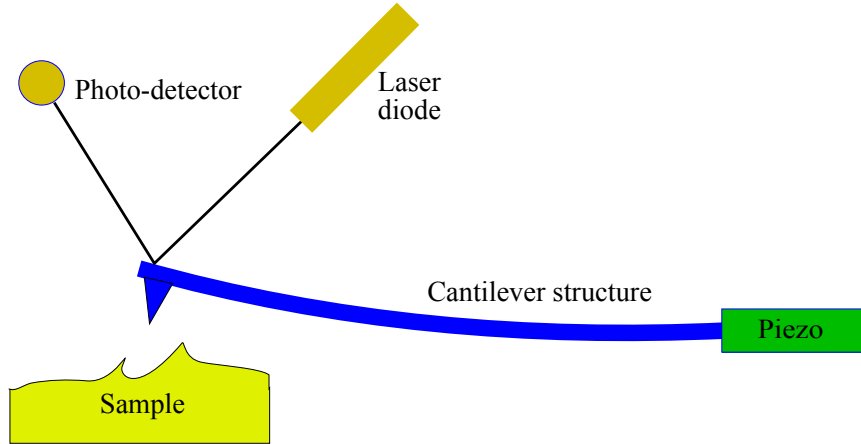


Figure 1.1: Schematic of an atomic force microscope. The micro-cantilever is generally a few hundred μm long.

with the sample), non-contact mode (the tip oscillates with a small amplitude over the sample without making contact with it), and intermittent-contact mode (where the tip oscillates over the sample and makes intermittent contact with it).

In dynamic mode AFM, a cantilever tip approaches and retracts from the sample, when the system is excited at resonance. *Tapping mode AFM* is a dynamic force microscopy method (e.g., Garcia and Perez, 2002) where the micro-cantilever is excited at a fixed frequency (usually near the first resonance frequency), and the oscillation amplitude is used as a feedback parameter to image the sample topography. The cantilever is excited in a base excitation mode using a piezoelectric actuator, which is attached below the cantilever base or in a non-contact excitation mode by directly exciting the tip by applying an oscillating magnetic field to a magnetized cantilever. The displacement of the beam tip is recorded by using a laser diode and photo-detector combination, as illustrated in Fig. 1.1, which contains

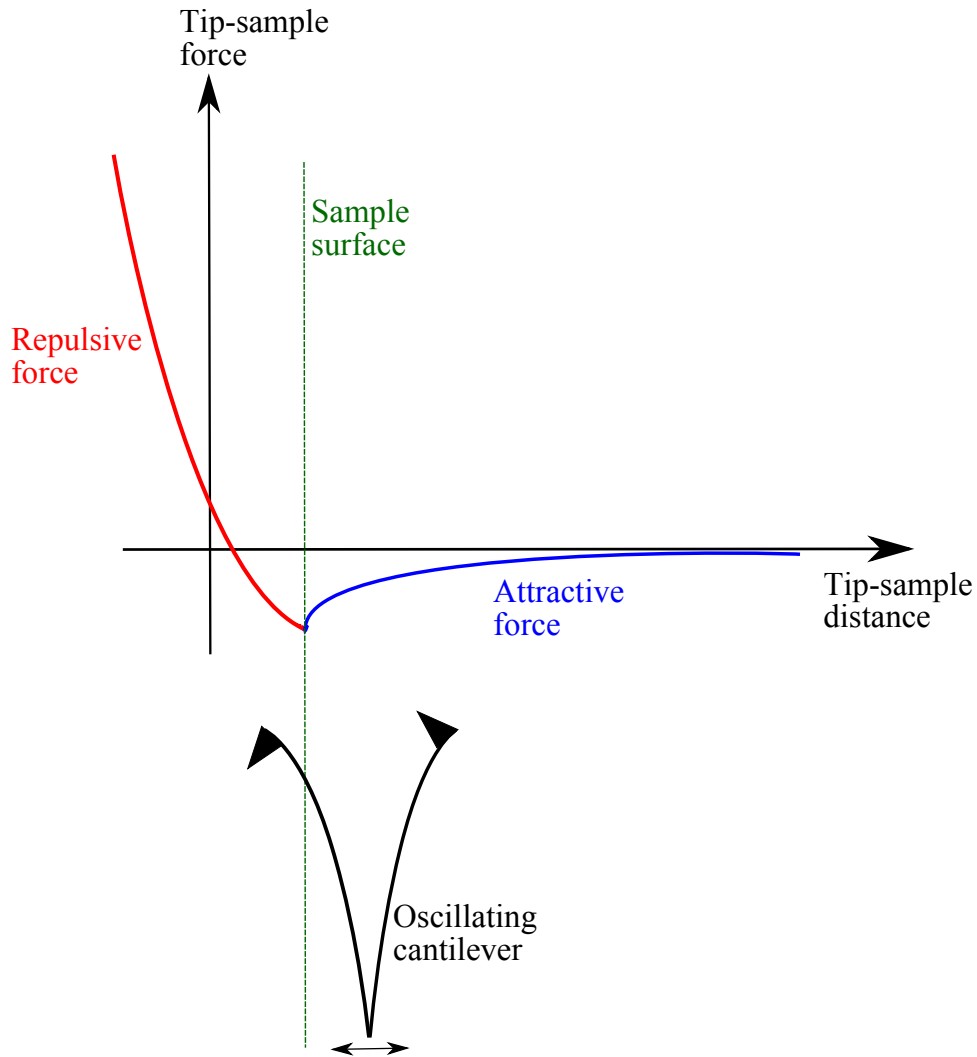


Figure 1.2: Variation of representative tip sample force with oscillation of the cantilever.

schematic of the tip-sample assembly. The distance between the sample and the cantilever is varied to maintain a set-point amplitude of the cantilever. Thus, the surface topography can be obtained from the variation of distance between the tip and the sample. The tip-sample interaction force assumes significant importance as the amplitude of the cantilever response depends on it.

The tip-sample forces associated with tapping-mode AFM cantilevers are inherently nonlinear. The tip-sample interaction forces are attractive when the distance between the tip and the sample is large, and the forces become repulsive as the tip makes contact with the sample. The variation of a representative tip-sample force with the tip-sample distance is shown in Fig. 1.2. The forces relevant to AFM arise from different intermolecular and surface forces. In previous studies, the tip-sample forces have been characterized by using Lennard Jones potential (Rutzel, Lee, and Raman, 2003), piecewise linear forces (Dankowicz, Zhao, and Misra, 2007), and van der Waals attractive forces and Derjaguin-Muller-Toporov contact forces (Lee, Howell, and Reifenberger, 2003). Due to the strong distance-dependent nonlinear forces, various nonlinear phenomena such as bistability, saddle-node bifurcations, period-doubling, chaotic oscillations, and so on, have been observed in tapping mode AFM (Dankowicz, 2006; Raman, Melcher, and Tung, 2008).

An impact of the cantilever tip with the sample surface can be characterized as “soft” or “hard” impacts. A special type of bifurcations arise when these impacts have zero-speed or are of “grazing” type. Grazing phenomenon and the bifurcations associated with it have been widely studied over the past decade. Period-adding, chaotic, or periodic qualitative changes have been observed in post-grazing states. In the first part of this dissertation, the author concentrates on the period-doubling bifurcations due to grazing incidence in the micro-scale AFM system and a similar macro-scale system. The scalability and the possible utilization of nonlinear phenomenon to reduce the repulsive forces in AFM operations is studied in detail. In the next part, the effects of adding Gaussian white noise to the system is studied

through experimental, numerical, and analytical efforts. The existing literature on this subject is briefly summarized in the next section.

1.2 Literature review

Impacting structures can be found in various macro-scale systems including impact dampers, gears, cutting tools, and micro-scale systems such as tapping mode atomic force microscope and shock sensors. Elastic structures undergoing impacts have been extensively studied over the past several decades (see Shaw and Balachandran, 2008). Shaw and Holmes (1983a,b) studied the response of a piecewise linear, sinusoidally forced impact oscillator for various values of the forcing frequency. A special situation arises during zero-speed incidence or “grazing” impacts. Nordmark (1991) treated the grazing dynamics of an impact oscillator by constructing a local map. When a periodic orbit comes close to experiencing a grazing impact during the quasi-static variation of a scalar control parameter, it has been shown that a special type of qualitative change takes place in the motion. Stensson and Nordmark (1994) investigated the effects of low-speed impacts through experimental and numerical efforts. Chin, Ott, Nusse, and Grebogi (1994) studied various types of grazing bifurcations for a simple impactor system in the presence of friction. Hunt and Sarid (1998) modeled tapping-mode atomic force microscope operations by using a grazing impact oscillator. By using local maps, Molenaar, de Weger, and van de Water (2001) studied the period-adding mechanism in the response of an impact oscillator. For near-grazing impacts in an impact oscillator, de Weger, van de Water, and

Molenaar (2000) conducted an experimental investigation into the period-adding phenomenon. The applicability of these analyses to atomic force microscope was reported by van de Water and Molenaar (2000). Dankowicz and Nordmark (2000) derived a local discontinuity map in the neighbourhood of a grazing bifurcation. di Bernardo, Budd, and Champneys (2001a,b) derived a normal form map for grazing and corner-collision bifurcations. Following Feigin's earlier work, di Bernardo, Feigin, Hogan, and Homer (1991) analyzed atypical bifurcations during border-collision impacts. An experimental study of an impacting oscillator was presented by Ing, Pavlovskaja, Wiercigroch, and Banerjee (2008), and in this work, the stability of grazing orbits were determined by using an experimental approach.

When the excitation frequency is away from the first natural frequency of the system, multiple period-doubling windows can occur as reported in the study by Balachandran (2003) for an elastic structure subjected to harmonic and aharmonic impactor motions. For soft impacts with an elastic structure, corner-collision bifurcations were studied by constructing a discontinuity map and period-doubling bifurcations close to the corner-collision was reported by Long, Lin, and Balachandran (2008). Dick, Balachandran, Yabuno, Numatsu, Hayashi, Kuroda, and Ashida (2009) observed period-doubling bifurcations close to grazing impacts in a macro-scale experimental system and in an atomic force microscope for an off-resonance excitation. This period doubling can be used to identify near-grazing impacts to reduce the repulsive tip-sample forces in tapping mode operations with soft materials. In previous efforts of the research group the dissertation author is associated with, the beneficial use of various nonlinear phenomena in macro-scale and micro-scale

structures has been studied (Dick, 2007).

As mentioned earlier, nonlinear phenomena associated with dynamic mode AFM has received considerable attention over the past decade (Hu and Raman, 2006; Lee, Howell, Raman, and Reifenberger, 2002; Basak and Raman, 2007; Hashemi, Dankowicz, and Paul, 2008; Yagasaki, 2004) when the excitation frequency is at the first natural frequency of the cantilever. There has been relatively less work on off-resonance excitations of the cantilever. In the efforts of Kowalewski and Legleiter (2006) and Legleiter (2009), the effects of exciting the cantilever far below its first natural frequency on the tip-sample forces and imaging quality have been explored.

Another aspect of this dissertation effort is to explore the effects of added noise on the dynamics of base excited elastic cantilevers subjected to nonlinear force interactions in macro-scale and micro-scale. The effects of noise on dynamic mode AFM operations has only received limited attention. In AFM cantilever operations, thermal fluctuations are a major source of noise. Butt and Jaschke (1995) calculated the thermal noise in contact mode AFM. Stark, Drobek, and Heckl (2001) determined the thermal noise associated with the free vibration of a V-shaped cantilever structure by using the finite element method. In the works of Basso, Dahleh, Mezić, and Salapaka (1999) and Rajaram, Salapaka, Basso, and Dahleh (2000), the stochastic resonance phenomenon has been explored in the context of dynamic mode AFM operations. It is noted that the tip-sample interaction potential associated with an elastic cantilever has a double-well form. The addition of noise to the system can move the system from one potential well to the other. It is well recognized that, stochastic effects, such as those arising from thermal sources and

fabrication irregularities, assume significance at the micro-scale and nano-scale. In the efforts of Ramakrishnan and Balachandran (2010), it has been discussed that the formation of intrinsic localized modes in micro-scale resonator arrays can be influenced by adding Gaussian white noise to a deterministic and periodic excitation. Stochastic effects arising from different sources can cause a significant change in the dynamics of micro-scale operations such as AFM operations.

1.3 Dissertation objectives

In the current effort, the focus is on maintaining “grazing” contact between the cantilever tip and the sample to reduce the tip-sample interaction forces. To study the effects of nonlinear tip-sample interactions on a vibrating cantilever, a macro-scale experimental arrangement has been constructed to study the cantilever-tip response for off-resonance as well as resonance excitations. To further understand near-grazing dynamics, the period-doubling bifurcation is studied by constructing a zero-time discontinuity map. The findings from the macro-scale studies are applied to micro-scale AFM operations. The effects of noise on the dynamics are analyzed through a combination of experimental, numerical, and analytical studies.

The overall goal of this work is to understand the response of an elastic structure subjected to nonlinear interaction forces at its tip and use this understanding to realize desired dynamics of physical systems at the macro-scale and micro-scale. Specific objectives include the following:

1. Experimentally and numerically study the dynamics of elastic structures, with

attention to different combinations of attractive and repulsive forces.

2. For soft impacts, study the bifurcations close to grazing impacts through analysis and use these bifurcations to explain qualitative changes observed in experiments and numerical studies.
3. Apply the findings to tapping mode atomic force microscopy with the goal of reducing the tip-sample repulsive force for non-destructive characterization of soft samples.
4. Experimentally and numerically study the effects of added Gaussian white noise on the system of interest and determine whether noise can be utilized in a beneficial manner.

While the focus of the current work is directed towards tapping-mode atomic force microscopy, extensions to other micro-scale applications are conceivable.

1.4 Contributions

The specific contributions of this dissertation can be listed as the following:

1. Understanding micro-scale system dynamics using macro-scale systems: A novel macro-scale experimental arrangement has been designed that has the similar tip-sample interaction forces as the micro-scale AFM operated in tapping mode.
2. Grazing and near-grazing dynamics: Bifurcations close to grazing impacts have been studied and characterized for off-resonance excitations in both the

macro-scale system and the micro-scale AFM. It is illustrated as to how period-doubling bifurcations can be utilized to identify grazing contact and how operating an AFM cantilever at a grazing point can reduce the repulsive tip-sample forces. A method based on nonlinear dynamics based operation of AFM is proposed.

3. Modeling and analysis: A reduced-order model is developed to understand the dynamics of systems at different length scales. A single model could be used to study these different systems through nondimensional parameters. The discontinuity induced bifurcations are studied by local maps by zero-time discontinuity mapping (ZDM) technique.
4. Noise influenced dynamics: The effects of noise are studied by adding noise in the systems under consideration. Numerical and experimental efforts are directed towards understanding the effects of noise on contact and adhesion related phenomena. Fokker-Planck equations are derived to study the stochastic dynamics of base-excited cantilevers with nonlinear force interactions and better understand noise-influenced dynamics. These equations are solved by using a semi-analytical method involving moment evolution equations.

1.5 Organization of dissertation

The rest of the dissertation is organized as follows. In Chapter 2, an overview of the dynamics of elastic cantilevers for off-resonance excitations is presented. First, the macro-scale experimental arrangement is described, followed by the obtained ex-

perimental results. The model development is described in detail for the macro-scale cantilever-sample combination. The numerical results obtained from this model are compared with the experimental results. In Chapter 3, the experimental and numerical studies conducted for the micro-scale AFM system are presented. The dynamics of micro-scale AFM is analyzed with the same computational model developed for analyzing the macro-scale system. In Chapter 4, the discontinuity induced bifurcations are studied through the construction of local Poincaré maps close to the point of grazing incidence. The constructed maps are studied for both of the systems. In Chapter 5, the studies on effects of noise are presented. Experimental and numerical studies conducted on the dynamics of systems in the presence of noise are documented. Fokker-Planck equations are derived for these systems. Moment evolution equations are derived from the Fokker Planck equations to study the stochastic dynamics. In Chapter 6, the noise-induced dynamics of an elastic cantilever in the presence of high attractive forces is presented. Summary of the dissertation work and recommendations for future directions are presented in Chapter 7. Appendices related to the dissertation work are included at the end.

Chapter 2

Dynamics of Elastic Cantilevers for Off-resonance Excitations

In this chapter, the experimental and numerical studies conducted with the macro-scale system are presented and discussed. Some of the material presented in this chapter has been published by the dissertation author (Chakraborty and Balachandran, 2009, 2011a). In order to study the dynamics of AFM cantilevers subjected to off-resonance (atypical) base excitations and near-grazing impacts, a macro-scale system, inspired by the micro-scale AFM system, is studied.

The reasons for studying the dynamics of a macro-scale system can be summarized as follows:

1. The macro-scale experimental set-up serves as a vehicle to better understand the nonlinear phenomena possible at the micro-scale. Further, a study of different phenomena in the macro-scale system can provide an idea on what to expect in an AFM system.
2. The macro-scale system provides a flexibility to control the experimental parameters, which would be difficult to achieve in an actual AFM system.

In order to make a macro-scale model of an AFM cantilever operating in tapping mode, a full scale cantilever with approximately $1000\times$ the dimension of a typical AFM cantilever is selected. The selected material for this cantilever is Aluminum, since a soft cantilever is needed to study the response for off-resonance

excitations. The attractive-repulsive force combination is engineered through a combination of attracting magnets and intermittent periodic impacts.

Tip-sample forces in micro-scale AFM are described in the next section. This is followed by a description of the macro-scale experimental system and experimental results. The model developed to study the system is presented in the Section 2.2. The numerically obtained results are presented next and they are compared with the experimental data.

2.1 Tip-sample forces in dynamic AFM operations

The tip-sample forces in the tapping mode operation of an AFM involves a long-range attractive force and a short-range repulsive force. These forces are electro-magnetic in nature (see Garcia and Perez, 2002). As discussed in Section 1.2, the tip-sample forces have been modeled in a few different ways in the literature.

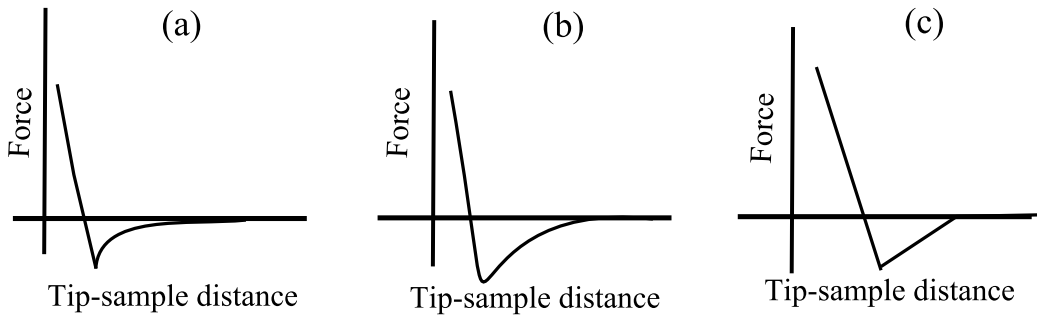


Figure 2.1: Different models to represent tip-sample interaction force variation with distance between the tip and the sample - (a) combination of van der Waals and Derjaguin-Muller-Toporov forces, (b) force derived from Lennard-Jones potential, and (c) piecewise linear force profile.

Some of the different models to capture the nonlinear forces are shown in Fig. 2.1. The primary forces acting between the AFM tip and sample are attractive van der Waals forces due to constructive correlation between the tip and the sample atoms, and the forces become repulsive due to Pauli and ionic-repulsive type forces. In this work, the selected model used to represent the tip-sample forces are a combination of van der Waals forces and DMT contact forces (Derjaguin, Muller, and Toporov, 1975). For a simple approximation of a spherical tip and a flat sample, the van der Waals forces can be described by

$$F_{vdw}(z) = -\frac{HR}{6z^2},$$

where H is the Hamaker constant, R is the radius of the tip, and z is the instantaneous tip-sample distance. This expression is applicable for $z > a_0$ where a_0 is the intermolecular separation between the tip and the sample atoms. The short-range repulsive forces are modeled by accounting for the contact between the two surfaces, since there are a number of atoms, which gives rise to contact between

Table 2.1: Tip-sample properties

Property	Value
Tip radius (R)	20 nm
Cantilever Young's Modulus (E_t)	176 GPa
Effective Young's Modulus (E^*)	10.4 GPa
Hamaker Constant (H)	$2.96 \times 10^{-19} J$
Intermolecular distance (a_0)	0.2 nm

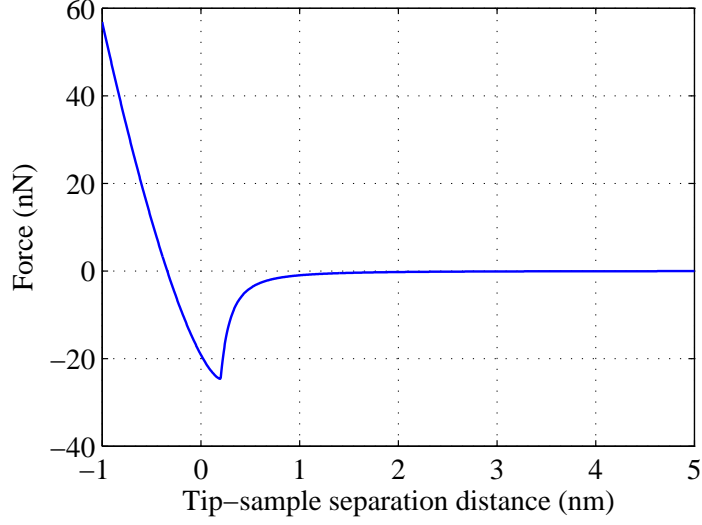


Figure 2.2: Representative tip-sample forces in an AFM operation.

the two surfaces. The repulsive forces can be described by various models including the Johnson-Kendall-Roberts (JKR) or Derjaguin-Muller-Toporov (DMT) models. In this work, it is assumed that the repulsive interactions take place in accordance with the DMT model, where for $z \leq a_0$, the forces are governed by

$$F_{DMT}(z) = -\frac{HR}{6a_0^2} + \frac{4}{3}E^*\sqrt{R}(a_0 - z)^{\frac{3}{2}}.$$

Here, E^* , the effective elasticity of the tip and the sample is given by

$$\frac{1}{E^*} = \frac{1 - \nu_t^2}{E_t} + \frac{1 - \nu_s^2}{E_s}$$

where ν_t and ν_s are the Poisson's ratios and E_t and E_s are the tip Young's Modulus and sample Young's Modulus, respectively. Next, taking into account both the attractive and the repulsive force components, the tip-sample interaction force can be described by

$$F_{vdw}(z) = -\frac{HR}{6z^2} \quad \text{for } z > a_0$$

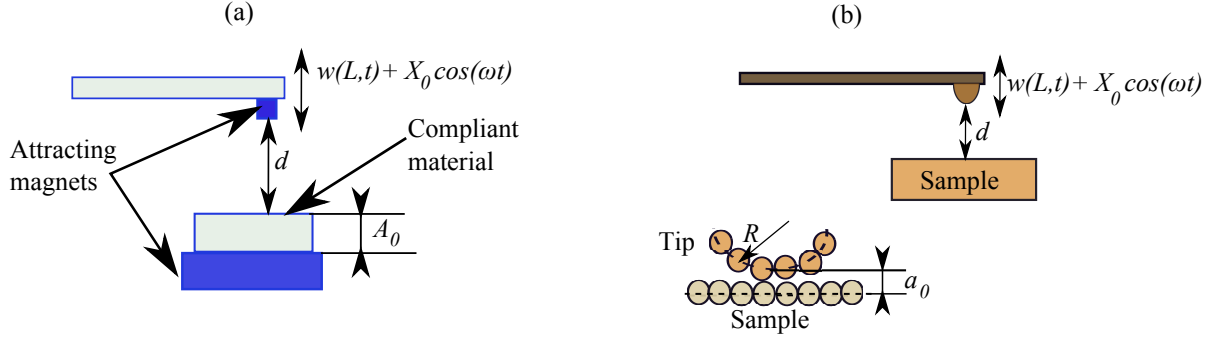


Figure 2.3: (a) Tip-surface arrangement in macro-scale. (b) Tip-sample arrangement in micro-scale AFM.

$$F_{DMT}(z) = -\frac{HR}{6a_0^2} + \frac{4}{3}E^*\sqrt{R}(a_0 - z)^{1.5} \quad \text{for } z \leq a_0 \quad (2.1)$$

By using the parameter values for a Si micro-cantilever and an HOPG sample given in Table 2.1, the force-distance curve shown in Fig. 2.2 has been generated. To study the effects of this type of nonlinear tip-interaction forces on a vibrating micro-cantilever, a macro-scale experiment is designed with a similar type of attractive and repulsive tip interaction forces.

2.2 Macro-scale experimental arrangement

2.2.1 Tip interaction forces

A similar type of attractive repulsive force combination as discussed in section 2.1 is engineered at the macro-scale with a combination of magnets to generate the attractive forces and a compliant surface to facilitate soft contact. A small magnet is mounted at the tip of a macro-scale cantilever beam, which is base excited by a shaker. The magnetic tip periodically comes into contact with a soft surface, below

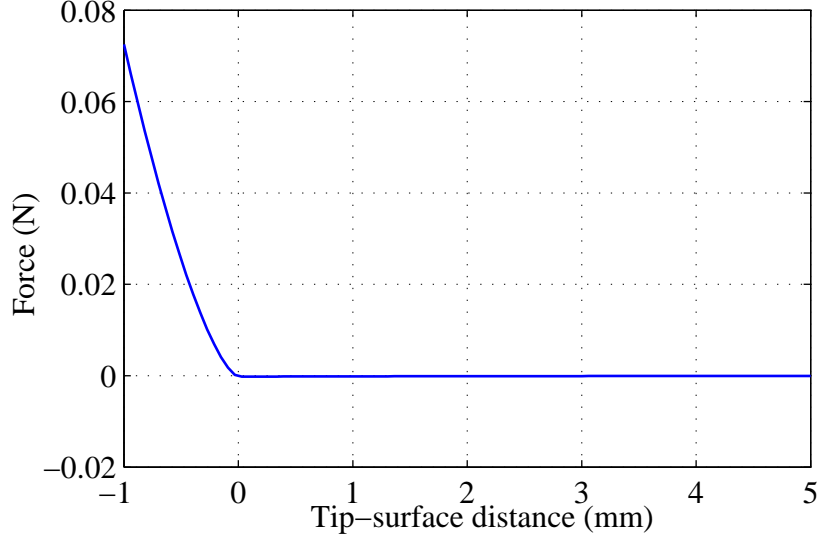


Figure 2.4: Variation of nonlinear force with the distance between the tip and surface for the macro-scale system.

which another magnet of opposite polarity is located (see Fig. 2.3(a)). These two magnets produce a $1/r^2$ type attractive force similar to the van der Waals force at the micro-scale. The soft impacts of the tip with the compliant material is modeled by using the DMT model, and hence, similar to Eq. (2.1), the tip interaction force at the macro-scale can be expressed as shown in Eq. (2.2)

$$F(z) = \begin{cases} -\frac{K_M}{(z+d+A_0)^2} & \text{for } d+z > 0 \\ -\frac{K_M}{(A_0)^2} + K_E(-d-z)^{1.5} & \text{for } d+z \leq 0 \end{cases} \quad (2.2)$$

where K_M and K_E are the constants associated with the magnetic and elastic forces, respectively. A_0 is the thickness of the compliant material, z is the displacement of the cantilever tip, and d is the initial distance between the cantilever tip and the compliant surface. The magnetic constant K_M can be expressed as

$$K_M = \mu m_1 m_2,$$

where μ is the permeability of the air, and m_1 and m_2 are the magnetic pole strengths. Here, the effects due to the shape and size of the magnets are ignored. K_E is expressed in a similar fashion as in Section 2.1. In the macro-scale system, the assumed nonlinear tip interaction has similar characteristics as the tip-sample forces in the micro-scale system. The repulsive force comes into play as the cantilever tip makes contact with the compliant surface. The tip-sample force curve at the macro-scale is displayed in Fig. 2.4 for representative values of the constants (K_M , K_E and d), which are also used later in the numerical simulations. The values of these constants are provided in Table 2.2. The interaction forces shown in Fig. 2.4 is seen to be qualitatively similar to the micro-scale forces shown in Fig. 2.2.

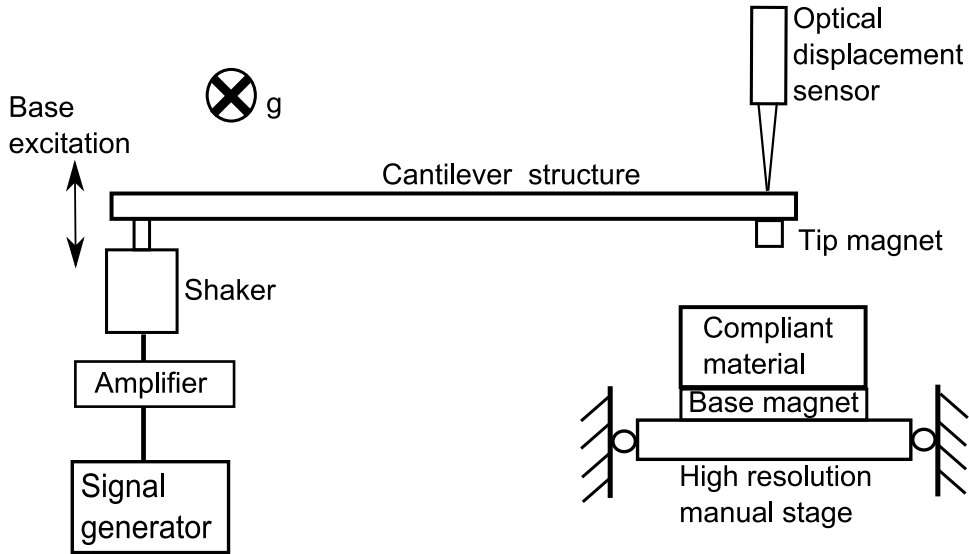


Figure 2.5: Schematic of experimental arrangement at macro-scale.

2.2.2 Experimental arrangement and results

The experimental arrangement consists of an aluminum beam with a magnet attached to its tip, as shown in Fig. 2.3(a) and Fig. 2.5. The length of the beam is 0.295 m and the area of the cross-section is $0.95 \times 20 \text{ mm}^2$. The Young's modulus of the beam material is 70 GPa and the material density is 2700 Kg/m^3 . The mass of the magnet attached to the beam tip is 0.0943 grams. The beam motion is excited in the horizontal direction, and hence, it can be assumed that there is no effect of gravity in the experiments. The first and second natural frequencies of the beam are experimentally determined as 7.14 Hz and 46.8 Hz, respectively. The primary interest in this study lies in the system behavior when the excitation frequency is in between these two frequencies. The schematic of the experimental set up is shown in Fig. 2.5. The input excitation is imparted on the beam by a Brüel and

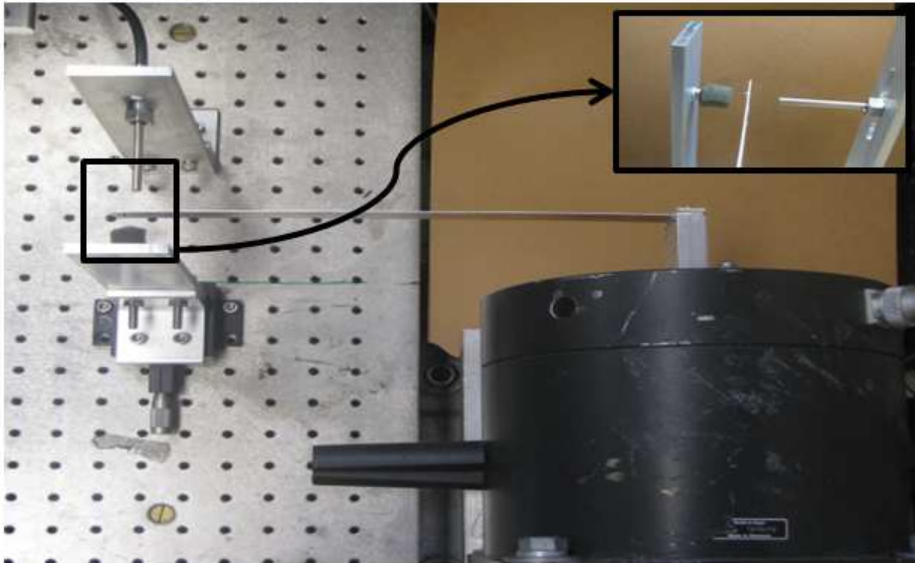


Figure 2.6: Details at the tip in the context of the experimental arrangement.

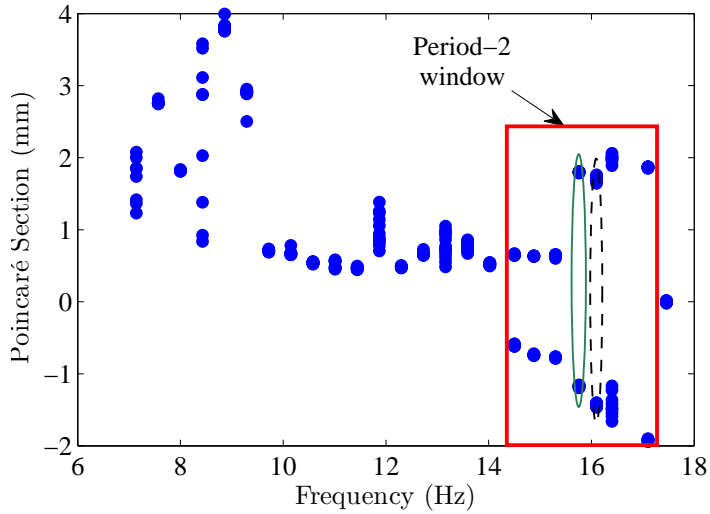


Figure 2.7: Experimentally obtained diagram of qualitative changes on Poincaré section for excitation frequencies higher than the system’s first natural frequency. Here, the scalar control parameter is the excitation frequency. The Poincaré sections are constructed by using the excitation frequency as the clock frequency.

Kjær vibration exciter, which is referred as the shaker. The displacement of the tip is recorded with a PHILTEC optical displacement sensor. The initial distance between the magnetic tip and the compliant surface can be varied by using the high resolution manual stage, on which the base magnet and the compliant material is stationed. A snapshot of the experimental set up is shown in Fig. 2.6.

In order to observe the responses of the system for various excitation frequencies, the author started the experiments from the first natural frequency of the system located at 7.14 Hz, and gradually carried out a quasi-static sweep of the excitation frequency while ensuring that the beam-tip made near-grazing impact with the compliant material. In keeping with the previous work conducted in the

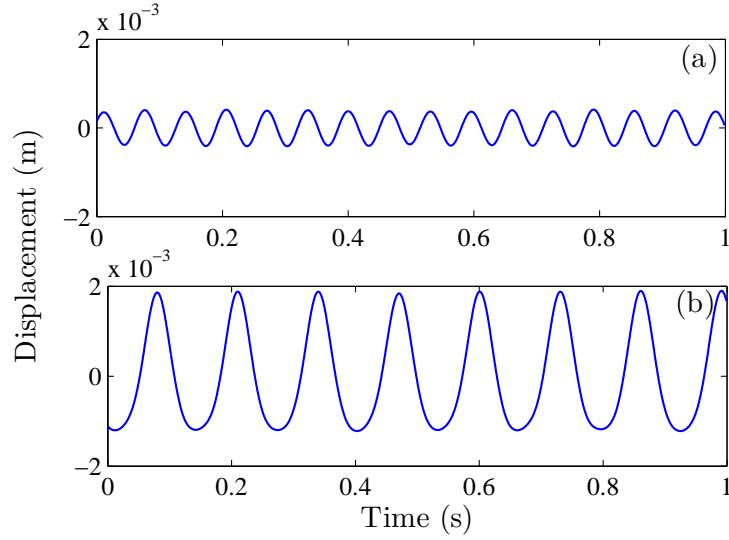


Figure 2.8: Experimentally obtained cantilever tip displacement history for excitation at 15.4 Hz: (a) unconstrained motions (motions without contact) and (b) constrained motions.

group by Dick *et al.* (2009), no qualitative changes were seen when the excitation frequency was close to the first resonance frequency. The first period-doubling was observed when the excitation frequency was around 14.5 Hz, which is 2.03 times the first natural frequency of the system. This *period-doubling window* was observed up to the forcing frequency value of 17.1 Hz, which is 2.39 times the first natural frequency of the system. The experimentally obtained diagram of qualitative changes on a Poincaré section is presented in Fig. 2.7. As in earlier work (Dick *et al.*, 2009), these experiments have been carried out at “near-grazing” conditions. For the frequency value of 15.4 Hz, marked out by the solid ellipse in Fig. 2.7, the corresponding beam-tip displacements and response spectrum are shown for unconstrained (i.e., without contact) and constrained motions in Fig. 2.8 and Fig.

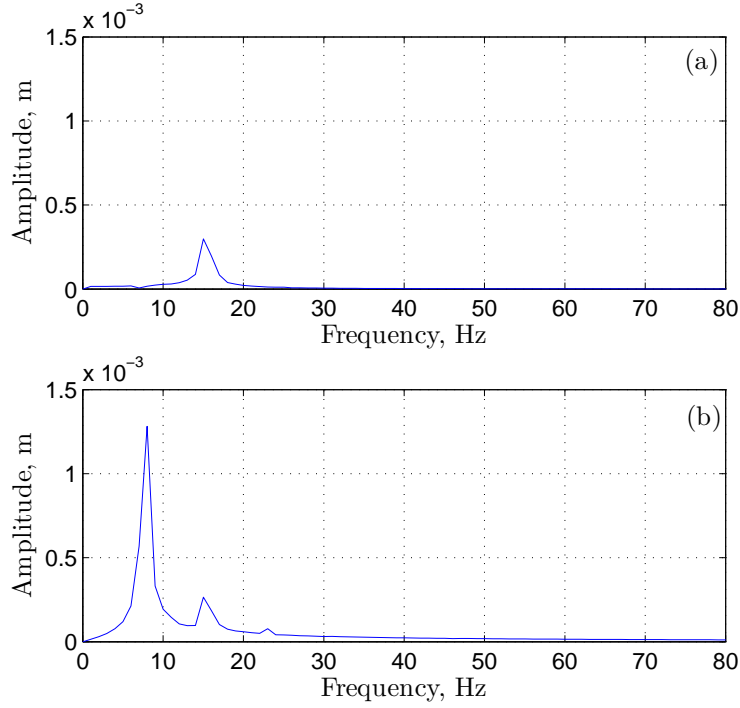


Figure 2.9: Experimentally obtained response spectra for excitation at 15.4 Hz: (a) unconstrained motions (motions without contact) and (b) constrained motions.

2.9, respectively. In the unconstrained case, the basic frequency component of the system response is the same as the excitation frequency, while in the constrained case, the basic frequency component is one half of the excitation frequency, which is indicative of a period-doubled response. As the distance between the tip and the sample is further decreased, a transition to aperiodic motions is seen, as shown in Fig. 2.10. The phase portrait for this aperiodic motion is shown in Fig. 2.11. The time-series data for this aperiodic motion have been analyzed to find the correlation dimension (e.g., Nayfeh and Balachandran, 1995). A fractional dimension of 2.624 was obtained for these data, suggesting that the observed aperiodic motion has a

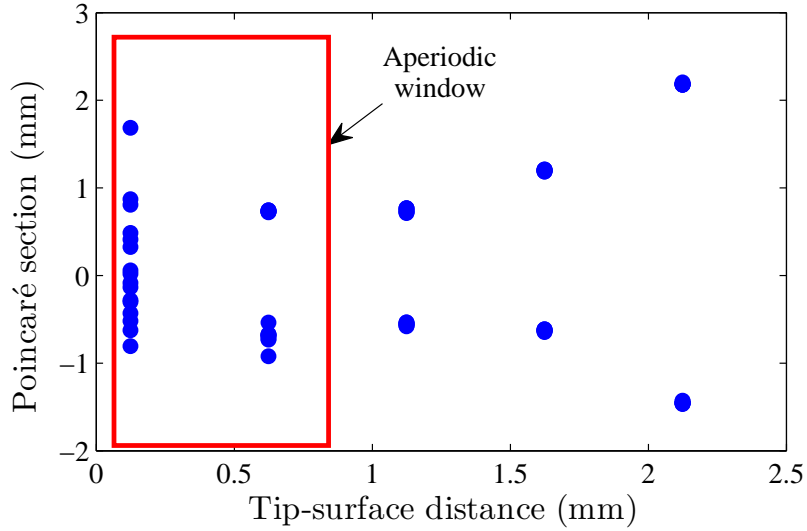


Figure 2.10: Experimentally obtained diagram of qualitative changes on Poincaré section when excitation frequency is 2.24 times the system's first natural frequency. Here, the scalar control parameter is the distance between the tip and sample. A transition to aperiodic motion from the period-doubled response at near-grazing condition is observed as the separation between the cantilever tip and the compliant material is decreased.

fractal character. The plot of $\ln C_r$ versus $\ln(r)$ is given in Fig. 2.12, and the reported dimension value is based on the scaling region determined for the embedding dimension $d = 8$.

2.3 Computational modeling and numerical results

The response of the impacting cantilever beam is studied by using a reduced-order model developed through a Galerkin projection of the governing equations of

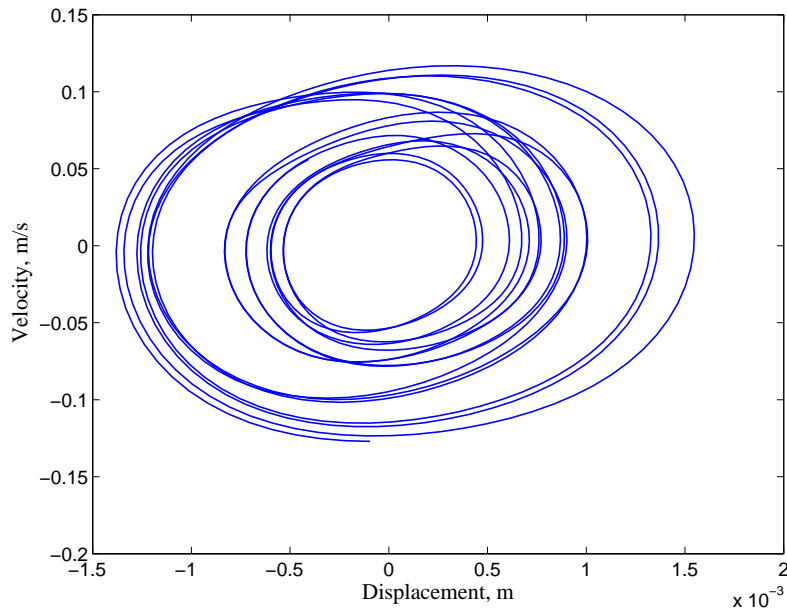


Figure 2.11: Experimentally obtained phase portrait for aperiodic response.

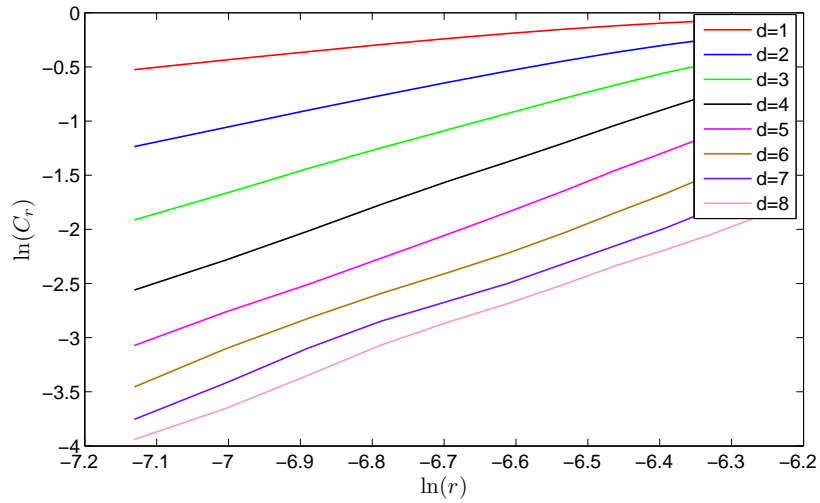


Figure 2.12: Plot of $\ln C_r$ versus $\ln r$ for aperiodic data for different embedding dimensions.

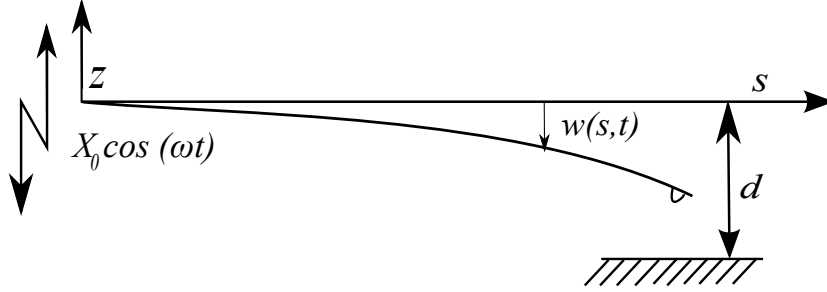


Figure 2.13: Model of a base excited cantilever beam subjected to impacts at the free end.

motion. In developing this model, the geometric nonlinearity is not considered, and only the nonlinearity associated with loss of contact is considered, as this nonlinearity is expected to be dominant in determining the motion characteristics. Furthermore, this is reasonable, as the magnitude of tip displacement is small. The equations are nondimensionalized, so that multi-scale simulations can be carried out.

2.3.1 Model development

The model development follows that used in the earlier work of Balachandran (2003) and Long *et al.* (2008). In constructing the Lagrangian of the continuous system, the inextensionality condition is taken into account. This condition provides a relationship between the longitudinal and transverse displacement fields of the cantilever. Here, the transverse displacement field is denoted by $w(s,t)$, where t is the time and s is the spatial coordinate along the length of the cantilever. The extended Hamilton's principle is used to determine the governing differential system

and boundary conditions. Retaining up to cubic terms, the governing equation of motion in the open domain reads as

$$\begin{aligned} & \rho A \ddot{w} + EI w^{iv} + EI (w' (w' w'')')' - \frac{1}{2} m w'' \int_0^L \frac{\partial^2}{\partial t^2} (w'^2) ds + \\ & \frac{1}{2} \rho A w' \frac{\partial}{\partial s} \left[\int_L^s \int_0^s \frac{\partial^2}{\partial t^2} (w'^2) d\hat{s} ds \right] + \\ & \frac{1}{2} \rho A w'' \left[\int_L^s \int_0^s \frac{\partial^2}{\partial t^2} (w'^2) d\hat{s} ds \right] = F_b \end{aligned} \quad (2.3)$$

where ρ is the density of the beam material, EI is the flexural rigidity, m is the tip mass and A is the cross section of the beam. The term F_b is the base excitation. It is written as,

$$F_b = \rho \omega^2 A X_0 \cos(\omega t)$$

where ω is the frequency of excitation and X_0 is the magnitude of the base excitation. In Eq. (2.3), the prime superscript denotes a derivative with respect to the spatial coordinate s and the overdot represents a derivative with respect to time t .

2.3.2 Nondimensionalization and discretization

The following nondimensional quantities are introduced:

$$\begin{aligned} \bar{w} &= \frac{w}{L}, & \bar{s} &= \frac{s}{L}, & \tau &= \omega_n t, \\ \nu &= \frac{X_0}{L}, & \eta &= \frac{d}{L}, & \xi &= \frac{A_0}{L}, \\ \gamma &= \frac{m}{\rho A L}, & \kappa &= \frac{K_E}{\rho A \sqrt{L} \omega_n^2}, & \lambda &= \frac{K_M}{\rho A L^4 \omega_n^2}, \\ & & \Omega &= \frac{\omega}{\omega_n}. \end{aligned}$$

As earlier mentioned, in the model development, the author considers only the nonlinearities generated by the tip-sample interaction forces, and the geometric nonlinearities in the left-hand side of Eq. (2.3) are ignored. The contact force along with the magnetic attraction is taken into account in the boundary conditions. The boundary conditions without the nonlinear terms are given by

$$\begin{aligned}
\bar{w}(\bar{s}, \tau) &= 0 & \text{at } \bar{s} = 0 \\
\bar{w}'(\bar{s}, \tau) &= 0 & \text{at } \bar{s} = 0 \\
\bar{w}''(\bar{s}, \tau) &= 0 & \text{at } \bar{s} = 1 \\
\bar{w}'''(\bar{s}, \tau) &= \gamma\ddot{\bar{w}} + f_{ts} & \text{at } \bar{s} = 1.
\end{aligned} \tag{2.4}$$

Here, the prime superscript denotes the derivative with respect to the nondimensional space parameter \bar{s} and f_{ts} , the nondimensional tip-sample force, is given by

$$f_{ts}(\bar{z}) = \begin{cases} -\frac{\lambda}{(\bar{z} + \eta + \xi)^2} & \text{for } \eta + \bar{z} > 0 \\ -\frac{\lambda}{(\xi)^2} + \kappa(-\eta - \bar{z})^{1.5} & \text{for } \eta + \bar{z} \leq 0 \end{cases} \tag{2.5}$$

Here, \bar{z} is the nondimensional absolute displacement of the cantilever tip given by

$$\bar{z} = \bar{w} + \nu \cos(\Omega\tau).$$

Next, the displacement field is expanded as

$$\bar{w}(\bar{s}, \tau) = \sum_{r=1}^{\infty} q_r(\tau) \phi_r(\bar{s}) \tag{2.6}$$

where $q_r(\tau)$ is the time-dependent part and $\phi_r(\bar{s})$ is the associated spatial function. This spatial function is assumed to be given by the mode shape of a cantilever beam, which has the form

$$\phi_r(\bar{s}) = C_{1r} [\sin(\beta_r \bar{s}) - \sinh(\beta_r \bar{s})] + C_{2r} [\cos(\beta_r \bar{s}) - \cosh(\beta_r \bar{s})]. \tag{2.7}$$

In Eq. (2.7), C_{1r} , C_{2r} , and β_r are determined from the characteristic equation. Since the first and the second natural frequencies of the beam are well separated, the author has used a single-mode approximation. Particularly, the phenomenon of period-doubling events close to grazing impacts is seen to be captured well by a single-mode approximation. For a single-mode approximation, the response of the system is given by

$$\bar{w}(\bar{s}, \tau) = q_1(\tau)\phi_1(\bar{s}).$$

Writing Eq. (2.3) in terms of the nondimensional parameters and then discretizing the model by using the above form of \bar{w} , carrying out a Galerkin projection, and including linear damping, the following reduced-order model is obtained:

$$m_1\ddot{q}_1 + k_1q_1 + c_1\dot{q}_1 + \text{nonlinear terms} = f_b + f_c \quad (2.8)$$

where the nonlinear terms are as obtained in earlier studies (see Long *et al.*, 2008; Balachandran, 2003) and the other terms are given by

$$m_1 = \int_0^1 \phi_1(\bar{s})\phi_1(\bar{s})d\bar{s} + \gamma \{\phi_1(\bar{s} = 1)\}^2$$

$$k_1 = \int_0^1 \phi_1(\bar{s})\phi_1(\bar{s})d\bar{s}$$

$$c_1 = 2m_1\zeta$$

$$f_b = \left(\int_0^1 \phi_1 d\bar{s} \right) \Omega^2 \nu \cos(\Omega\tau)$$

$$f_c = (\phi_1(\bar{s} = 1)) f_{ts}$$

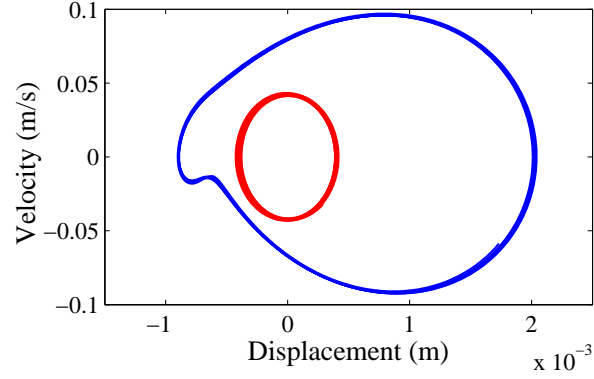


Figure 2.14: Numerically obtained phase portraits for the excitation frequency of 15.4 Hz. Unconstrained motions correspond to the smaller orbit and constrained motions correspond to the larger orbit.

Table 2.2: Simulation parameter values.

Property	Value
Beam length (L)	295 mm
Material density (ρ)	2700 Kg/m ³
Cantilever Young's Modulus (E)	70 GPa
Thickness of foam (A_0)	5 mm
Quality factor (Q)	10
Constant related to magnetic force (K_M)	4.3×10^{-10}
Constant related to elastic force (K_E)	2.3×10^3
Excitation amplitude (X_0)	0.44 mm

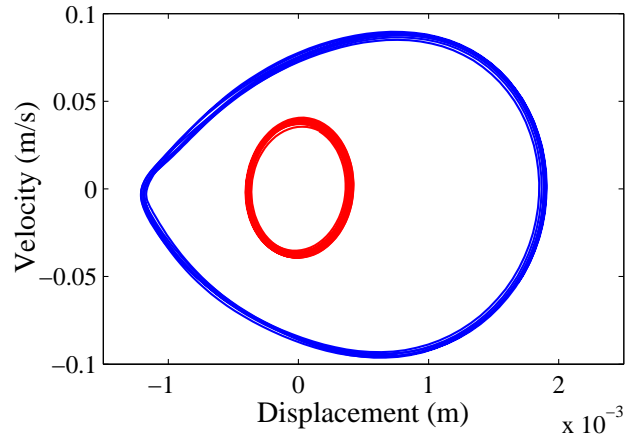


Figure 2.15: Experimentally obtained phase portraits for the excitation frequency of 15.4 Hz. Unconstrained motions correspond to the smaller orbit and constrained motions correspond to the larger orbit.

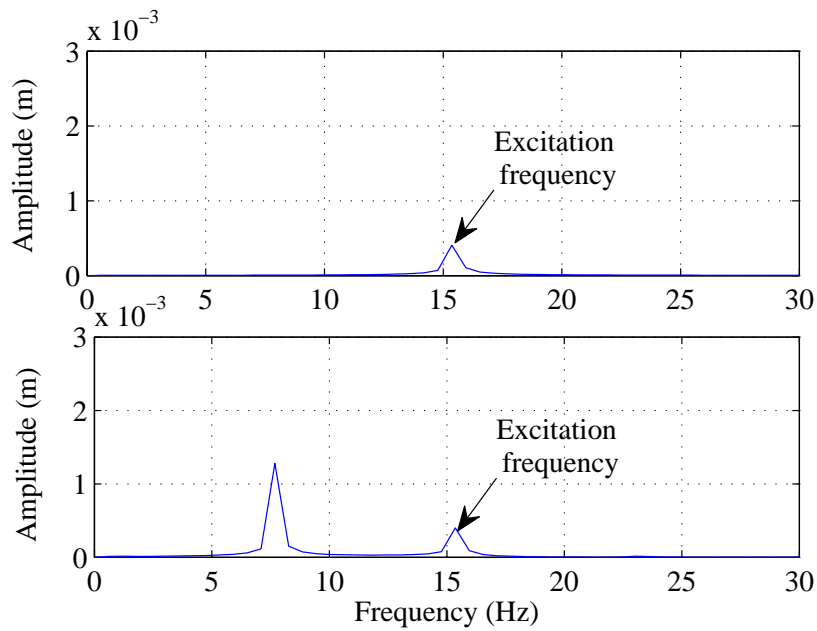


Figure 2.16: Response spectra for unconstrained motions (top) and constrained motions (bottom) at 15.4 Hz.

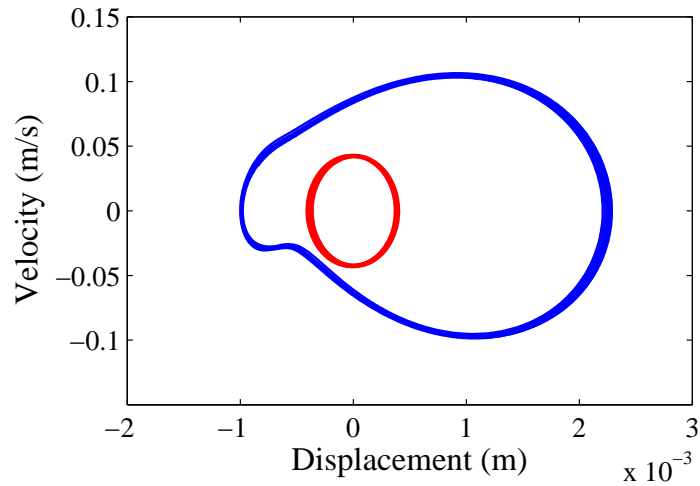


Figure 2.17: Numerically obtained phase portraits for excitation frequency of 16.1 Hz. Unconstrained motions correspond to the smaller orbit and constrained motions correspond to the larger orbit.

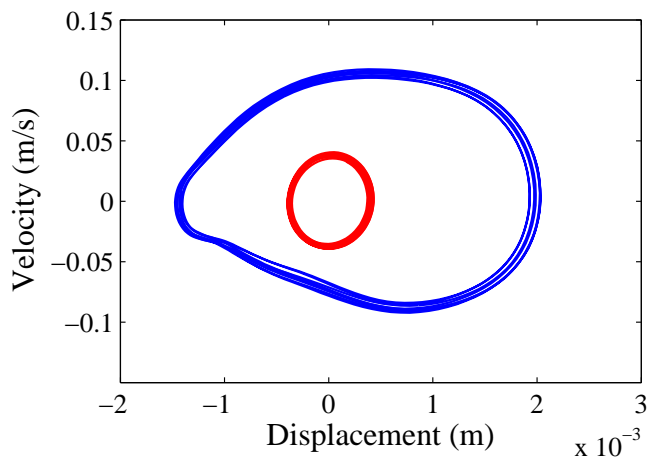


Figure 2.18: Experimentally obtained phase portrait for excitation frequency of 16.1 Hz. Unconstrained motions correspond to the smaller orbit and constrained motions correspond to the larger orbit.

2.3.3 Numerical results

In order to observe the response of the cantilever through numerical simulations, parameters are identified from the experimental response. The linear damping is identified by an experimental method. The cantilever tip is given an initial displacement and the response of the tip is recorded. These data are taken for a case where no contact or tip interaction forces were present in the experiment. This experimentally obtained response was matched with numerically obtained response for a linear damping. The damping ratio for which the numerically obtained response is closest to the experimentally obtained response, is selected as the damping ratio for the numerical simulations. The constants related to the attractive and repulsive forces are found out by matching the experimentally obtained response with the simulations from the numerical model when the cantilever is experiencing both attractive and repulsive interaction forces, i.e., making periodic contact with the compliant material.

Direct numerical simulations of Eq. (2.8) are carried out to compare the numerical results with the experimental observations. The parameters used to carry out the simulations are given in Table 2.2. Two frequencies, marked by the solid line ellipse and dotted line ellipse in Fig. 2.7, are chosen for making response comparisons amongst experimental and numerical results. These frequencies are 15.4 Hz and 16.1 Hz, for both of which period-two responses were observed in experiments under conditions of near-grazing contact. The numerically obtained phase portraits for both constrained and unconstrained motions are compared with the correspond-

ing experimental results in Fig. 2.14 and Fig. 2.15, for an excitation frequency of 15.4 Hz. The corresponding numerically determined response spectra are shown in Fig. 2.16. The same period-doubling phenomenon is observed in the reduced-order model predictions. The experimental and numerical results obtained for an excitation frequency of 16.1 Hz are compared in Fig. 2.17 and Fig. 2.18. Again, good agreement is seen between the experimental and numerical results. These results are illustrative of the period-doubling phenomenon close to grazing for excitation frequencies between the first and the second natural frequencies. The author has also carried out multi-mode studies. These studies are not reported here, since the experimentally observed phenomena are well captured in the numerical study with a single-mode approximation. Although the participation of the second mode is less than 10% in terms of magnitude of the first mode, the phase portraits are expected to have certain quantitative differences when multiple modes are considered. The quantitative differences are in the form of shape variations in the phase portraits. However, it is noted that the numerical results obtained with the single-mode approximation are in good agreement with the experimentally obtained results, and the reduced-order model reported here helps shed light on the associated qualitative changes experienced by the system. The computational model with multiple modes is presented in Appendix A of this dissertation.

2.4 Summary

In this chapter, the macro-scale experimental system has been presented and experiments conducted with it have been described along with the associated modeling and numerical efforts. Period-doubling bifurcations are studied in detail through experimental and numerical means. It is observed that for a certain range of frequencies of excitations (in between the first and the second natural frequencies), near-grazing contact can be identified due to the occurrence of period-doubling bifurcations. This idea of identifying grazing or near-grazing contact through a bifurcation behavior is pursued in the context of an AFM operated in tapping mode, as described in Chapter 3.

Chapter 3

AFM Experimental and Numerical Studies

In this chapter, the experimental arrangement, results and numerical studies associated with the micro-scale AFM system are presented and discussed. The motivation behind conducting the macro-scale studies were to apply the findings to the micro-scale AFM system. Since, period-doubling bifurcations were observed for a range of excitation frequencies in the macro-scale system, off-resonance operations are studied in an AFM system, operated in dynamic mode (also known as AM-AFM or tapping mode AFM). Period-doubling bifurcations can be used to identify grazing contact in AM-AFM for off-resonance excitation frequencies. Operating the AFM at a grazing point can result in reduced repulsive forces between the tip and the sample, which is desirable for imaging soft samples.

The principle of dynamic mode AFM is described in the next section. This is followed by a discussion of the experimental AFM arrangement. The computational model is similar to the computational model used for macro-scale system which was presented in Chapter 2. The numerical results are compared with experimentally obtained results.

3.1 Dynamic mode operation of AFM

The amplitude modulation mode (AM-AFM) is also known as the tapping mode AFM or AC AFM. In this mode of operation, a harmonic excitation is provided through a piezoelectric actuator, to the AFM cantilever base. A set-point amplitude is defined and the base-excited cantilever is lowered until the response of the tip reaches the set-point value. The response of the cantilever is detected by a laser and photo-detector combination. The height of the cantilever and sample or the base-excitation amplitude is varied to maintain a constant set-point amplitude of the cantilever tip. Since the tip makes intermittent contact with the sample, this mode of operation sheds light on both short-range and long-range force interactions between the tip and the sample. This mode of operation is increasingly popular for the characterization of soft materials such as biological samples. Since, biological samples can be destroyed by forces of the order of a few nanoNewtons, it is important to reduce the maximum repulsive force. In tapping mode operation, the frequency of excitation is generally the first resonance frequency of the cantilever. The cantilever resonance frequencies can be determined experimentally by thermal tuning of the cantilever. Typically the cantilever is excited at the resonance frequency. However, in the present work, the frequency of excitation is chosen to be between the first and the second natural frequencies of the system. A primary focus of this study is to locate near-grazing contact through period-doubling bifurcations. If the excitation frequency of the cantilever is away from the resonance frequency, near-grazing contact can be identified based on the observed period-two responses

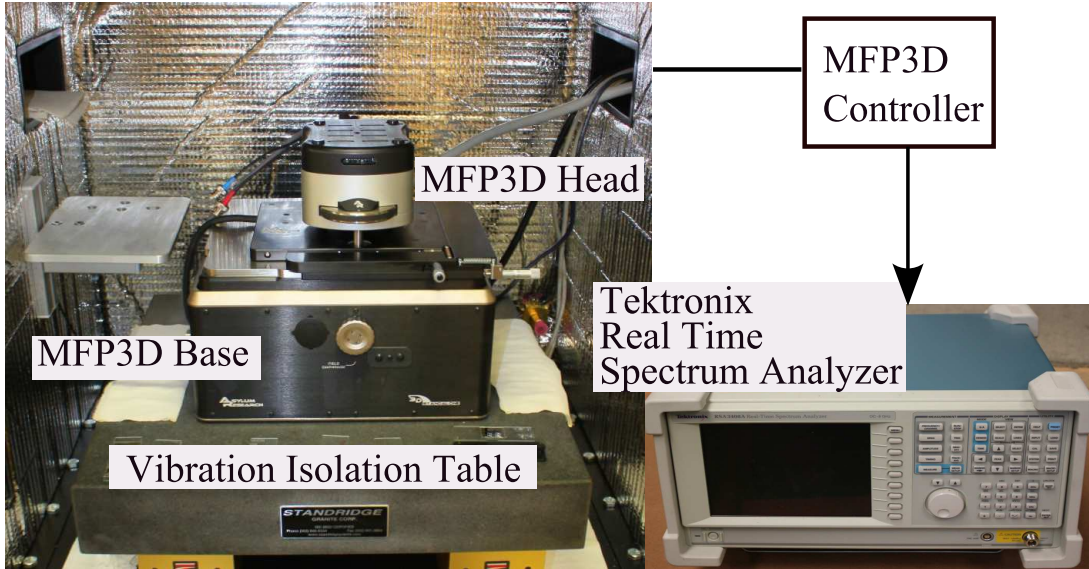


Figure 3.1: Snapshot of the experimental arrangement located in the AFM lab at the Department of Mechanical Engineering at the University of Maryland. An Asylum Research MFP3D AFM is connected to a Tektronix signal analyzer to locate the period-two response for near-grazing impacts.

of the cantilever.

3.2 Experimental arrangement and observations

The micro-scale experimental arrangement is shown in Fig. 3.1. From the results obtained in the studies of macro-scale experiments, it is expected that there exists a period-two window for off-resonance excitation frequencies. However, in order to locate that period-two window in an AFM operation, it is necessary to analyze the tip response in real time. In order to achieve this, the displacement signal of the oscillating tip is fed into a Tektronix RSA 3408A 8 GHz Real-Time

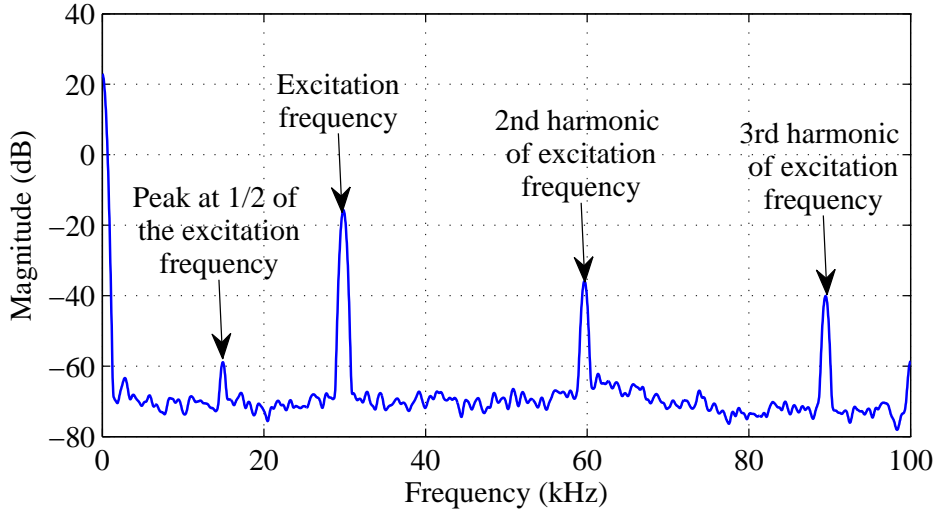


Figure 3.2: Power spectrum of the response of the cantilever tip when the tip makes near-grazing contact with the sample. The peak located at half the excitation frequency is indicative of the period-two response of the cantilever.

Spectrum Analyzer. All experiments were conducted with an Asylum Research MFP3D AFM. The excitation frequency was varied manually in very small steps (.001 kHz), since the window of period-two response was seen to be much smaller compared to that of the macro-scale case.

The cantilever-sample combination used was Si cantilever with a Si(100) sample. The cantilever used for the experiments is a NanoWorld CONT cantilever. The length, width, and the thickness of the cantilever are 450.00 μm , 50.00 μm , and 2.00 μm , respectively. Due to a low force constant (stiffness) of this cantilever, it is particularly useful in carrying out an operation where the frequency of excitation is away from the resonance frequencies of the cantilever. The first natural frequency of the cantilever is found to be at 12.72 kHz. The second natural frequency of the can-

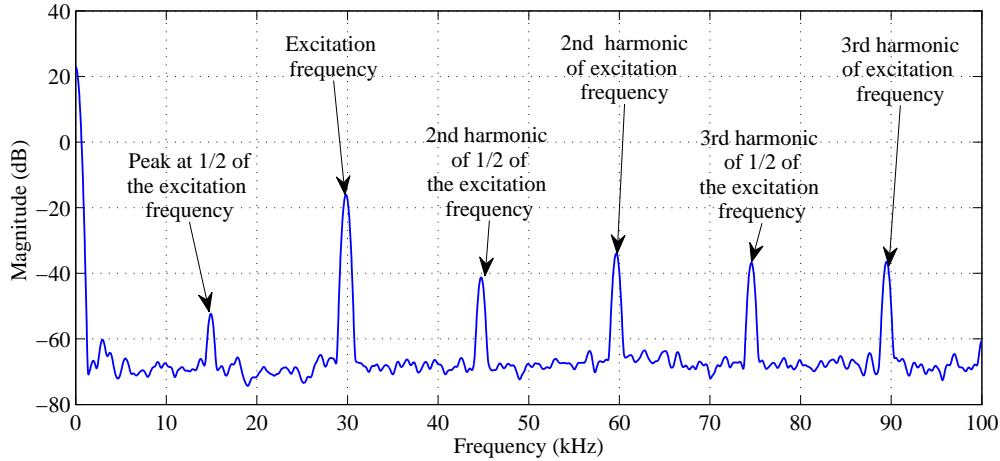


Figure 3.3: Power spectrum of the response of the cantilever tip when the excitation amplitude is higher, for the same excitation frequency as used in Fig. 3.2. Higher harmonics are seen for harder impacts.

tilever is 78.64 kHz. The cantilevered structure’s response signals are monitored by using the real time signal analyzer to identify qualitative changes associated with grazing contact, when the frequency of excitation is in between the first and the second natural frequencies of the system.

The AFM is operated at tapping mode, with the frequency of excitation in between the first and the second natural frequencies. Period-doubling responses were found when the frequency of excitation is around 2.34 times the first natural frequency of this particular cantilever-sample combination. In Fig. 3.2, the power-spectrum data obtained from the spectrum analyzer is presented. A peak at half of the excitation frequency is observed, which confirms the existence of a period-2 response at this operating point. Keeping all other operating parameters constant, the drive amplitude is increased to observe the dynamics with harder impacts. In Fig.

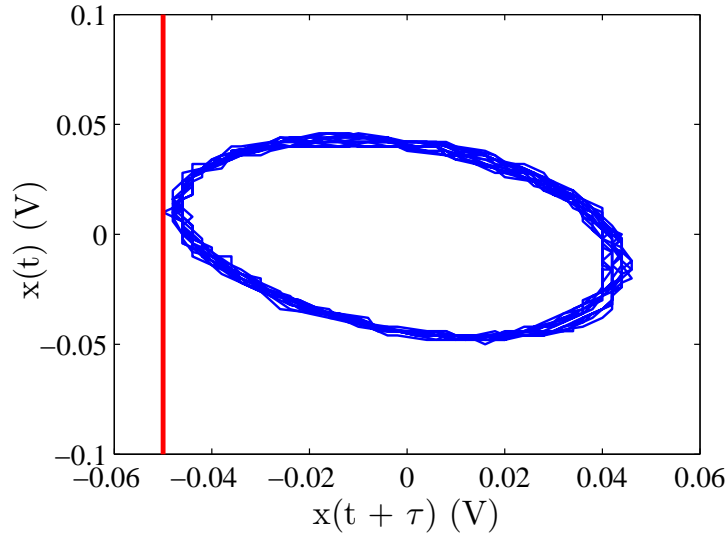


Figure 3.4: Experimentally obtained phase portrait for Si cantilever and Si(100) sample combination, before the tip makes grazing impacts with the sample. The vertical line signifies the location of the sample.

3.3, the power spectrum of the response signal is presented for a higher drive amplitude. It is observed that higher harmonics are prominent in the post-bifurcation region. Similar phenomenon was observed in the macro-scale case for post-grazing conditions. In Fig. 3.4, the phase portrait of the displacement data is presented, for the cantilever tip response, just before the tip makes grazing contact with the sample. The vertical line represents the location of the sample, which is obtained from the set point amplitude, in this case. The phase portrait for the case of grazing periodic orbits is presented in Fig. 3.5.

The phase portrait shown in Fig. 3.5 is illustrative of the period-doubling phenomenon associated with near-grazing contact, when the excitation frequency is 2.34 times the first natural frequency; this phenomenon is similar to what was

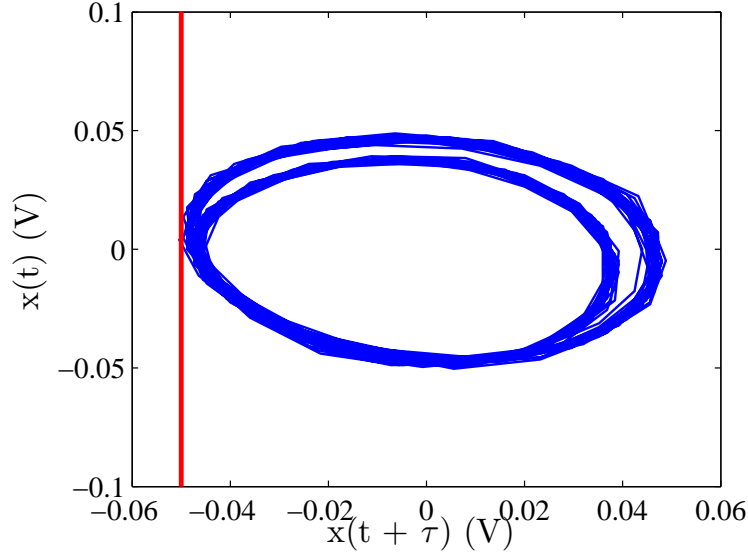


Figure 3.5: Experimentally obtained period-two phase portrait for Si cantilever and Si(100) sample combination, after the tip makes grazing impacts with the sample. The vertical line signifies the location of the sample

observed in the macro-scale system wherein the frequency location is different.

3.3 Numerical studies

The numerical model used for simulations of the micro-scale cantilever dynamics is similar to that reported in Chapter 2. However, the tip-sample forces are modeled as a combination of van der Waals attractive force and DMT contact force and the tip mass of the cantilever is neglected in the micro-scale case. The reduced-order model is recalled first:

$$m_1 \ddot{q}_1 + k_1 q_1 + c_1 \dot{q}_1 = f_b + f_c. \quad (3.1)$$

The different terms in the above equation are the same as that used in Eq. (2.8) of Chapter 2. The nondimensional form of the tip-sample forces are expressed as

$$f_{ts}(\bar{z}) = \begin{cases} -\frac{\lambda}{(\bar{z}+\eta)^2} & \text{for } \eta + \bar{z} > \eta_0 \\ -\frac{\lambda}{\eta_0^2} + \kappa(\eta_0 - \bar{z} - \eta)^{1.5} & \text{for } \eta + \bar{z} \leq \eta_0 \end{cases} \quad (3.2)$$

Here, \bar{z} is the absolute displacement of the cantilever.

The parameters listed in Eq. (3.2) stand for the same quantities as in Section 2.3 in Chapter 2. The parameters which differ from the macro-scale model are:

$$\lambda = \frac{HR}{6a_0^2\rho AL^4\omega_n^2}$$

$$\kappa = \frac{4E^*\sqrt{R}}{3\rho A\sqrt{L}\omega_n^2}$$

$$\eta_0 = \frac{a_0}{L}.$$

Table 3.1: Simulation parameter values.

Property	Value
Cantilever length (L)	450 μm
Cantilever width (b)	50 μm
Cantilever thickness (h)	2 μm
Material density (ρ)	2300 Kg/m ³
Cantilever Young's Modulus (E)	176 GPa
Tip radius (R)	20 nm
Effective Young's Modulus (E^*)	94.91 GPa
Hamaker Constant (H)	$2.96 \times 10^{-19} J$
Intermolecular distance (a_0)	0.2 nm

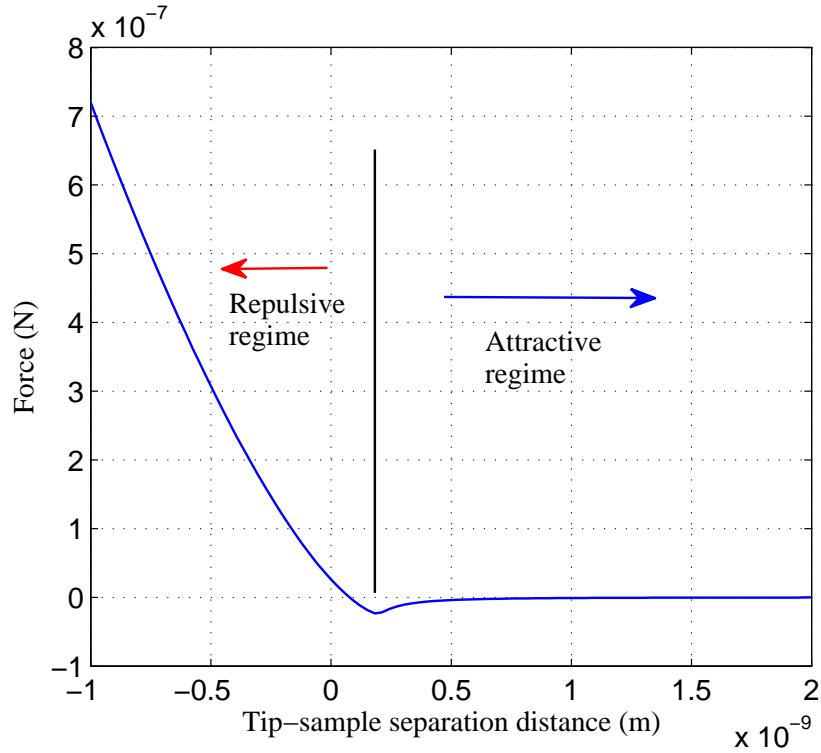


Figure 3.6: Tip-sample force curve for a Si cantilever and a Si(100) sample.

The simulation parameters are listed in Table 3.1. The force profile for this cantilever-sample combination (Si-Si) is shown in Fig. 3.6. The force profile has been obtained by using Eq. (3.2).

Numerical simulations are carried out for before and after grazing contact conditions. For non-contact conditions (when the tip does not make contact with the sample), the phase portrait, response spectrum, and the force on the tip are as presented in Figures 3.7, 3.8, and 3.9, respectively. The numerically obtained first natural frequency is around 13 kHz, which is close to the experimentally observed natural frequency. The frequency of excitation is 2.34 times the first natural frequency (same as in the experiments described). From Fig. 3.7 and Fig. 3.8, it is

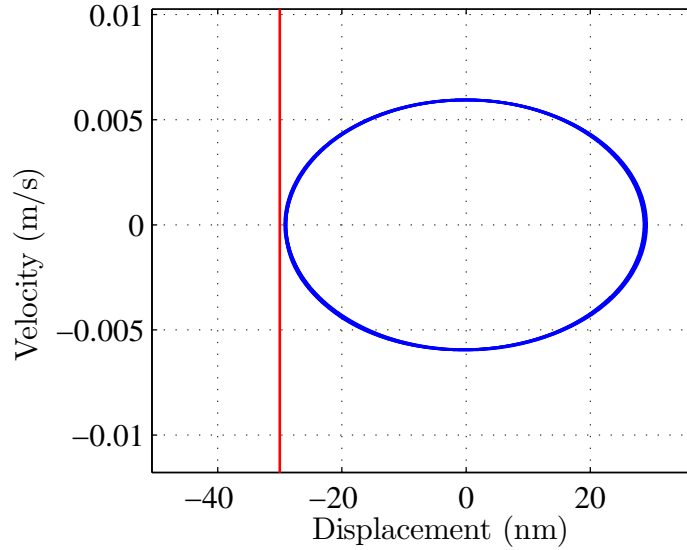


Figure 3.7: Phase portrait of the AFM cantilever tip when the tip does not make intermittent contact with the sample. The solid vertical line represents the location of the sample.

evident that no period-doubling is observed when there is no contact between the tip and the sample. The force experienced by the tip is seen to be always attractive. Since there is no contact between the tip and the sample, the repulsive force does not come into play.

When the tip makes near-grazing contact with the sample, the phase portrait, response spectrum, and the force on the tip are as shown in Figures 3.10, 3.11, and 3.12, respectively. In this case, the response of the cantilever tip is seen to have a dominant component at one half of its excitation frequency. In Fig. 3.11, the peak at one half of the frequency of excitation confirms that the frequency of response is at half of the frequency of excitation. The force experienced by the cantilever tip is

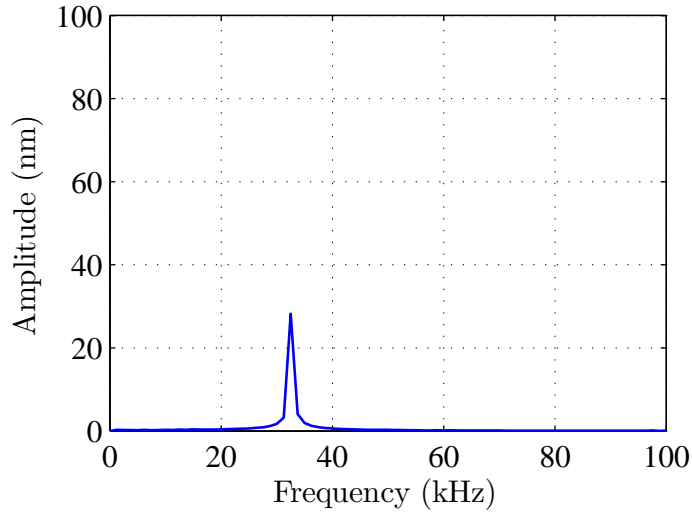


Figure 3.8: Response spectrum of the cantilever tip response when the tip is not making contact with the sample. A single peak is seen at the frequency of excitation.

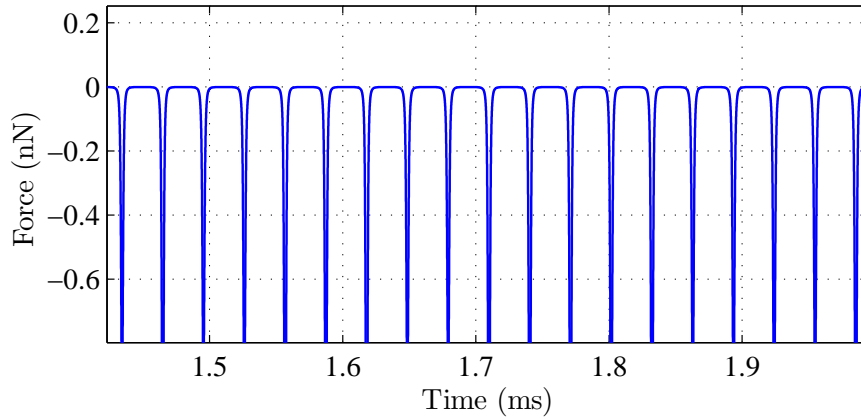


Figure 3.9: Force on the cantilever tip when the tip is not making contact with the sample. The forces are always attractive due to long-range forces.

shown in Fig. 3.12. So, it can be concluded that if the AFM cantilever is operated in off-resonance excitation frequencies, near-grazing contact can be identified through the occurrence of a period-doubling bifurcation. Operating the cantilever at this

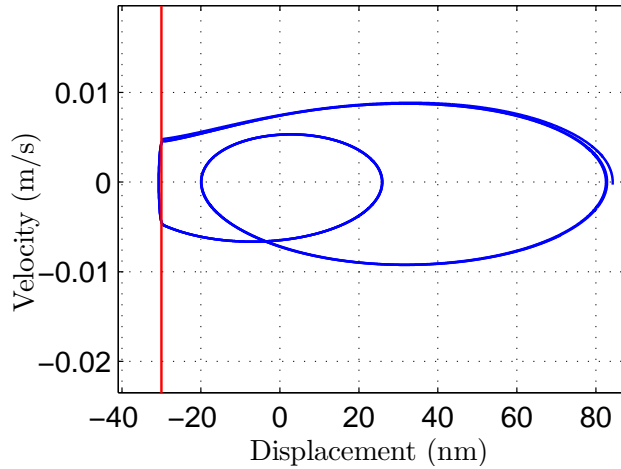


Figure 3.10: Phase portrait of the AFM cantilever tip when the tip makes intermittent contact with the sample. The solid vertical line represents the location of the sample.

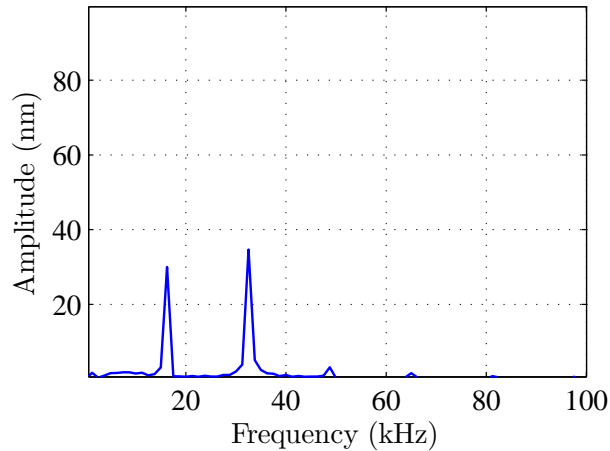


Figure 3.11: Response spectrum of the cantilever tip response when the tip makes contact with the sample. A peak is seen at half the frequency of excitation.

point will ensure low-velocity impacts and this in turn will result in a reduction of repulsive contact forces.

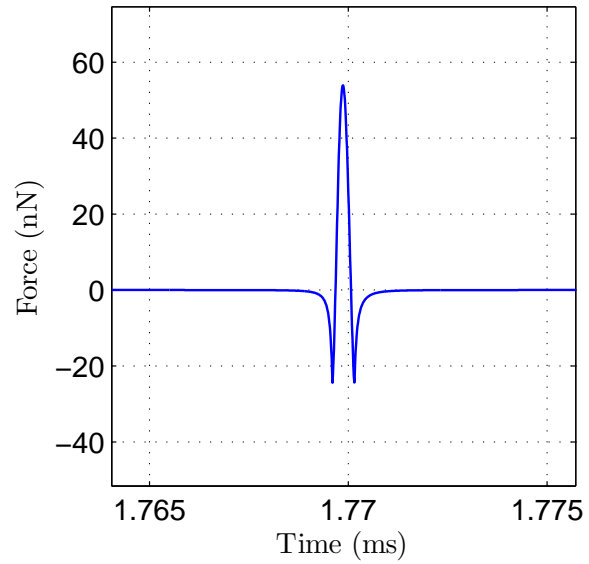


Figure 3.12: Force on the cantilever tip when the tip is making contact with the sample. Both attractive and repulsive interaction forces come into play.

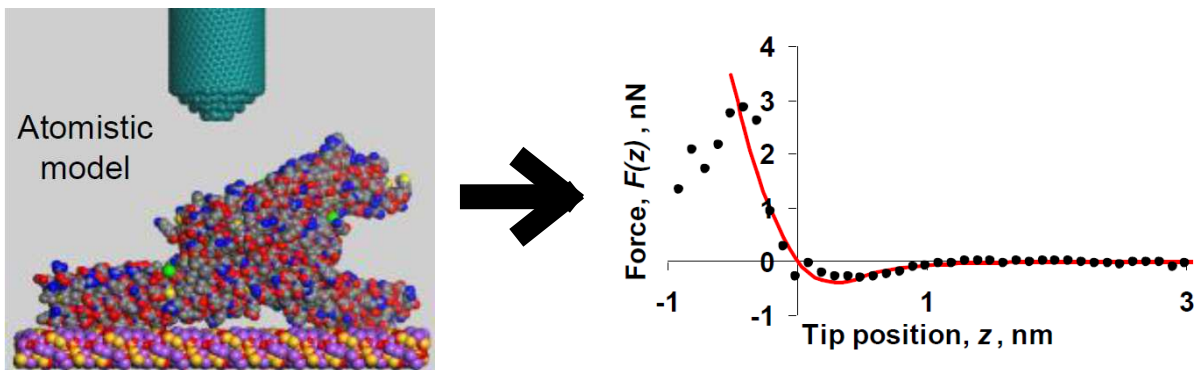


Figure 3.13: Force curve obtained from molecular dynamic simulations (Solares, 2007).

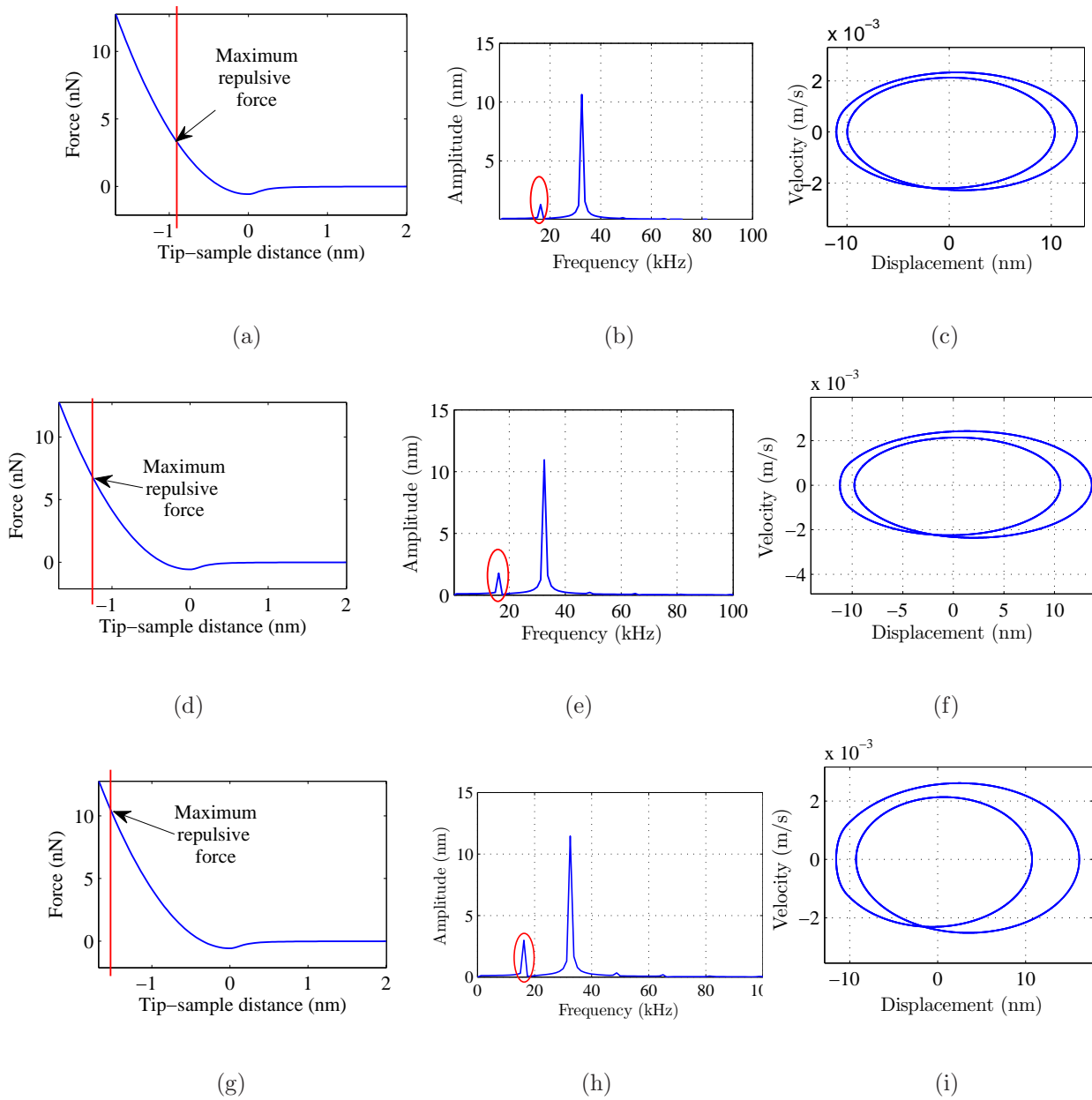


Figure 3.14: Tip-sample force profiles and the location of the maximum repulsive force for contact is presented in (a), (d), and (g). Response spectra are presented in (b), (e), and (h). The corresponding phase portraits are presented in (c), (f), and (i).

3.4 Operations with soft samples

High repulsive forces are undesirable while scanning soft materials such as biological samples, tissues, and cells. The proposed method of operating the cantilever in near-grazing condition can help minimize the repulsive forces and also serve as a means to identify contact (through period-doubling bifurcation). In this section, numerical simulation results are presented for a soft bacteriorhodopsin sample. The tip-sample force curve is obtained from a curve fit to data obtained from molecular dynamic simulations (Solares, 2007). The constructed force curve is expressed as

$$F(z) = \begin{cases} -\frac{W}{1+30z^2} & \text{for } z > 0 \\ -W + sz^2 & \text{for } z \leq 0 \end{cases}. \quad (3.3)$$

In Eq. (3.3), z is the distance between the tip and the sample, the values of the constants W and s are 0.5736 and 4.7374, respectively. Numerical simulations are carried out with previously described models and the results are presented in Fig. 3.14. Here, the frequency of excitation is 2.34 times the first natural frequency of the system. Each row in Fig. 3.14 corresponds to the same operating conditions. The excitation amplitude is gradually increased to induce higher penetration by the tip into the sample. It is observed that the peak at one half of the excitation frequency gets stronger as the maximum repulsive force becomes larger for harder impacts. This phenomenon has been previously observed in the experiments described in the previous sections. Controlling a constant amplitude of the peak at one half of the excitation frequency can minimize the repulsive interaction forces, which can prevent the damage to soft materials, while imaging them in tapping mode.

3.5 Summary

The period-doubling phenomenon is studied in detail through experiments and numerical studies in micro-scale AFM systems. It is observed that period-doubling bifurcations take place in the micro-scale system, around the same excitation frequency window, as previously observed in the macro-scale system. The feasibility of carrying out AFM operation at an off-resonance excitation condition has been demonstrated in this chapter. This is a new method of operation of the AFM, where nonlinear phenomenon can be used to maintain grazing contact.

Chapter 4

Discontinuity Induced Bifurcations

In this chapter, the period-doubling bifurcations reported in the previous chapters are studied in more detail by using zero-time discontinuity maps (ZDMs) and local Poincaré maps.

The bifurcations observed in the experimental and numerical studies can be attributed to grazing impacts with the separating boundary. These types of impacts can be studied by using discontinuity maps (e.g., Dankowicz and Nordmark, 2000; Dankowicz *et al.*, 2007; di Bernardo *et al.*, 2001a,b). This type of bifurcations occur when a trajectory grazes or makes tangential contact with the switching boundary. It has been noted in the previous chapters that due to the discontinuous nature of the attractive-repulsive forces on the cantilever's tip, the system has a non-smooth characteristic. In order to construct the ZDM, the repulsive force-profile has been modeled as a quadratic function, that matches very well with the DMT contact forces used in the simulations described in the previous chapters. Near-grazing dynamics is examined by carrying out local analyses with Poincaré map constructions to show that the observed period-doubling events are possible for the considered nonlinear tip interactions. In the corresponding experiments, the stability of the observed grazing periodic orbits has been assessed by constructing the Jacobian matrix from the experimentally obtained Poincaré map. The nondimensional parameters are

compared for both the micro-scale and macro-scale cases.

In the next section, a force profile that is used to facilitate the analysis is described. The local maps descriptive of grazing dynamics are developed in the next section. An experimental procedure used to determine the stability of the macro-scale experimental data is presented in the following section.

4.1 Piecewise nonlinear force model

The interaction forces in the macro and micro-scale systems are approximated with a nonlinear piecewise function to make it amenable to the discontinuity mapping technique presented later in this work. It is noted that the numerical results obtained with the modified force profile remain the same as the obtained results with DMT and van der Waals forces in the previous chapters (Chakraborty and Balachandran, 2012).

The original tip-sample force profile for macro-scale studies described in the Chapter 2 are given by

$$F(z) = \begin{cases} -\frac{K_M}{(z+A_0)^2} & \text{for } z > 0 \\ -\frac{K_M}{(A_0)^2} + K_E(-z)^{1.5} & \text{for } z \leq 0 \end{cases} \quad (4.1)$$

In this study, the force given by Eq. (4.1) is approximated by Eq. (4.2):

$$F(z) = \begin{cases} -\frac{K_M}{(z+A_0)^2} & \text{for } z > 0 \\ -\frac{K_M}{(A_0)^2} + K_1 z^2 - K_2 z & \text{for } z \leq 0 \end{cases} \quad (4.2)$$

where K_M is the constant due to an attractive magnetic force, and K_1 and K_2 are the constants associated with elastic impacts. These constants are determined

to match the DMT contact force profile used in the previous chapters. The other parameters are same as presented in Chapter 2. The comparison between the two force profiles given by Eq. (4.2) and Eq. (4.1) are shown in Fig. 4.1.

At the micro-scale, the author assumes a similar tip-sample force interaction as at the macro-scale. The attractive part of the tip sample interaction is given by the van der Waals attractive force. The repulsive part of this interaction force is approximated by a quadratic force. The constants related to the quadratic force profile is determined by comparing this profile with the Derjaguin-Muller-Toporov (DMT) contact force profile for a Si-Si combination. As presented earlier in Chapter 3, the van der Waals and DMT tip sample interaction force is given by Eq. (4.3), where H is the Hamaker Constant, R is the tip radius, and E^* is the effective elastic modulus of the tip-sample combination.

$$F(z) = \begin{cases} -\frac{HR}{6z^2} & \text{for } z > a_0 \\ -\frac{HR}{6a_0^2} + \frac{4}{3}E^*\sqrt{R}(a_0 - z)^{1.5} & \text{for } z \leq a_0 \end{cases} \quad (4.3)$$

A quadratic repulsive force profile is used instead of the Hertzian contact force profile given in Eq. (4.3). The used force profile is:

$$F(z) = \begin{cases} -\frac{HR}{6z^2} & \text{for } z > a_0 \\ -\frac{HR}{6a_0^2} + K_1(z - a_0)^2 - K_2(z - a_0) & \text{for } z \leq a_0 \end{cases} \quad (4.4)$$

The two force profiles given in Eq. (4.3) and Eq. (4.4) are compared in Fig. 4.2. The constants related to the repulsive force are chosen to match the DMT contact force profile as shown in the figure. The parameter values used in the simulations are the same as in Chapter 3.

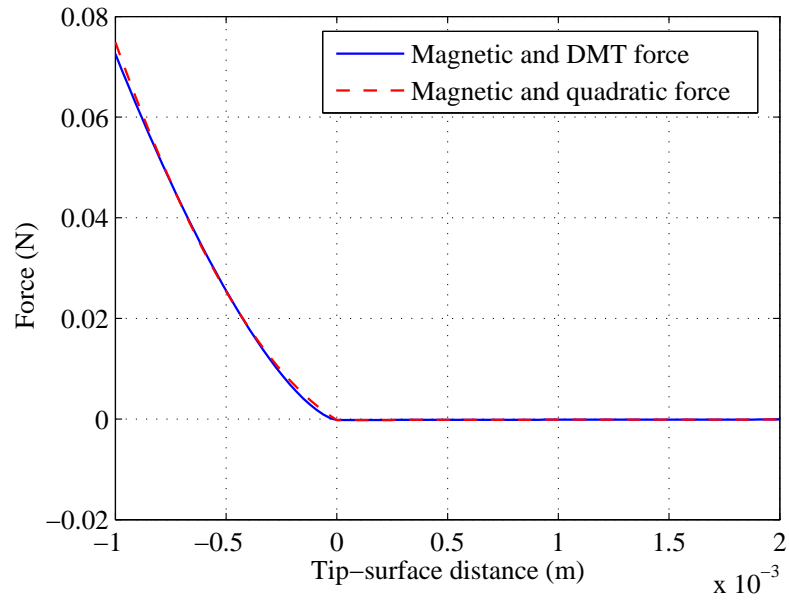


Figure 4.1: Comparison of force profiles in macro-scale system.

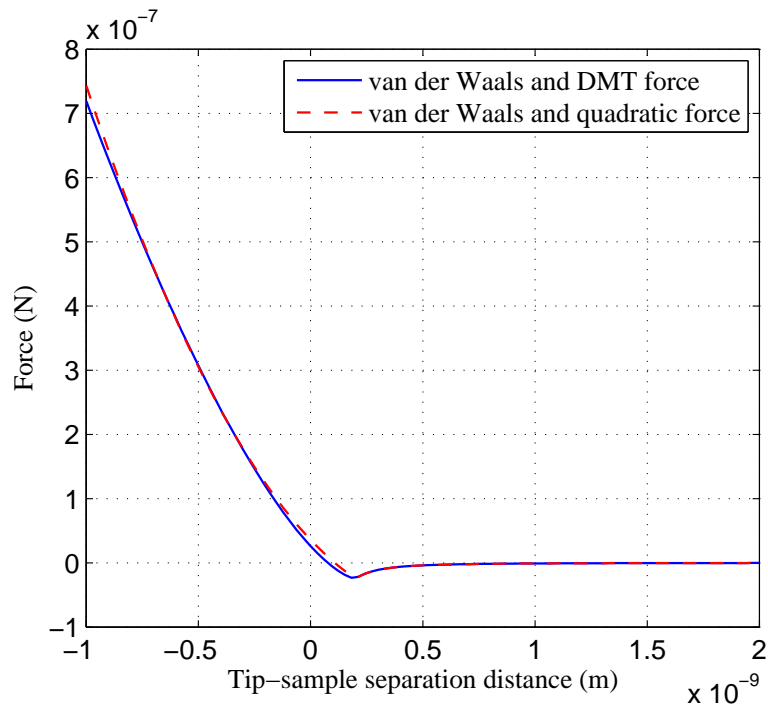


Figure 4.2: Comparison of force profiles in micro-scale AFM operation.

In addition to the nondimensional parameters listed in Chapter 2, additional parameters are introduced for the new force profile; that is,

$$\kappa_1 = \frac{K_1}{\rho A \omega_n^2}, \quad \kappa_2 = \frac{K_2}{\rho A L \omega_n^2}.$$

The nondimensional tip-sample force f_{ts} (for both the macro-scale and micro-scale systems) are given by

$$f_{ts}(\bar{z}) = \begin{cases} -\frac{\lambda}{(\bar{z} + \bar{\eta} + \xi_0)^2} & \text{for } \bar{z} + \bar{\eta} > 0 \\ -\frac{\lambda}{(\xi_0 + \eta_0)^2} + \kappa_1(-\bar{z} - \bar{\eta})^2 & \\ +\kappa_2(-\bar{z} - \bar{\eta}) & \text{for } \bar{z} + \bar{\eta} \leq 0 \end{cases} \quad (4.5)$$

Here, \bar{z} is the nondimensional displacement of the cantilever tip and it is given by

$$\bar{z} = \bar{w} + \nu \cos(\Omega\tau).$$

The tip-sample force in both macro-scale and micro-scale systems are given by Eq. (4.5). For the micro-scale case,

$$\bar{\eta} = \eta - \eta_0,$$

$$\xi_0 = 0.$$

On the other hand, for the macro-scale case, Eq. (4.5) can be applied by assuming

$$\eta_0 = 0,$$

$$\bar{\eta} = \eta.$$

The computational model used for simulations of the systems is given by Eq. (2.8) in Chapter 2, wherein the tip sample forces are given by Eq. (4.5). It is

observed that the new force profile generates similar responses of the cantilever tip as presented through the numerical results of Chapter 2 and Chapter 3.

The bifurcations reported in this dissertation are due to grazing type of contact between the tip and the sample. The equation of motion given by Eq. (2.8) along with the tip-sample forces described by Eq. (4.5) is put in the following state-space form

$$\dot{\mathbf{x}} = \begin{cases} F_1(\mathbf{x}) & \text{for } H(\mathbf{x}) > 0 \\ F_2(\mathbf{x}) & \text{for } H(\mathbf{x}) \leq 0 \end{cases} \quad (4.6)$$

and local analysis is carried out with this system. In Eq. (4.6), $H(x) = 0$ is the switching boundary of the system. The construction of local maps near grazing is explored in detail in the next section.

Table 4.1: Nondimensional parameter values used in simulations

Micro-scale case		Macro-scale case	
ν	8.43×10^{-4}	ν	1.49×10^{-3}
η	7.75×10^{-4}	η	2.02×10^{-3}
η_0	4.44×10^{-7}	ξ_0	1.69×10^{-2}
λ	1.36×10^{-17}	λ	7.63×10^{-9}
κ_1	5.11×10^2	κ_1	1.91×10^8
κ_2	1.14×10^0	κ_2	2.93×10^2

4.2 Discontinuity maps near grazing

A grazing event occurs when a periodic orbit grazes (i.e., makes tangential contact) a boundary Σ that separates two regions of state space, as shown in Fig. 4.3. Here, a zero-speed impact with the compliant material corresponds to the boundary Σ , which separates regions governed by different dynamics in the state space. In Fig. 4.3, orbit A represents the system response prior to grazing, orbit B represents the response at grazing condition (i.e., the solution grazes the switching boundary Σ), and orbit C represents a possible scenario after grazing contact.

The boundary Σ separates the regions S_1 and S_2 , where S_2 corresponds to

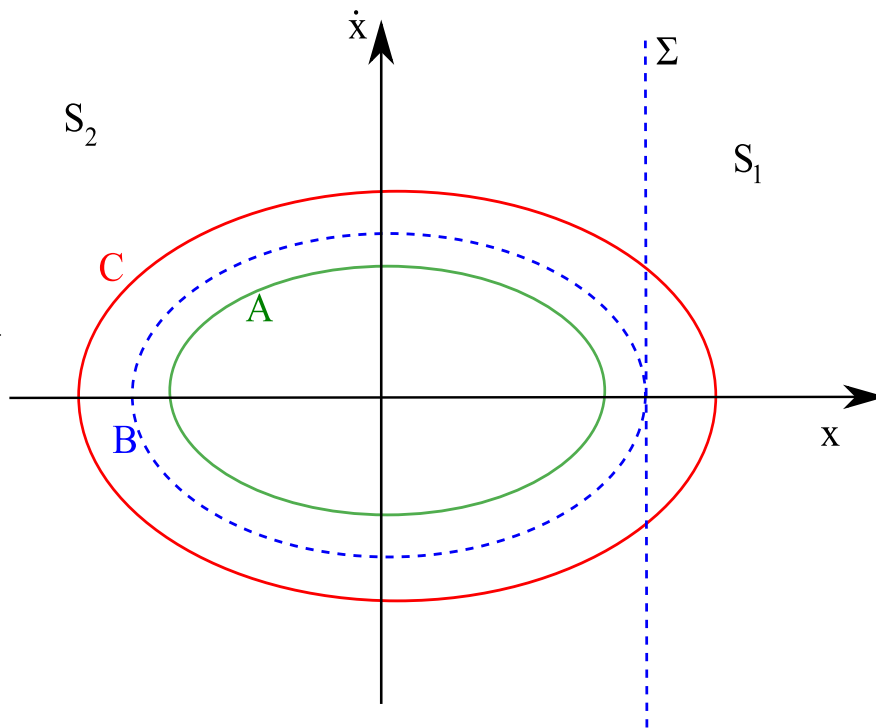


Figure 4.3: Illustration of grazing bifurcation. Orbits A , B and C are representative system responses, when a scalar control parameter is quasi-statically varied.

the region of non-contact dynamics. The qualitative change experienced by a stable periodic orbit when it experiences a grazing impact is termed a *grazing bifurcation*. When a system undergoes a grazing contact, a wide variety of phenomena has been observed in the post-grazing state, including periodic oscillations, quasi-periodic oscillations, period adding, and chaotic oscillations.

di Bernardo *et al.* (2001a) derived a formula for local Poincaré maps at the grazing point by using Taylor series expansions and discontinuity maps. The author also uses a similar approach to derive the local Poincaré maps of orbits of the considered system. As introduced in earlier work by Dankowicz and Nordmark (2000), the zero-time discontinuity mapping (ZDM) is a mapping that can be used to take into account the dynamics in the vicinity of a grazing trajectory, and this mapping provides a correction to the Poincaré map due to the presence of a discontinuity. Let F_i be the vector field in the region S_i , H be the switching function such that $\Sigma : H = 0$, and \langle, \rangle stand for the dot product of two vectors and $\nabla = \frac{\partial}{\partial x}$. Following di Bernardo *et al.* (2001a), it is assumed for the grazing condition at $x = 0$, without any loss of generality that

$$H(0) = 0, \quad \langle \nabla H, F_i \rangle = 0. \quad (4.7)$$

The second condition ensures the trajectory F_i is tangential to the boundary $H = 0$. Here, $\langle \nabla H, F_i \rangle$ is calculated at the grazing point $x = 0$.

The flow in the two regions separated by $H(x) = 0$, is illustrated in Fig. 4.4. The state space is separated in two regions S_1 and S_2 by the boundary $H(x) = 0$. The zero-time discontinuity map (ZDM) is derived for this system. Let T be the

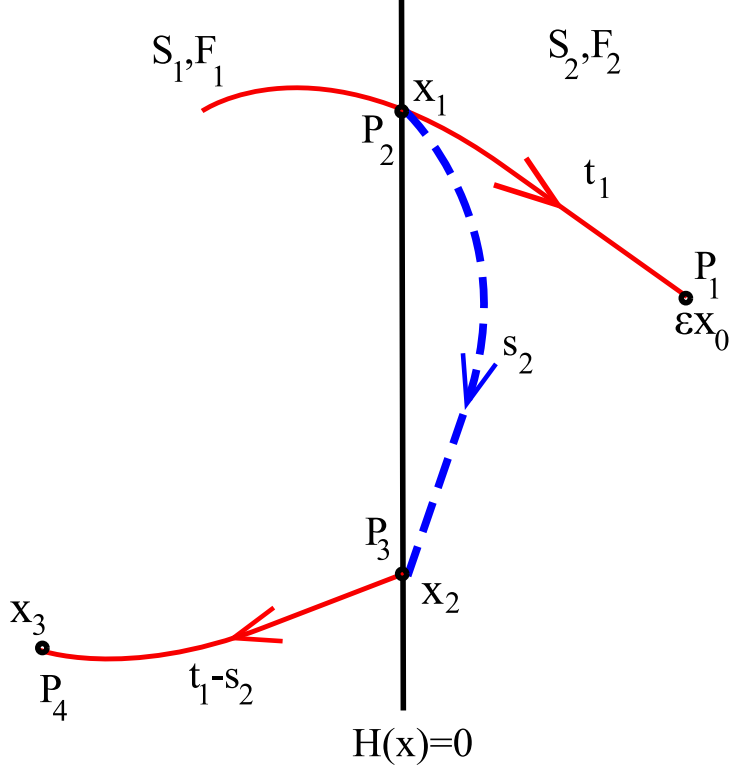


Figure 4.4: Illustration of discontinuity map near the grazing point.

driving period and mT be the period of the grazing limit cycle. If it is assumed that the switching boundary does not exist, the Poincaré map π_{per} can be found numerically at the grazing point by going from $t = 0$ to $t = mT$. Then, the ZDM π_{zdm} can be applied as a correction term for trajectories that “graze” the boundary.

The local Poincaré map is given by

$$\pi = \begin{cases} \pi_{per} & \text{if not crossing } H \\ \pi_{zdm} \circ \pi_{per} & \text{if crossing } H \end{cases} \quad (4.8)$$

The ZDM is defined as $\pi_{zdm} : \epsilon x_0 \mapsto x_3$. The discontinuity map π_{zdm} is a correction made to the local Poincaré map π_{per} due to the presence of the discontinuity or the switching manifold $H = 0$. For soft impacts, this construction was used to obtain

a local Poincaré map for a corner colliding trajectory by Long *et al.* (2008). The discontinuity map π_{zdm} is the map obtained by considering the zero-time correction needed to take into account the presence of discontinuity.

In Fig. 4.4, for purposes of understanding, the flow under the influence of F_1 (non-contact dynamics) is represented by a solid line, and the influence of F_2 (contact dynamics) is represented by a dashed line. The mapping $\epsilon x_0 \mapsto x_3$ is split into three pieces, as follows:

1. from ϵx_0 to x_1 during the time interval $[0, -t_1]$ under the action of the vector field F_1
2. from x_1 to x_2 during the time interval $[-t_1, -t_1 + s_2]$ under the action of the vector field F_2
3. from x_2 to x_3 during the time interval $[-t_1 + s_2, 0]$ under the action of the vector field F_1 .

Here, t_1 , s_2 , and $t_1 - s_2$ are considered to be positive and the total time is zero for the mapping $\epsilon x_0 \mapsto x_3$. Furthermore, the quantities ϵ , x_1 , x_2 , x_3 , t_1 , and s_2 are assumed to be “small” to facilitate Taylor series expansions. In Fig. 4.4, the trajectory hits the discontinuity at P_2 . If it is assumed that the boundary $H(x) = 0$ does not exist, then the trajectory evolves to P_1 under the influence of F_1 . Now the correction to ϵx_0 is applied because of the existence of the boundary. For the considered system, the force field is continuous at grazing; that is, $F_1 = F_2$ at grazing point. Without any loss of generality, the illustration in Fig. 4.4 will be used, as discussed next.

(1) evolution from ϵx_0 to x_1

Taylor series expansions are used to analyze the flow of the solution. Without loss of generality, the flow under the influence of vector field F_i for a time t , starting from the initial position x is given by

$$\begin{aligned} \phi_i(x, t) &= x + F_i t + \frac{1}{2} \frac{\partial F_i}{\partial x} F_i t^2 + \frac{\partial F_i}{\partial x} x t \\ &+ \frac{1}{6} \left(\frac{\partial^2 F_i}{\partial x^2} F_i^2 + \left(\frac{\partial F_i}{\partial x} \right)^2 F_i \right) t^3 + \frac{1}{2} \frac{\partial^2 F_i}{\partial x^2} x^2 t \\ &+ \frac{1}{2} \left(\frac{\partial^2 F_i}{\partial x^2} F_i + \left(\frac{\partial F_i}{\partial x} \right)^2 \right) x t^2 + O(t^4, x^2 t^2, x t^3). \end{aligned} \quad (4.9)$$

This form of Eq. (4.9) will be used here to analyze the motion in this section. Let the solution of Eq. (4.6) with the vector field F_i ($i=1,2$), which is started from the initial condition x_0 , be written as $\phi_i(x_0, t)$ at time t . Then, the Taylor expansion of x_1 about the grazing point becomes

$$\begin{aligned} x_1 &= \phi_1(\epsilon x_0, -t_1) \\ &= \epsilon x_0 - t_1 F_1 + t_1^2 a_1 - \epsilon t_1 b_1 x_0 - c_1 t^3 - \epsilon^2 d_1 x_0^2 t_1 \\ &\quad + \epsilon e_1 x_0 t_1^2 + O(\epsilon^4, t_1^4, \epsilon^2 t_1^2, \epsilon t_1^3) \end{aligned} \quad (4.10)$$

where a_i, b_i, c_i, \dots can be found from Eq. (4.9), $i = 1, 2$, and $x = [x_1 \ x_2]^T$. t_1 is defined as the time needed by the perturbed trajectory to cross the switching manifold at $x = x_1$. As the switching boundary is assumed to be a straight line, the function H has the property

$$\nabla^n H(\tilde{x}) = 0 \quad \forall \tilde{x} \in \mathfrak{R}^2 \quad n \geq 2 \quad (4.11)$$

and it follows that

$$H(x_1) = H(0) + \langle \nabla H, x_1 \rangle = \langle \nabla H, x_1 \rangle \quad (4.12)$$

At the point x_1 ,

$$H(x_1) = 0. \quad (4.13)$$

Combining Eqs. (4.12) and (4.13), one has

$$\langle \nabla H, x_1 \rangle = 0. \quad (4.14)$$

On substituting the Taylor expansion of Eq. (4.10) into Eq. (4.14), the result is

$$\begin{aligned} t_1 &= \gamma_1 \epsilon^{\frac{1}{2}} + \gamma_2 \epsilon + \gamma_3 \epsilon^{\frac{3}{2}} + O(\epsilon^2), \\ \gamma_1 &= \sqrt{-\frac{\langle \nabla H, x_0 \rangle}{\langle \nabla H, a_1 \rangle}}, \quad \gamma_2 = \frac{1}{2} \frac{\langle \nabla H, b_1 x_0 \rangle + \langle \nabla H, c_1 \gamma_1^2 \rangle}{\langle \nabla H, a_1 \rangle}, \\ \gamma_3 &= \frac{-1}{2 \langle \nabla H, a_1 \gamma_1 \rangle} [\langle \nabla H, a_1 \gamma_2^2 \rangle - \langle \nabla H, b_1 x_0 \gamma_2 \rangle \\ &\quad - \langle \nabla H, 3c_1 \gamma_1^2 \gamma_2 \rangle + \langle \nabla H, e_1 x_0 \gamma_1^2 \rangle], \\ x_1 &= \chi_1 \epsilon^{\frac{1}{2}} + \chi_2 \epsilon + \chi_3 \epsilon^{\frac{3}{2}} + O(\epsilon^2) \\ \chi_1 &= -\gamma_1 F_1 \epsilon^{\frac{1}{2}}, \quad \chi_2 = x_0 - \gamma_2 F_1 + \gamma_1^2 a_1 \\ \chi_3 &= -F_1 \gamma_3 - b_1 x_0 \gamma_1 + 2a_1 \gamma_1 \gamma_2 - c_1 \gamma_1^3. \end{aligned} \quad (4.15)$$

(2) evolution from x_1 to x_2

Following the same procedure as before, it is found that

$$\begin{aligned} x_2 &= \phi_2(x_1, s_2) = x_1 + F_2 s_2 + a_2 s_2^2 + b_2 s_2 x_1 \\ &\quad + c_2 s_2^3 + d_2 x_1^2 s_2 + e_2 x_1 s_2^2 + O(\epsilon^2), \end{aligned} \quad (4.16)$$

$$\langle \nabla H, x_2 \rangle = 0 \quad (4.17)$$

Hence, it follows that

$$\begin{aligned}
s_2 &= \nu_1 \epsilon^{\frac{1}{2}} + \nu_2 \epsilon + \nu_3 \epsilon^{\frac{3}{2}} + O(\epsilon^2) \\
\nu_1 &= \frac{\langle \nabla H, b_2 F_1 \rangle}{\langle \nabla H, a_2 \rangle} \gamma_1, \\
\nu_2 &= \frac{-\nu_1}{\langle \nabla H, b_2 \chi_1 \rangle + \langle \nabla H, 2a_2 \nu_1 \rangle} [\langle \nabla H, d_2 \chi_1^2 \rangle \\
&\quad + \langle \nabla H, c_2 \gamma_1^2 \rangle + \langle \nabla H, e_2 \chi_1 \gamma_1 \rangle + \langle \nabla H, b_2 \chi_2 \rangle]
\end{aligned}$$

Here, the denominator in the expression of ν_1 is assumed to be non-zero.

(3) evolution from x_2 to x_3

The Taylor expansion of x_3 results in

$$\begin{aligned}
x_3 &= \phi(x_2, t_1 - s_2) = x_1 + (F_2 - F_1)s_2 + F_1 t_1 + a_2 s_2^2 \\
&\quad + b_2 x_1 s_2 + a_1 (t_1 - s_2)^2 + b_1 (x_1 + F_2 s_2)(t_1 - s_2) + O(\epsilon^{\frac{3}{2}})
\end{aligned}$$

The considered system has a continuous form at the point of grazing discontinuity.

At the grazing point $F_1 = F_2 := F$. This condition gives rise to a $3/2$ singularity in the ZDM. Due to the continuous nature of the vector field at grazing point the $O(\epsilon^{\frac{1}{2}})$ terms go to zero, and $O(\epsilon)$ coefficients become x_0 . Further calculation of $O(\epsilon^{\frac{3}{2}})$ terms yields the ZDM. Therefore, the ZDM has a leading order term of the form

$$\begin{aligned}
\pi_{zdm} \quad \tilde{x} \mapsto \tilde{x} &+ V_1 \langle \nabla H, \tilde{x} \rangle^{\frac{3}{2}} + V_2 \tilde{x} \langle \nabla H, \tilde{x} \rangle^{\frac{1}{2}} \\
&+ V_3 \left\langle \nabla H, \frac{\partial F_2}{\partial \tilde{x}} \tilde{x} \right\rangle \langle \nabla H, \tilde{x} \rangle^{\frac{1}{2}} + O(\epsilon^2)
\end{aligned} \tag{4.18}$$

where

$$V_1 = \frac{2}{\langle \nabla H, \frac{\partial F_1}{\partial \tilde{x}} F \rangle^{\frac{3}{2}}} \left[\frac{1}{3} \left(\frac{\partial^2 F_2}{\partial \tilde{x}^2} - \frac{\partial^2 F_1}{\partial \tilde{x}^2} \right) F^2 \right]$$

$$\begin{aligned}
& + \frac{\partial F_2}{\partial \tilde{x}} \frac{\partial F_1}{\partial \tilde{x}} F - \frac{1}{3} \left[\left(\frac{\partial F_1}{\partial \tilde{x}} \right)^2 + 2 \left(\frac{\partial F_2}{\partial \tilde{x}} \right)^2 \right] F \\
& - \frac{1}{\langle \nabla H, \frac{\partial F_2}{\partial \tilde{x}} F \rangle} \left(\frac{\partial F_2}{\partial \tilde{x}} - \frac{\partial F_1}{\partial \tilde{x}} \right) F \left[\frac{1}{3} \left\langle \nabla H, \frac{\partial^2 F_2}{\partial \tilde{x}^2} F^2 \right\rangle \right. \\
& \left. + \left\langle \nabla H, \frac{\partial F_2}{\partial \tilde{x}} \frac{\partial F_1}{\partial \tilde{x}} F_1 \right\rangle - \frac{2}{3} \left\langle \nabla H, \left(\frac{\partial F_2}{\partial \tilde{x}} \right)^2 F \right\rangle \right] \\
V_2 &= \frac{2\sqrt{2}}{\sqrt{\langle \nabla H, \frac{\partial F_1}{\partial \tilde{x}} F \rangle}} \left(\frac{\partial F_2}{\partial \tilde{x}} - \frac{\partial F_1}{\partial \tilde{x}} \right) \\
V_3 &= \frac{2\sqrt{2}}{\langle \nabla H, \frac{\partial F_2}{\partial \tilde{x}} F \rangle \sqrt{\langle \nabla H, \frac{\partial F_1}{\partial \tilde{x}} F \rangle}} \left(\frac{\partial F_2}{\partial \tilde{x}} - \frac{\partial F_1}{\partial \tilde{x}} \right) F
\end{aligned}$$

It is assumed that the Poincaré map π_{per} is given by

$$\pi_{per} : \tilde{x} \mapsto A\tilde{x} \quad (4.19)$$

Combining Eqs. (4.18) and (4.19), the local map at the grazing point is given by

$$\begin{aligned}
\pi &= \pi_{per} \circ \pi_{zdm} : \\
\tilde{x} &\mapsto \begin{cases} A\tilde{x} & \text{if not crossing } H \\ A \left(\tilde{x} + V_1 \langle \nabla H, \tilde{x} \rangle^{\frac{3}{2}} + V_2 \tilde{x} \langle \nabla H, \tilde{x} \rangle^{\frac{1}{2}} \right. \\ \left. + V_3 \langle \nabla H, \frac{\partial F_2}{\partial \tilde{x}} \tilde{x} \rangle \langle \nabla H, \tilde{x} \rangle^{\frac{1}{2}} \right) & \text{if crossing } H \end{cases} \quad (4.20)
\end{aligned}$$

The author applies this discontinuity map to the current system. Since the bound-

ary of the discontinuity is $\bar{\eta} + \bar{z} = 0$ (see Eq. (4.5)), a new variable $x = \bar{\eta} + \bar{z}$ is introduced. Then, the boundary of the discontinuity is given by

$$H(x) : x = 0$$

and the grazing condition occurs at $x = 0$.

Revisiting the non-autonomous system Eq. (2.8), the author introduces the additional variable $\theta = \Omega\tau$ as an additional state; that is,

$$\mathbf{x} = \begin{pmatrix} x_1 \\ x_2 \\ x_3 \end{pmatrix} = \begin{pmatrix} x \\ \dot{x} \\ \theta \end{pmatrix}$$

Then, in state-space form, one has

$$\begin{pmatrix} \dot{x}_1 \\ \dot{x}_2 \\ \dot{x}_3 \end{pmatrix} = \begin{pmatrix} x_2 \\ [\frac{1}{m_1}\{-k_1(x_1 - \bar{\eta} - \nu \cos x_3) \\ -c_1(x_2 + \Omega\nu \sin x_3) + \\ \psi_1(\int_0^1 \psi_1 d\bar{s}) \Omega^2\nu \cos x_3 \\ -\psi_1^2 \frac{\lambda}{(x_1 + \eta_0 + \xi_0)^2}\} - \Omega^2\nu \cos x_3] \\ \Omega \end{pmatrix}$$

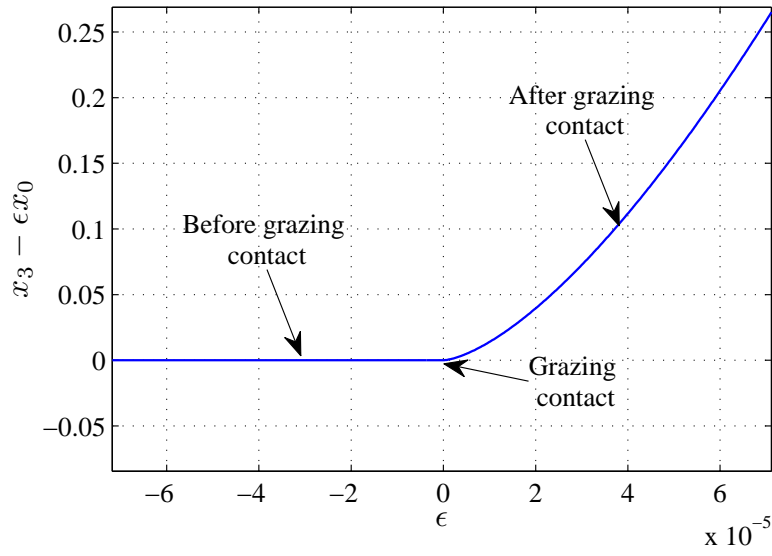
for $H(\mathbf{x}) > 0$ (4.21)

and

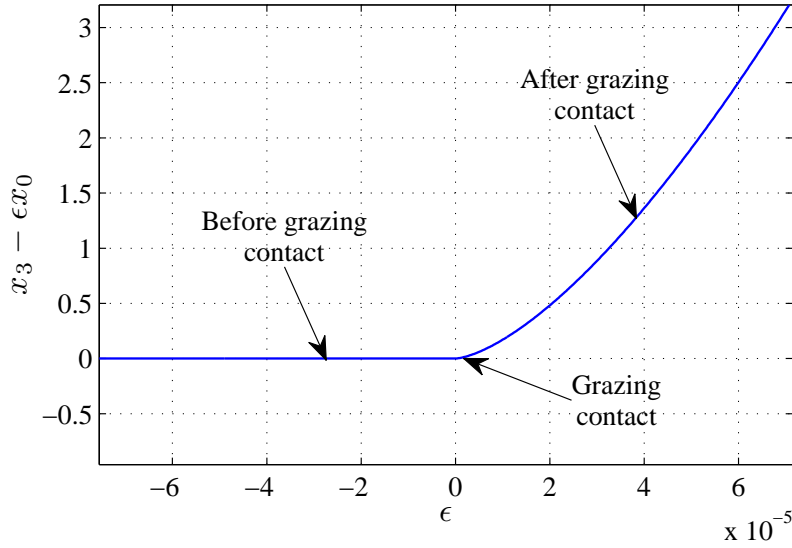
$$\begin{pmatrix} \dot{x}_1 \\ \dot{x}_2 \\ \dot{x}_3 \end{pmatrix} = \begin{pmatrix} x_2 \\ [\frac{1}{m_1}\{-k_1(x_1 - \bar{\eta} - \nu \cos x_3) \\ -c_1(x_2 + \Omega\nu \sin x_3) + \psi_1(\int_0^1 \psi_1 d\bar{s}) \\ \Omega^2\nu \cos x_3 - \\ \psi_1^2 \frac{\lambda}{(\xi_0 + \eta_0)^2} + \psi_1^2(\kappa_1 x_1^2 \\ -\kappa_2 x_1)\} - \Omega^2\nu \cos x_3] \\ \Omega \end{pmatrix}$$

for $H(\mathbf{x}) \leq 0$ (4.22)

The systems given by Eq. (4.21) and Eq. (4.22) describe the vector fields F_1 and F_2 used in Eq. (4.6). The system given by Eq. (2.8) is used to construct the Poincaré map given by Eq. (4.20).



(a)



(b)

Figure 4.5: (a) Illustration of discontinuity map near the grazing bifurcation point for macro-scale system. (b) Illustration of discontinuity map near the grazing bifurcation point for micro-scale system.

Discontinuity maps are numerically computed as discussed in Section 4.2, for both the macro-scale and micro-scale systems with parameter values as given in Table 4.1. The obtained variations of different solutions are plotted in Fig. 4.5 with respect to the parameter ϵ .

Due to the nature of the attractive-repulsive forces acting on the cantilever tip, the vector field is the same on both sides, at the grazing point, and there is a discontinuity in the first or second derivative of the flow, so the ZDM shows a 3/2 type singularity at the grazing point as shown in previous studies, for example, Dankowicz and Nordmark (2000).

4.3 Experimental study of stability

The author analyzed the stability of the periodic orbits observed in the macro-scale experiments by using an experimental approach used by Ing *et al.* (2008). In theory, stability information for a periodic orbit can be obtained from the eigenvalues of the Jacobian matrix related to a fixed point of the corresponding map of the periodic motion. If the eigenvalues of the Jacobian lie within the unit circle, from the local analysis, then the fixed point and the corresponding periodic solution are stable (e.g., Nayfeh and Balachandran, 1995). This concept is illustrated in the following general discussion of the stability of maps. First, a general map is considered

$$x_{k+1} = F(x_k). \tag{4.23}$$

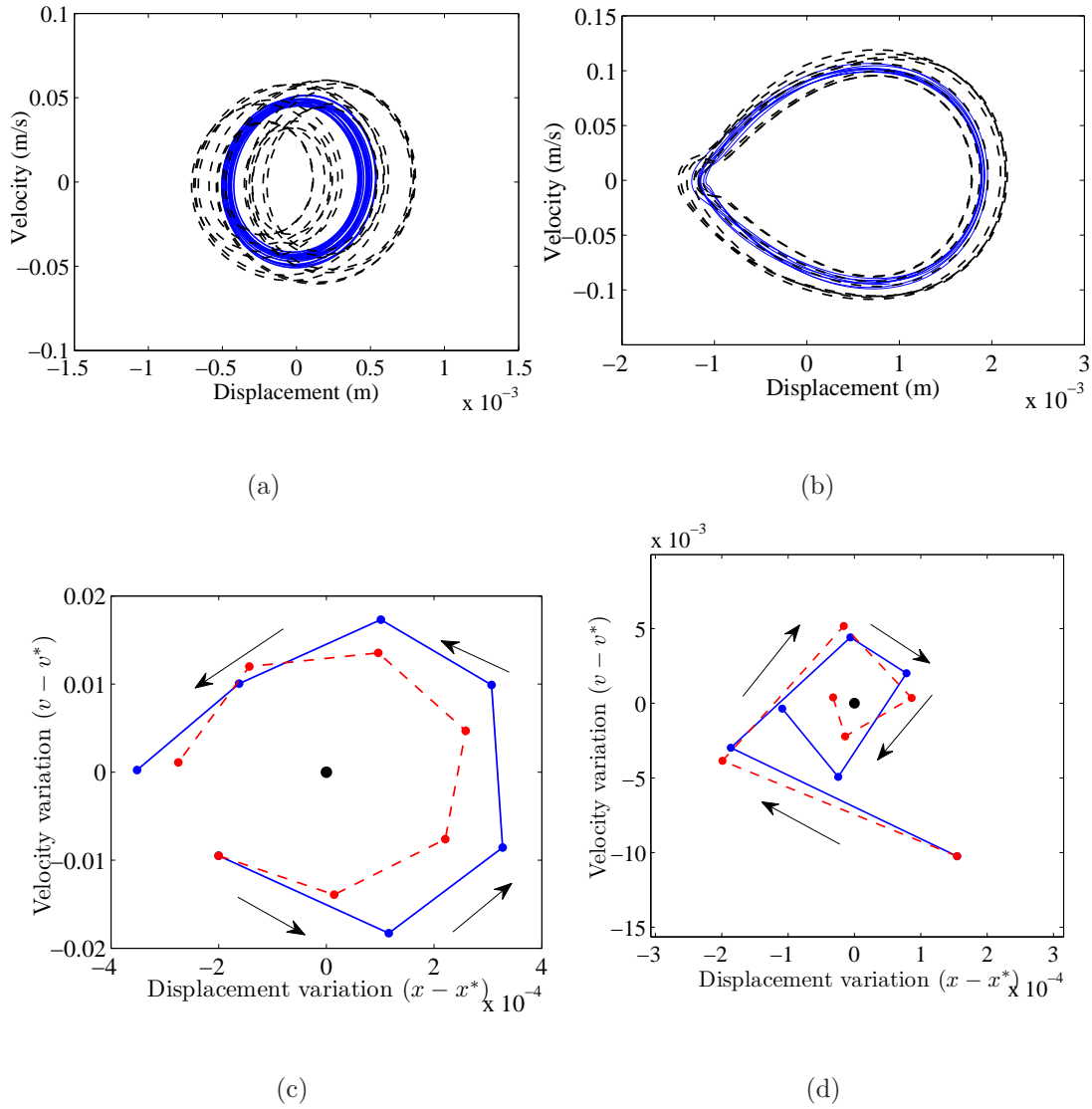


Figure 4.6: Experimentally obtained phase portraits for the perturbed system (dashed line), and the unperturbed system (solid line): (a) unconstrained motion and (b) constrained motion. Iterations of Poincaré map: (c) unconstrained motion and (d) constrained motion. The experimentally obtained points are connected by solid lines and the points obtained from the linear curve fit are joined by dashed lines.

Now, the stability of a fixed point of this map $x = x^*$, can be determined by perturbing Eq. (4.23) around the fixed point:

$$x^* + y_{k+1} = F(x^* + y_k). \quad (4.24)$$

Taylor expansion (after keeping only the linear terms) of Eq. (4.24) gives rise to the linear equation

$$y_{k+1} = D_x F|_{x=x^*} y_k. \quad (4.25)$$

The stability of the fixed point depends on the eigenvalues of the Jacobian matrix $D_x F$. If the eigenvalues lie within the unit circle, the fixed point x^* and the corresponding periodic orbit are stable.

For the considered experimental system, a periodic solution corresponds to a fixed point of a Poincaré map, and the stability of that fixed point can be analyzed by experimentally determining the Jacobian matrix (assuming linear evolution around the fixed point for small perturbations). In order to experimentally study the stability of the periodic orbits, small perturbations are applied to the system. Physically, it was performed by a gentle tap on the tip of the cantilever. The results presented in this section were repeatable for multiple runs of the experiment. The phase portraits corresponding to the perturbed system (dashed line) and the unperturbed system (solid line) are shown in Figures 4.6(a) and 4.6(b) for cases without and with contact, respectively. Next, the Poincaré maps for the perturbed orbits are constructed for the two cases, and the difference between the Poincaré points of the perturbed orbit (x, v) and the Poincaré points of the original unperturbed orbit (x^*, v^*) are plotted in Figures 4.6(c) and 4.6(d). The local behaviors of the pertur-

bations around the point $(0, 0)$ are shown in these figures. The following linear map is assumed between any two subsequent points:

$$\begin{pmatrix} x_{n+1} - x^* \\ v_{n+1} - v^* \end{pmatrix} = \begin{bmatrix} a_{11} & a_{12} \\ a_{21} & a_{22} \end{bmatrix} \begin{pmatrix} x_n - x^* \\ v_n - v^* \end{pmatrix}.$$

The coefficients of the the matrix \mathbf{a} , namely, a_{11} , a_{12} , a_{21} , and a_{22} , are obtained through a least squares method, as the number of points are more than necessary to determine the constants. The linear curve fits, which are illustrated by the dotted lines in Figures 4.6(c) and 4.6(d), show a good match with the experimental data. The matrix \mathbf{a} is an experimental equivalent of the theoretically obtained Jacobian matrix for a perturbation around a fixed point. The eigenvalues of \mathbf{a} are $0.6188 \pm 0.7945i$ for the non-contact case, and $-0.1203 \pm 0.6318i$ for the contact case. Since the eigenvalues lie within the unit circle, it can be concluded that the observed periodic orbits, one before grazing contact and another after making grazing contact with the compliant material, are stable.

4.4 Summary

In this chapter, grazing dynamics of an impacting cantilever has been studied for a particular form of nonlinear interaction forces and off-resonance base excitations with local maps. For two different length-scale systems with similar nonlinear interaction forces, it is shown that there exists remarkable similarity in terms of the near-grazing dynamics through a combination of local analyses, experimental efforts, and numerical efforts. In particular, the commonality of the period-doubling

event close to a grazing contact is pointed out.

Chapter 5

Effects of Noise

The effects of noise on the impacting systems are discussed in this chapter; this work has been reported in the publications by the author (Chakraborty and Balachandran, 2011b,c). Noise is always present in physical systems, and the effects of noise can be important for micro-scale applications such as the AFM.

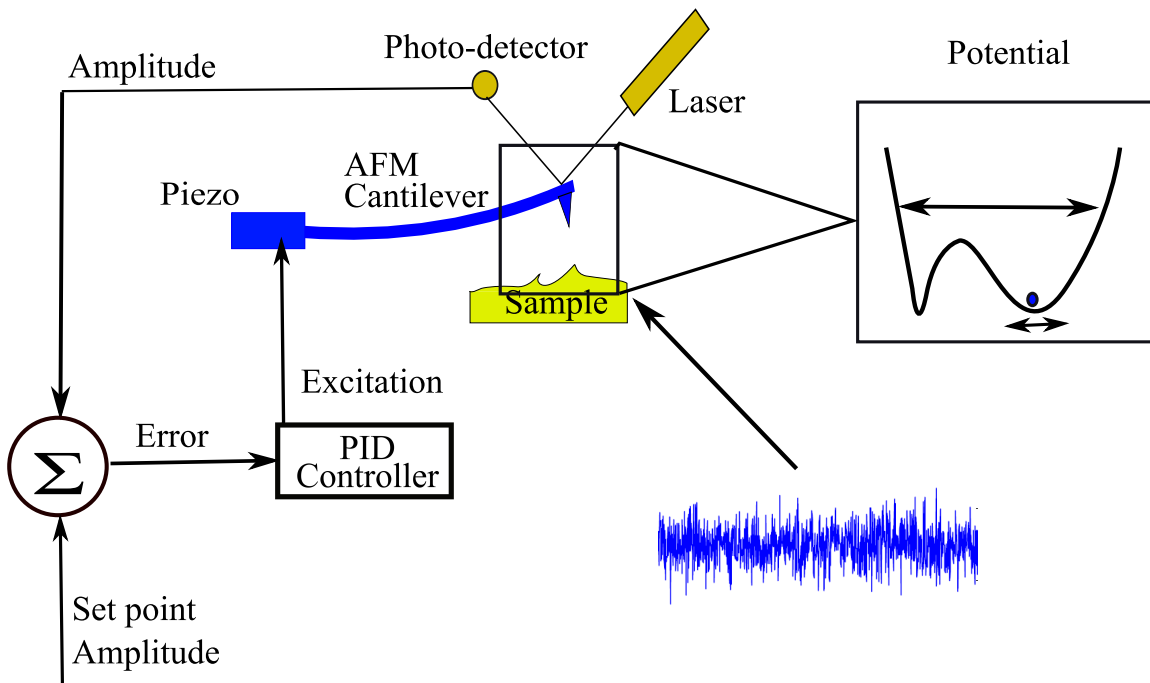


Figure 5.1: Potential sources of noise in an AFM system, which can be attributed to the controller, optical system, or a fabrication irregularity. Noise effects are important to understand due to the presence of the double-well potential in the cantilever-sample system.

In an AFM, noise can arise from the PID controller, the optical detection system, fabrication irregularities of the cantilever, thermal excitation, and so on. However, the effects of noise in an AFM system have received limited attention in the existing literature. In this work, experimental, numerical, and analytical efforts are directed to quantify and understand the effects of noise on an AFM operation. A representative schematic of an AFM system is shown in Fig. 5.1. Here, the noise present in the system is modeled as an additive white noise. Ideally, the noise can be assumed to take an additive form. The noise arising from the controller can result in a random signal addition to the harmonic excitation signal, the noise due to the optical detection system can be considered as an additive term to the harmonic excitation signal, and the noise due to fabrication irregularities as well as thermal noise or the laser shot noise can be modeled as additive random components in the governing system. The effect of added noise is of considerable interest, since the potential function associated with the AFM tip-sample combination has a double-well characteristic. The addition of an “optimum” amount of noise can make the trajectory of the tip hop between the potential wells. The system model with the additive noise term can be expressed by adding a noise term to Eq. (2.8); that is,

$$m_1\ddot{q}_1 + k_1q_1 + c_1\dot{q}_1 + \overbrace{f_b + \text{noise}} + f_c. \quad (5.1)$$

The explanations for the different terms used in Eq. (5.1) can be found in Chapter 2. A random component is added with the harmonic base excitation, so that the effects of noise can be examined by adding a known amount of noise through the input signal. As in the previous studies described in this dissertation, the author

started by examining the effects of added noise in the macro-scale experimental system, and then applied the findings to the micro-scale AFM system. This approach of studying the effects of additive noise will serve the dual purpose of helping understand the effects of noise already present in the system, and determining whether noise can be used in an advantageous fashion. Noise is added along with the harmonic excitation signal, when the excitation frequency is away from the resonance (in order to study the effects of noise on period-doubling and grazing phenomena discussed in the previous chapters). This work is motivated by a need to understand the effects of noise on the dynamics of the macro-scale system, and explore the applicability of the associated findings to an AFM system. It is observed in experimental and numerical studies that period-doubling bifurcations take place when white noise is added with a harmonic signal to form the input, when the harmonic signal was not sufficient to facilitate contact between the cantilever tip and the compliant material. A generic analytical framework based on the Fokker-Planck formalism is derived to examine the stochastic dynamics of a macro-scale cantilever system in the presence of noise. Moment evolution equations are obtained and studied. The numerical results obtained from these equations show qualitative agreement with the experimental and numerical observations. Guided by the observations made with the macro-scale system, the author carried out numerical simulations for the micro-scale AFM system and found that contact can be facilitated in a system in which there was previously no contact in the absence of a noise component in the input.

The experimental work in the macro-scale system is discussed in the next

section. Following that, the numerical simulation results are presented. An analytical framework for studying the stochastic dynamics is presented in Section 5.3. In this section, the Fokker-Planck equations are derived from the stochastic differential equation. A moment approximation is used to study the evolutions of the means of the dynamic variables with time, without explicitly solving for the Fokker-Planck equation. The numerical solution for the moment equations are presented in Section 5.7. The numerical results obtained for an AFM cantilever-sample combination is presented in Sections 5.5, 5.6, and 5.7.

5.1 Experimental studies and results

In this section, experimental results are described for the macro-scale system. The experimental arrangement follows that of previous arrangement described in earlier chapters. In these experiments, a known amount of noise is added to the system by the shaker, in addition to the harmonic input signal. The experiments were performed at a forcing frequency of 16 Hz, which is in between the first and the second natural frequency of the system (2.24 times the first natural frequency). For a purely harmonic base forcing, the beam tip does not make contact with the compliant surface, when the amplitude of the input signal is low. The corresponding base-excitation amplitude, and the phase portrait and spectrum associated with the cantilever's tip response are plotted in Fig. 5.2. A harmonic response at the same frequency as the excitation frequency is observed. The excitation frequency is chosen to be in between the first and the second natural frequencies of the system,

so that near-grazing contact can be identified by the associated period doubling phenomenon, as seen in the previous studies. In another experiment, Gaussian white noise was added along with the previously used harmonic base input. The noise is added through the shaker as an addition to the harmonic base excitation signal. Band-limited white noise can be added to the signal by using the Labview software that superimposes a random component of known noise intensity on the harmonic input. As the noise level in the base excitation reaches a threshold level, the cantilever starts to make contact with the compliant material and a response similar to a period-doubled response is observed; this can be used to identify grazing impacts as noted previously. The input excitation imparted to the cantilever structure, which includes the combination of the harmonic and random components, the response phase portrait, and the response spectrum are shown in Fig. 5.3. The response of the structure's tip shows that the basis frequency of the response is half the excitation frequency. In order to quantify the amount of noise necessary to induce contact between the beam tip and the surface, the author expresses the amount of noise in terms of the signal to noise ratio (SNR). This ratio, which is a measure of noise intensity in a signal, is defined as the ratio of signal power to noise power; that is,

$$SNR = \left(\frac{P_{signal}}{P_{noise}} \right).$$

For the experimental results, the SNR is obtained by individually calculating the power of the noise component and the power of the harmonic component. Here, it is noted that although theoretically white noise has infinite power, the author

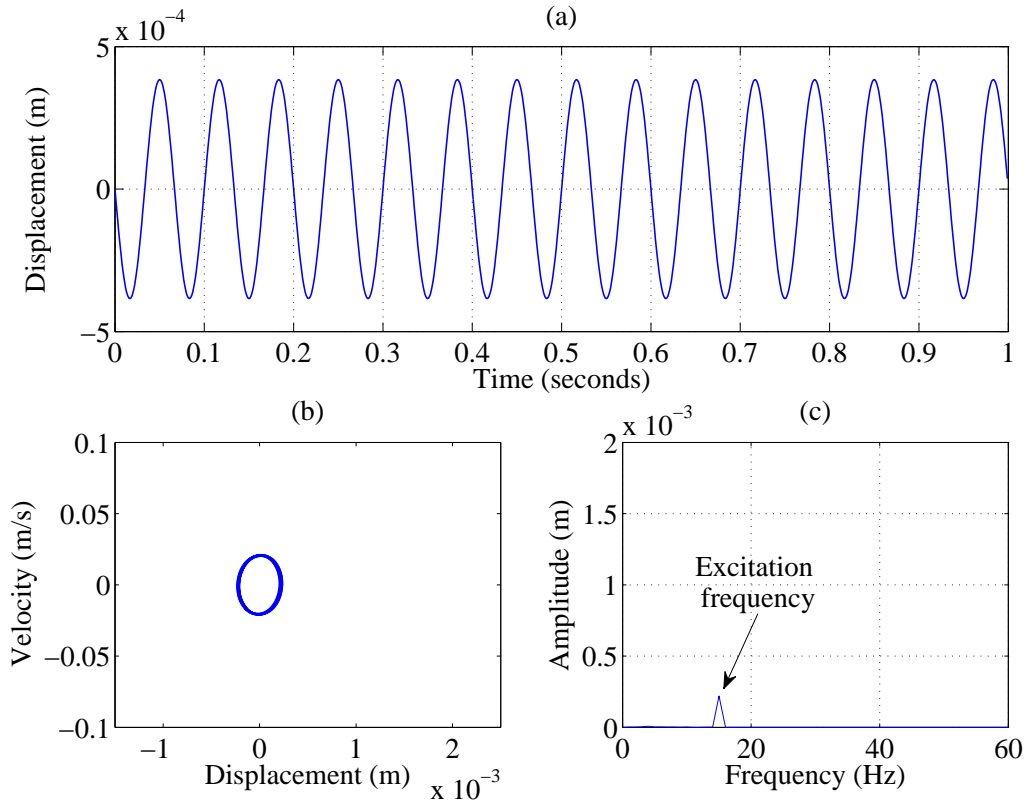


Figure 5.2: (a) Harmonic input from the shaker, (b) response phase portrait of the cantilever's tip, and (c) response spectrum. A single peak can be seen at the excitation frequency.

considers band-limited white noise, which has finite power. For the experimental results shown in Fig. 5.3, the SNR is determined to be 402.88.

5.2 Numerical studies and results

The numerical model developed in Chapter 2, is used in these simulations. The system under consideration (with added noise) is shown in Fig. 5.4. The random component is introduced in the numerical studies by adding a random component

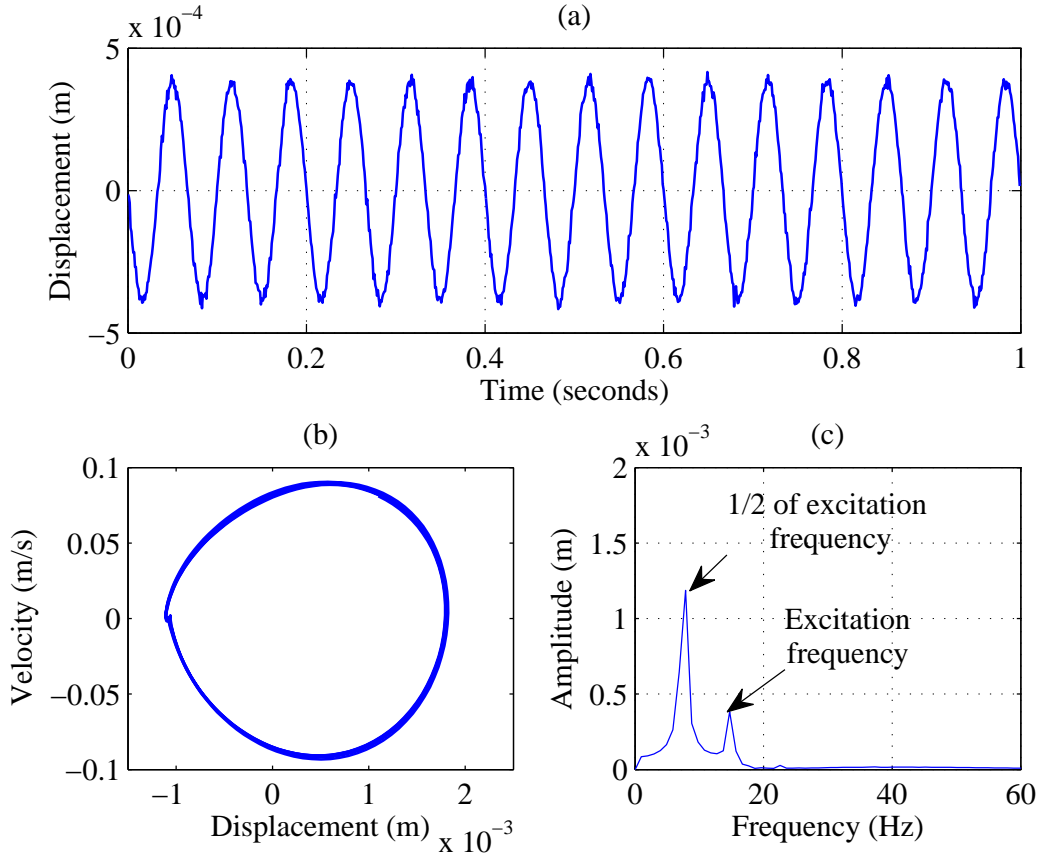


Figure 5.3: (a) Combined harmonic and noise input from the shaker, (b) response phase portrait, and (c) response spectrum. A dominant peak at half the excitation frequency can be seen along with a peak at the excitation frequency.

of known SNR to the base excitation signal.

The prescribed base excitation, the numerically obtained response phase portrait, and the response spectrum are shown in Fig. 5.5, when there is no prescribed noise addition to the harmonic base excitation. The results show that there is no contact between the beam tip and the compliant material. The base excitation, the response phase portrait, and the response spectrum are shown in Fig. 5.6, when

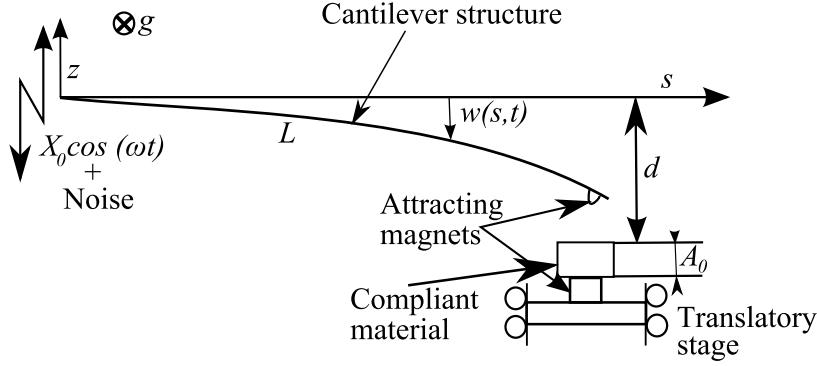


Figure 5.4: The schematic of the elastic structure and the tip sample arrangement.

there is a prescribed noise signal added to the harmonic base excitation. In this case, the signal to noise ratio for the added Gaussian white noise is 402.88, which is the same as that used in the experimental studies. In the case with noise in the input, the response resembles a period-doubled response, which is indicative of a near-grazing contact and provides a confirmation that the tip makes contact with the surface due to the addition of white noise along with the harmonic component in the base excitation.

5.3 Analytical framework for stochastic dynamics

To the best of the author's knowledge, there has not been any prior study aimed at developing an analytical framework for understanding the stochastic dynamics for an impacting system in presence of nonlinear interaction forces. An analytical framework is developed in this section to understand the dynamics of the cantilever-impactor system with an additive Gaussian white noise term to the base excitation. Throughout this work, white noise is treated as the differential of

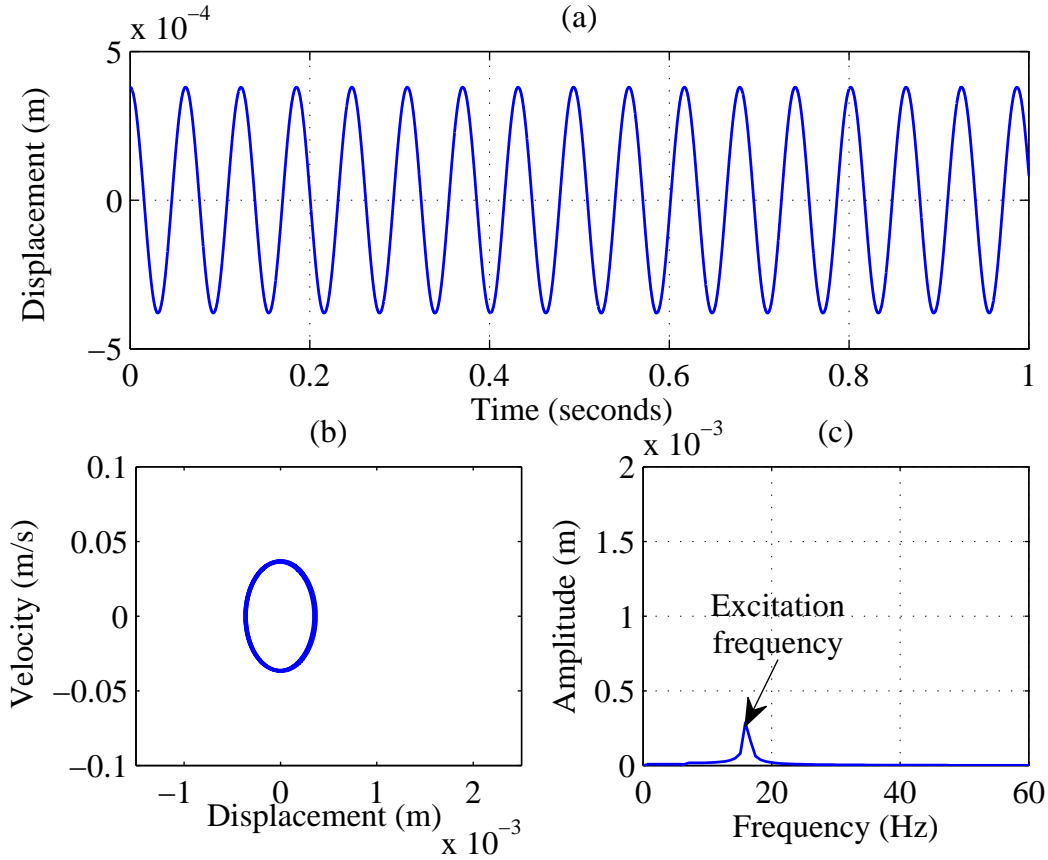


Figure 5.5: (a) Harmonic excitation input from the shaker, (b) response phase portrait of cantilever tip, and (c) response spectrum. A single peak can be seen at the excitation frequency.

a Wiener process (e.g, Gardiner, 1983), which when introduced into the previously deterministic governing equation makes it a stochastic differential equation (SDE). This stochastic differential equation is associated with a unique partial differential equation (called the Fokker-Planck equation) that is satisfied by the probability density function, which governs the system dynamics. The mean values of the dynamical variables may be obtained from this probability density function. The averaged dynamics of the stochastic system may be obtained by solving the moment evolution

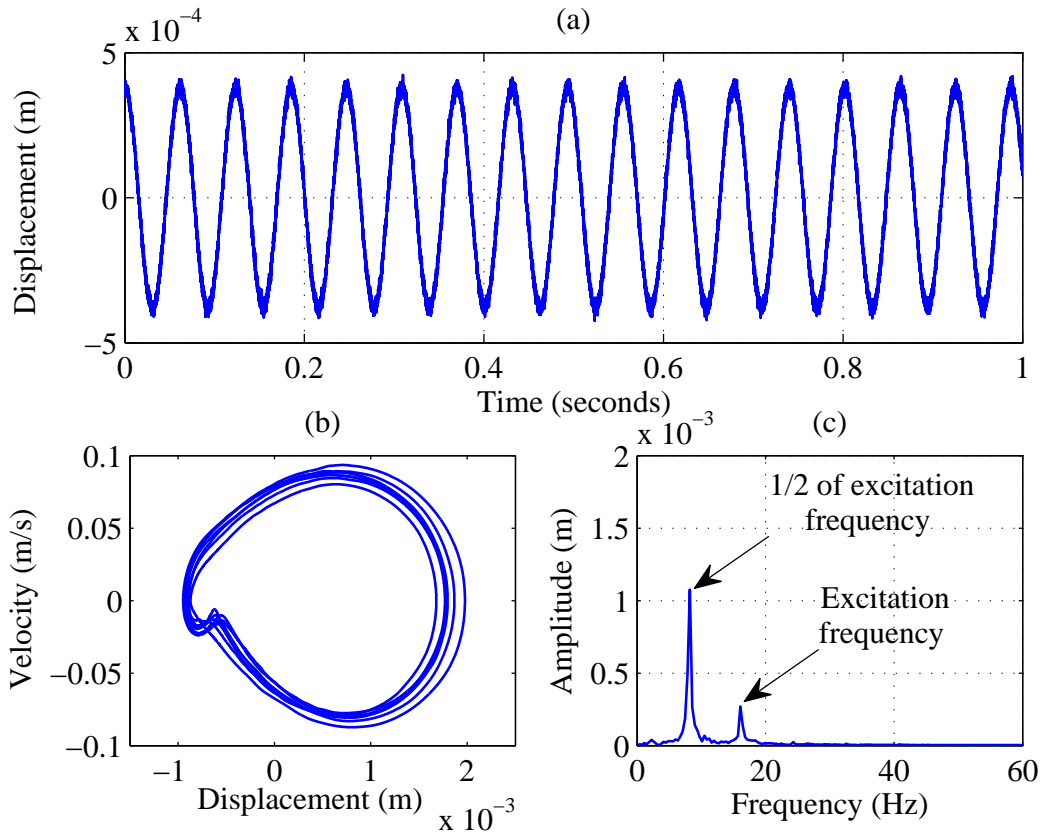


Figure 5.6: (a) Combined harmonic and noise input from the shaker, (b) response phase portrait, and (c) response spectrum. A dominant peak at half the excitation frequency can be seen along with a peak at the excitation frequency.

equations, which can be obtained from the Fokker-Planck equations, after some careful approximations. A moment closure approximation is applied to the system of moment evolution equations to generate a closed system of equations, as discussed next for the considered base excited cantilever with nonlinear tip interaction forces.

5.3.1 Stochastic differential equation

The stochastic differential equation can be obtained by adding a white noise process (the differential of the Wiener process denoted by dW) of strength σ to the governing system of equation given by Eq. (2.8). The resulting differential form in state space is given by

$$\begin{aligned} du_1 &= u_2 dt \\ du_2 &= \left(-\frac{k_1}{m_1} u_1 - \frac{c_1}{m_1} u_2 + \frac{1}{m_1} f_b + \frac{1}{m_1} f_c \right) dt + \sigma dW. \end{aligned} \quad (5.2)$$

5.3.2 Fokker-Planck equation

Eq. (5.2) can be put in the general form

$$dx = Adt + BdW,$$

where A is the drift vector, B is the diffusion matrix, and dW is a vector valued Wiener process. The associated Fokker-Planck Equation reads as

$$\frac{\partial P}{\partial t} = -\sum_{i=1}^N \frac{\partial}{\partial x_i} (A_i P) + \sum_{i,j} \frac{1}{2} \frac{\partial^2}{\partial x_i \partial x_j} \left([BB^T]_{ij} P \right) \quad (5.3)$$

For the particular case of Eq. (5.2), Eq. (5.3) translates to

$$\frac{\partial P}{\partial t} = -\frac{\partial}{\partial u_1} (u_2 P) - \frac{\partial}{\partial u_2} \left(\left(-\frac{k_1}{m_1} u_1 - \frac{c_1}{m_1} u_2 + \frac{1}{m_1} f_b + \frac{1}{m_1} f_{ts} \right) P \right) + \frac{\sigma^2}{2} \frac{\partial^2 P}{\partial u_2^2} \quad (5.4)$$

This equation can be simplified to

$$\frac{\partial P}{\partial t} = -u_2 \frac{\partial P}{\partial u_1} + \frac{c_1}{m_1} P + \frac{\partial P}{\partial u_2} \left(\frac{c_1}{m_1} u_2 + \frac{k_1}{m_1} u_1 - \frac{1}{m_1} f_b - \frac{1}{m_1} f_{ts} \right) + \frac{\sigma^2}{2} \frac{\partial^2 P}{\partial u_2^2} \quad (5.5)$$

5.3.3 Moment evolution equations

The author has strived to solve the moment evolution equations, given the intractability of explicitly solving the Fokker-Planck equation. To this end, the n^{th} order moment of an arbitrary random variable s with probability density function $P(x, y)$ is constructed as

$$\langle s^n \rangle = \int \int s^n P(x, y) dx dy. \quad (5.6)$$

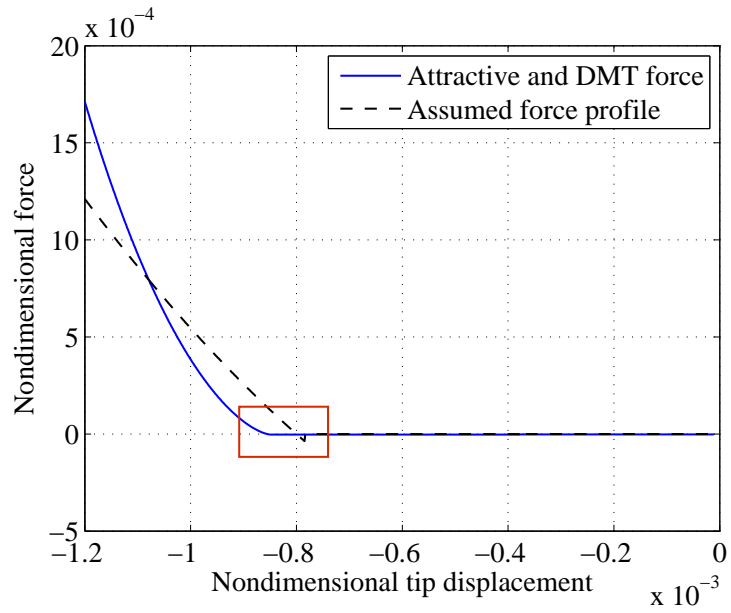
Instead of using the combination of magnetic attraction and DMT forces (as done in the numerical simulations), the author uses a different force profile to derive the moment equations, as the prior force combination results in the appearance of a negative moment. The tip-sample force combination described in Eq. 2.2 contains an attractive part and a repulsive part. The attractive part (van der Waals force) of the force combination gives rise to the negative moment. In addition to the negative moment generated due to the attractive part, the fractional power in the repulsive part of the interaction force would generate fractional powers in the moment evolution equations which is unwarranted in this analysis. To address these issues, the author uses a new force profile. This new force profile is given by

$$f_{ts} = \phi_1 \bar{\beta} (-a + u_1^2) h(\bar{a} - u_1). \quad (5.7)$$

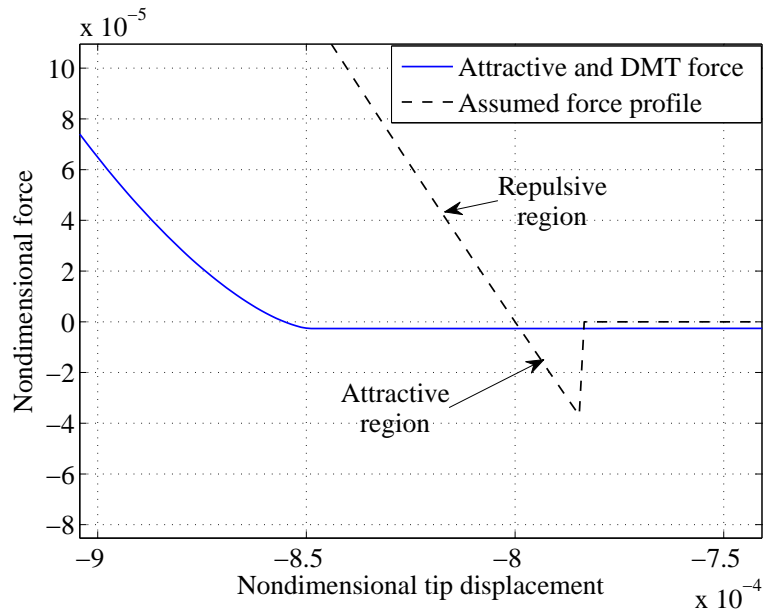
In Eq. (5.7), h represents the Heaviside function, and the constant \bar{a} is given by:

$$\bar{a} = \frac{-1}{\phi_1} (\nu \cos \Omega \tau + \eta).$$

The use of Heaviside function accounts for the discontinuous nature of the contact forces experienced by the cantilever tip. Since the assumed force profile is quadratic,



(a)



(b)

Figure 5.7: (a) Comparison between the combination of the magnetic attractive and DMT forces, and the assumed force profile. (b) Expanded view of the comparison for the boxed portion in Fig. 5.7(a).

both the repulsive and the attractive regime of tip-sample forces can be successfully modeled by Eq. (5.7). The constants $\bar{\beta}$ and a are tuned to get as close to the original force profile as that used in the numerical studies. The selected values of the different parameters are

$$\bar{\beta} = 400$$

$$a = 6.67 \times 10^{-6}.$$

The assumed force profile given by Eq. (5.7) and the combination of magnetic attraction and DMT contact forces (given by Eq. (2.1)) are compared in Fig. 5.7.

The moment evolution equations are obtained by multiplying both sides of Eq. (5.5) by $u_1^m u_2^n$ and then integrating both sides of the equation over the considered domain (the details are provided in Appendix A). The resulting system has the form

$$\begin{aligned} \frac{d \langle u_1^m u_2^n \rangle}{dt} = & m \langle u_1^{m-1} u_2^{n+1} \rangle - n \frac{c_1}{m_1} \langle u_1^m u_2^n \rangle \\ & - n \frac{k_1}{m_1} \langle u_1^{m+1} u_2^{n-1} \rangle + n \frac{f_b}{m_1} \langle u_1^m u_2^{n-1} \rangle \\ & + \frac{\phi_1 \bar{\beta}}{m_1} h(\bar{a} - \langle u_1 \rangle) \left[-an \langle u_1^m u_2^{n-1} \rangle \right] \\ & + \frac{\phi_1 \bar{\beta}}{m_1} h(\bar{a} - \langle u_1 \rangle) \left[n \langle u_1^{m+2} u_2^{n-1} \rangle \right] \\ & + \frac{\sigma^2}{2} n(n-1) \langle u_1^m u_2^{n-2} \rangle. \end{aligned} \quad (5.8)$$

For the moment evolution equations given by Eq. (5.8), since the moments of order n and m involve moments of order $n+1$ and $m+1$, the hierarchy of moments grows indefinitely. To address this, truncation of higher order moments after some order is required, to make the moment equations amenable to a numerical solution. In Fig. 5.8, the evolutions of the first moment are compared when moments are retained

upto orders 2 and 3. It is observed that the evolution of mean displacement with respect time is almost the same when moments of orders higher than 3 or 4 are truncated. Here, the moments of order 4 and higher are neglected, which gives a set of 9 coupled ordinary differential equations. The associated variables used in the moment equations are as follows:

$$x_1 = \langle u_1 \rangle$$

$$x_2 = \langle u_2 \rangle$$

$$x_3 = \langle u_1^2 \rangle$$

$$x_4 = \langle u_1 u_2 \rangle$$

$$x_5 = \langle u_2^2 \rangle$$

$$x_6 = \langle u_1^3 \rangle$$

$$x_7 = \langle u_1^2 u_2 \rangle$$

$$x_8 = \langle u_1 u_2^2 \rangle$$

$$x_9 = \langle u_2^3 \rangle.$$

The system of the moment evolution equations read as

$$\dot{x}_1 = x_2 \tag{5.9}$$

$$\dot{x}_2 = -Cx_2 - Kx_1 + F_b + H(-a + x_3) \tag{5.10}$$

$$\dot{x}_3 = 2x_4 \tag{5.11}$$

$$\dot{x}_4 = x_5 - Cx_4 - Kx_3 + F_b x_1 + H(-ax_1 + x_6) \tag{5.12}$$

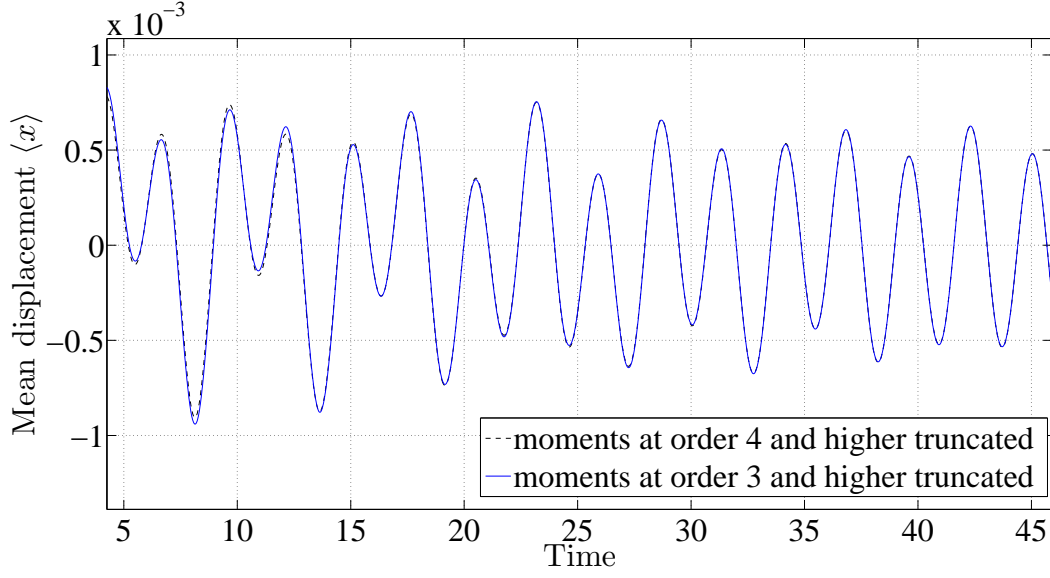


Figure 5.8: Comparisons of the evolutions of the mean displacement for different moment equation truncations.

$$\dot{x}_5 = -2Cx_5 - 2Kx_4 + 2F_b x_2 + 2H(-ax_2 + x_7) + \sigma^2 \quad (5.13)$$

$$\dot{x}_6 = 3x_7 \quad (5.14)$$

$$\dot{x}_7 = 2x_8 - Cx_7 - Kx_6 + F_b x_3 + H(-ax_3) \quad (5.15)$$

$$\dot{x}_8 = x_9 - 2Cx_8 - 2Kx_7 + 2F_b x_4 + 2H(-ax_4) + \sigma^2 x_1 \quad (5.16)$$

$$\dot{x}_9 = -3Cx_9 - 3Kx_8 + 3F_b x_5 + 3H(-ax_5) + 3\sigma^2 x_2. \quad (5.17)$$

In Eqs. (5.9) to (5.17), the different coefficients correspond to

$$C = \frac{c_1}{m_1}$$

$$K = \frac{k_1}{m_1}$$

$$F_b = \frac{f_b}{m_1}$$

$$H = \frac{\phi_1 \bar{\beta}}{m_1} h (\bar{a} - x_1).$$

5.4 Numerical studies with the moment evolution equations

The parameter values for the numerical simulations of the moment evolution equations are identical to those used in Section 5.2. For the case where the noise strength $\sigma = 0$, the mean value of displacement (which is characterized by the first moment) is plotted in Fig. 5.9. It is observed in Fig. 5.9 that the mean value of the displacement does not cross the surface boundary, denoted by the red line. This observation corresponds to previous numerical and experimental observations,

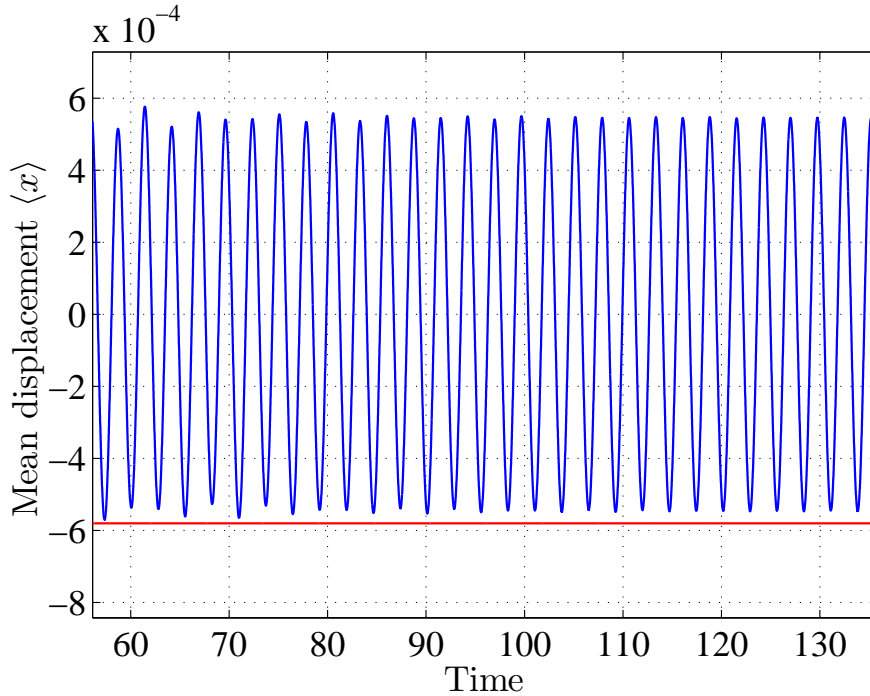


Figure 5.9: Evolution of mean value of displacement with time when $\sigma=0$. The solid line at the bottom signifies the location of the compliant material surface.

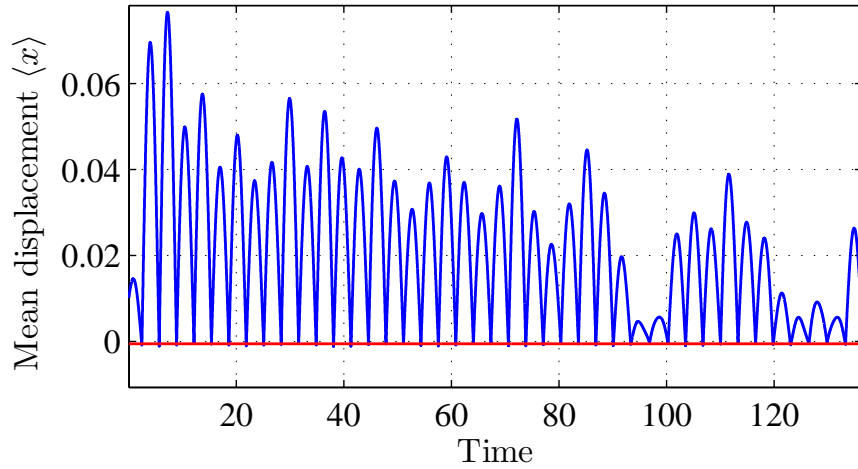


Figure 5.10: Evolution of mean value of displacement with time when $\sigma=0.0004$. The solid line at the bottom signifies the location of the compliant material surface.

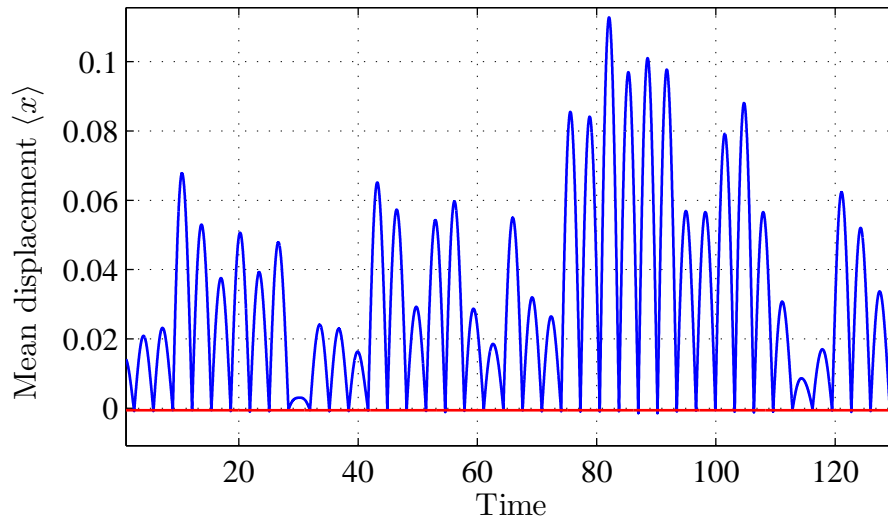


Figure 5.11: Evolution of mean value of displacement with time when $\sigma=0.0010$. The solid line at the bottom signifies the location of the compliant material surface.

wherein it was noted that the tip does not make contact with the sample surface when there was no prescribed additive noise. For the case where the noise strength

$\sigma = 0.0004$, the mean tip displacement is plotted in Fig. 5.10. In this case, it is observed that the displacement magnitude is much higher than that seen in Fig. 5.9. Furthermore, the evolution of the mean value of the displacement suggests that contact between the tip and the sample is facilitated by the introduction of noise. In Fig. 5.11, the evolution of mean of displacement is plotted for a higher noise strength; that is, $\sigma = 0.001$. A comparison of Fig. 5.10 and Fig. 5.11 clearly indicates that the magnitude of the displacement value becomes higher when the noise strength is higher. The probability distribution has been modeled by a sharp Gaussian distribution with a mean value of 0.01 and a variance of 0.0625. The numerical evolution of moments show qualitatively the same behavior as that noted previously through the authors' experimental and direct numerical studies; the addition of noise facilitates contact in the response, when there was previously no contact without noise. The threshold amount of noise necessary to induce contact is expressed in terms of signal to noise ratio for the experimental and numerical studies and noise intensity for the analytical-numerical studies conducted with moment evolution equations.

5.5 Application to atomic force microscopy

In this section, the effects of noise on an AFM cantilever is studied through numerical efforts. Effects of adding noise to the harmonic signal in an AFM has the similar effects as in the macro-scale system. The potential function for the vibrating AFM cantilever is obtained by integrating the right hand side of Eq. (2.1)

with respect to the tip displacement and adding the potential associated with the elastic stiffness of the cantilever to it. The variation of the potential function with respect to the cantilever's tip displacement is shown in Fig. 5.12. In this figure, the potential function is plotted for three different values of cantilever tip radius R , namely, 20 nm, 60 nm, and 100 nm. It is observed that depth of the second potential well, which is created by the tip-sample interactions, increases with increase of the tip-radius R . The presence of a double-well potential in the oscillating system makes it amenable to stochastic phenomena, since the addition of noise can move the system from one potential well to the other. The constants chosen to plot the potential wells in Fig. 5.12 are given in Table 2.1.

The micro-scale AFM cantilever in tapping mode is modeled in the same fash-

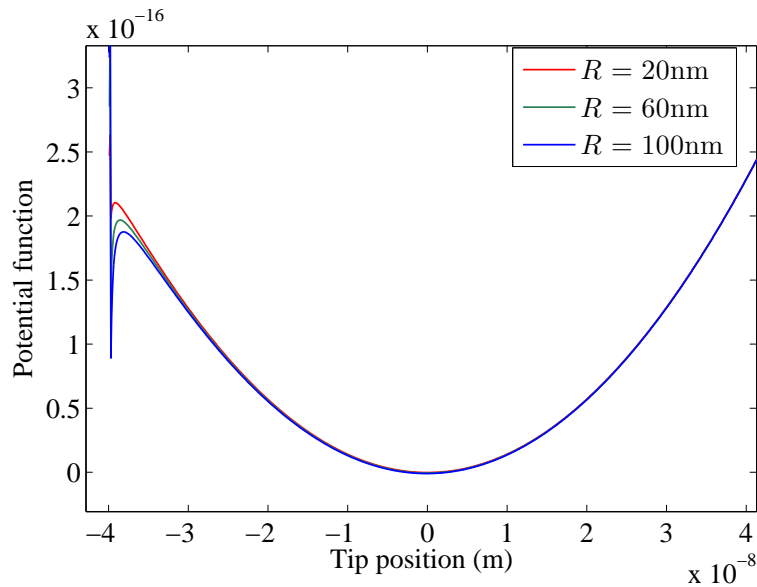


Figure 5.12: Variation of the potential function for the considered the tip-sample combination with the radius of the tip R .

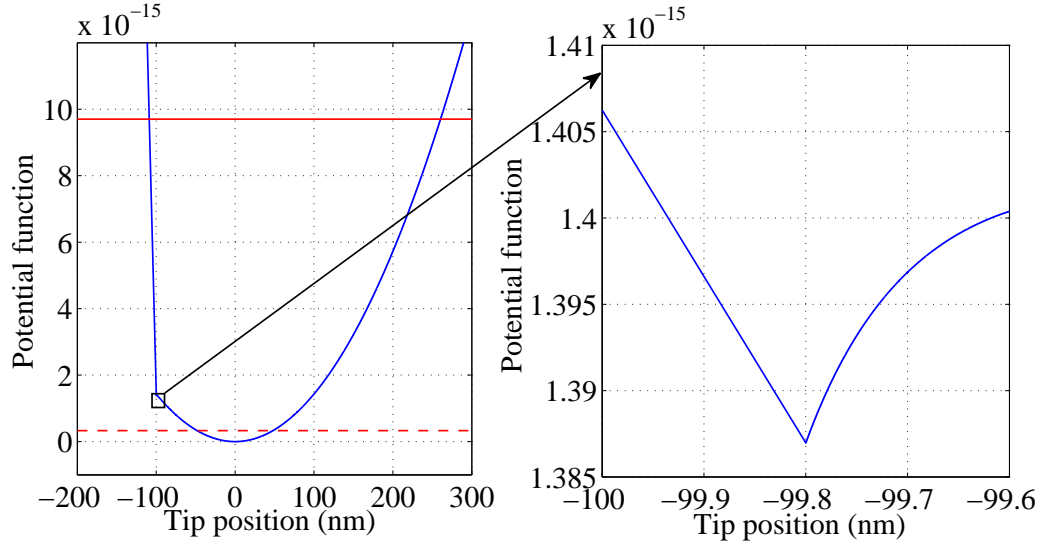


Figure 5.13: Potential function for AFM cantilever. A magnified view of the second potential well is shown on the right.

ion as the macro-scale cantilever studied in the previous sections. However, in the governing equation for the macro-scale forces, the forces are replaced by the non-dimensional form of the micro-scale tip-sample forces given by Eq. (2.1). Unlike the macro-scale analysis, the tip-mass of the cantilever is ignored in the micro-scale case. Except for these changes, the micro-scale system is modeled in the same fashion as the macro-scale system, in the presence of an additive Gaussian white noise in the base input.

Numerical simulations are carried out for a Si cantilever and HOPG sample combination, with the corresponding parameters are listed in Table 2.1. The first natural frequency of the selected cantilever is around 14 kHz. The selected forcing frequency is around 37 kHz, which is 2.24 times the first natural frequency. The excitation amplitude and initial tip sample distance are selected as 56 nm and 100

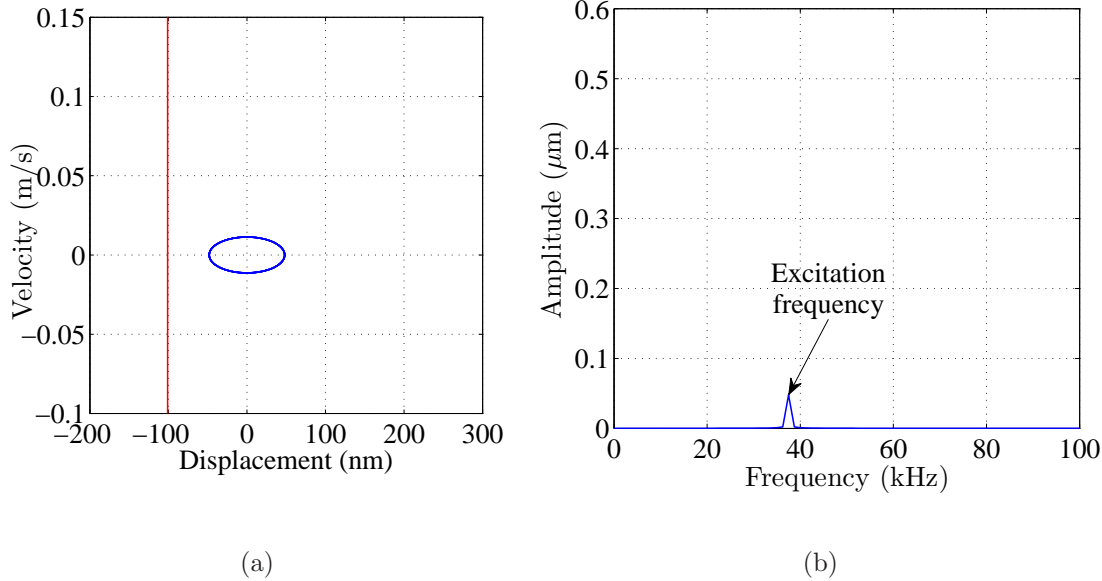


Figure 5.14: (a) Phase portrait of the cantilever tip response when there is no noise addition in the base input. (b) The response spectrum. The vertical line at 100 nm corresponds to the location of the sample in the phase portrait. A dominant peak at the excitation frequency can be seen in the response spectrum.

nm, respectively. The potential function for this situation is plotted in Fig. 5.13. For the case without noise, the response phase portrait and spectrum are shown in Fig. 5.14. The associated harmonic oscillation corresponds to the dotted line in the potential function plot shown in Fig. 5.13. The motions are symmetric in the phase portrait and they occur around the lower potential well. Furthermore, it is observed that the response is at the same frequency as the excitation, and that the cantilever tip does not make contact with the sample. Next, Gaussian white noise is added to the harmonic input signal. For a case with noise and a signal to noise ratio of 100, the response phase portrait and spectrum are presented in Fig. 5.15. The associated oscillation corresponds to the solid line in the potential function shown in Fig. 5.13.

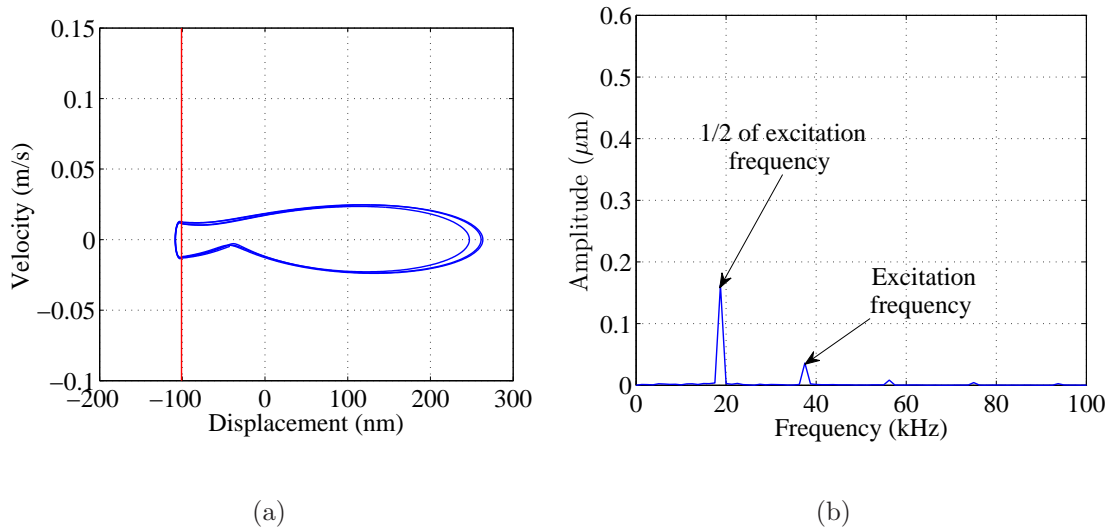


Figure 5.15: (a) Phase portrait of the cantilever tip response when there is noise added to the base input. The signal to noise ratio is 100. (b) The response spectrum. The vertical line at 100 nm corresponds to the location of the sample. A dominant peak at one half of the excitation frequency can be seen in the response spectrum.

It is noted that the inclusion of noise in the base excitation pushes the solution to a higher energy level where the motions encounter a double well potential. It is observed that the cantilever tip makes contact with the sample, due to the addition of white noise in the base excitation, with all other conditions remaining the same as in the previous case without noise and no contact. The response spectrum of the cantilever tip motion is seen to be dominated by a frequency peak at one half of the excitation frequency. The contact induced by addition of white noise in the excitation signal and the corresponding period-doubled response is seen to be realizable in the micro-scale AFM as previously seen in the macro-scale system.

5.6 Analysis with moment equations

The averaged dynamics of the stochastic system may be determined by solving the moment evolution equations, which can be obtained from the Fokker-Planck equations, after some assumptions, as seen in the earlier section.

As in earlier analysis, instead of using a combination of attraction and DMT forces (as done in the numerical simulations), the author uses a separate assumed force profile to derive the moment equations, to avoid a negative moment. This assumed force profile is given by

$$f_c = \phi_1 \left(-a + bu_1^2 \right) h(\bar{a} - u_1). \quad (5.18)$$

In Eq. (5.18), h represents the Heaviside function, and the constant \bar{a} is given by

$$\bar{a} = \frac{-1}{\phi_1} (\nu \cos \Omega\tau + \eta - \xi_0).$$

The use of Heaviside function accounts for the discontinuous nature of the contact forces experienced by the cantilever tip. The parameter \bar{a} is chosen such that the repulsive forces come into play when the cantilever tip makes contact with the sample. Since the assumed force profile is quadratic, both the repulsive and the attractive regime of tip-sample forces can be successfully modeled by using Eq. (5.18). The constants a and b are tuned to get close to the original force profile used for the numerical studies near contact. The selected values of the constants are

$$a = 400 \times 10^{-6}$$

and

$$b = 100.$$

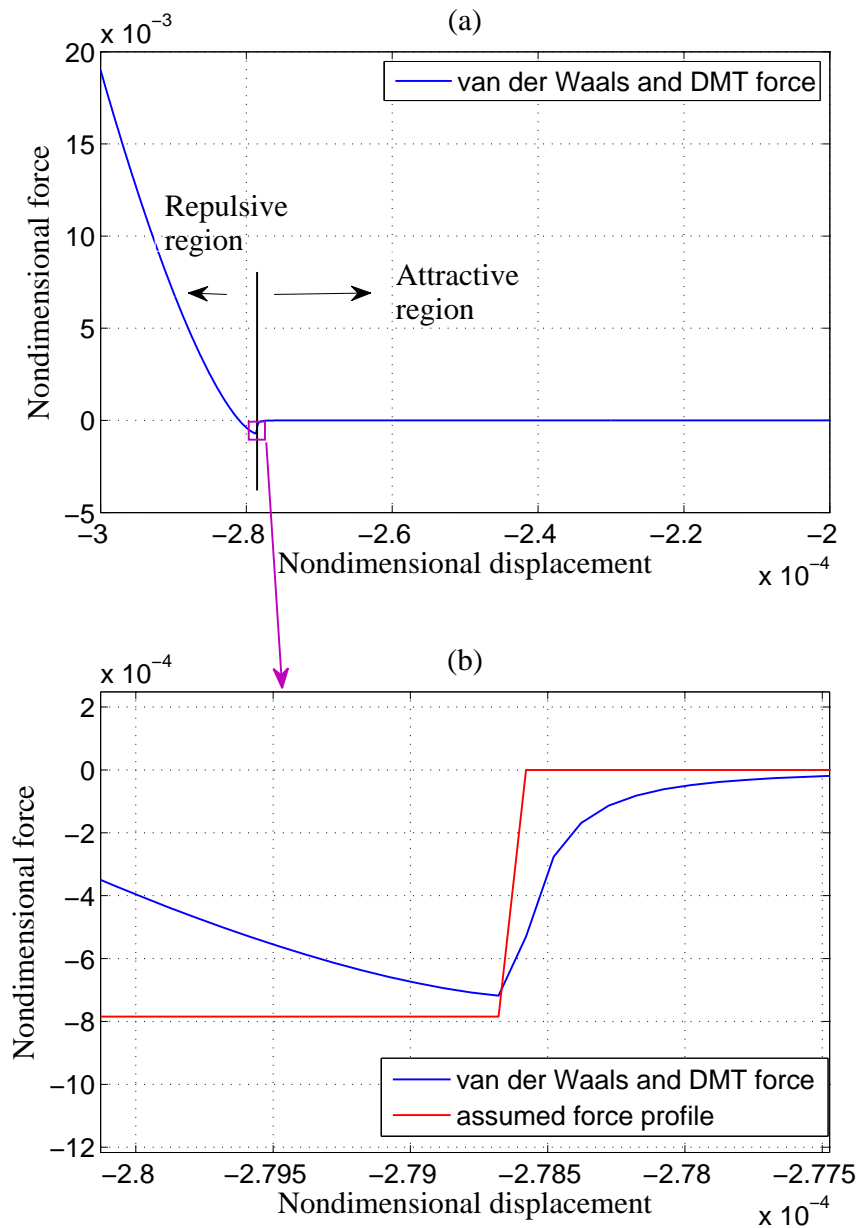


Figure 5.16: (a) Attractive and repulsive force interaction in the van der Waals and DMT force combination. (b) Comparison of the assumed force profile with tip-sample force given in (a) near the contact point.

The assumed force profile given by Eq. (5.18) and the combination of attractive and DMT contact forces given by Eq. (2.3) are compared in Fig. 5.16. The author has selected the parameters in a manner to match the force profiles near contact, since the focus of this analysis is to determine whether contact is achievable through the introduction of noise in the framework. The moment evolution equations are obtained by multiplying both sides of Eq. (5.5) by $u_1^m u_2^n$ and then integrating both sides of the equation over the domain. The obtained moment equations are given by

$$\begin{aligned}
\frac{d \langle u_1^m u_2^n \rangle}{dt} = & m \langle u_1^{m-1} u_2^{n+1} \rangle - n \frac{c_1}{m_1} \langle u_1^m u_2^n \rangle \\
& - n \frac{k_1}{m_1} \langle u_1^{m+1} u_2^{n-1} \rangle + n \frac{f_b}{m_1} \langle u_1^m u_2^{n-1} \rangle \\
& + \frac{\phi_1}{m_1} h (\bar{a} - \langle u_1 \rangle) [-an \langle u_1^m u_2^{n-1} \rangle] \\
& + \frac{\phi_1}{m_1} h (\bar{a} - \langle u_1 \rangle) [bn \langle u_1^{m+2} u_2^{n-1} \rangle] \\
& + \frac{\sigma^2}{2} n (n-1) \langle u_1^m u_2^{n-2} \rangle.
\end{aligned} \tag{5.19}$$

In the moment evolution equations given by Eq. (5.19), since the moments of order n and m involve moments of order $n+1$ and $m+1$, the moment hierarchy grows indefinitely. At this point, truncation of higher order moments after some order is required, to make the moment equations amenable to a numerical solution. In Fig. 5.17, the evolutions of the first moment are compared when moments are retained upto orders 3 and 4. As in the macro-scale case, moments of order 4 and higher are neglected, which results in a set of 9 coupled ODEs. The variables used in the moment equations as are given in the previous sections.

The system of coupled ordinary differential equations read as

$$\dot{x}_1 = x_2 \quad (5.20)$$

$$\dot{x}_2 = -Cx_2 - Kx_1 + F_b + H(-a + bx_3) \quad (5.21)$$

$$\dot{x}_3 = 2x_4 \quad (5.22)$$

$$\dot{x}_4 = x_5 - Cx_4 - Kx_3 + F_b x_1 + H(-ax_1 + bx_6) \quad (5.23)$$

$$\dot{x}_5 = -2Cx_5 - 2Kx_4 + 2F_b x_2 + 2H(-ax_2 + bx_7) + \sigma^2 \quad (5.24)$$

$$\dot{x}_6 = 3x_7 \quad (5.25)$$

$$\dot{x}_7 = 2x_8 - Cx_7 - Kx_6 + F_b x_3 + H(-ax_3) \quad (5.26)$$

$$\dot{x}_8 = x_9 - 2Cx_8 - 2Kx_7 + 2F_b x_4 + 2H(-ax_4) + \sigma^2 x_1 \quad (5.27)$$

$$\dot{x}_9 = -3Cx_9 - 3Kx_8 + 3F_b x_5 \quad (5.28)$$

$$+ 3H(-ax_5) + 3\sigma^2 x_2. \quad (5.29)$$

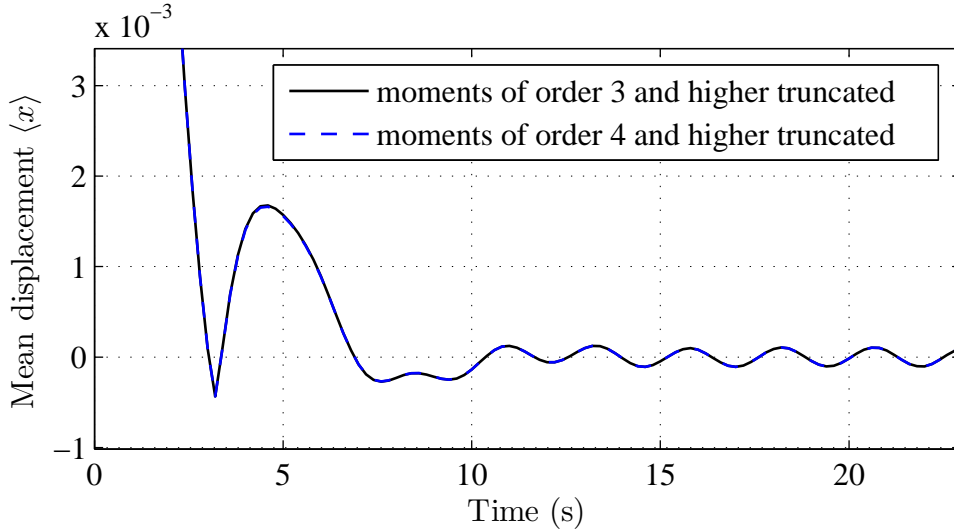


Figure 5.17: Comparisons of the evolutions of the mean displacement for different truncations of moment evolution equations.

In equations (5.20) to (5.29), the different coefficients take the form

$$C = \frac{c_1}{m_1}$$

$$K = \frac{k_1}{m_1}$$

$$F_b = \frac{f_b}{m_1}$$

$$H = \frac{\phi_1}{m_1} h (\bar{a} - x_1).$$

5.7 Numerical solutions of the moment evolution equations

The parameter values for the numerical simulations of the moment evolution equations are identical to those listed in Table 2.1. The mean value of displacement, which is characterized by the first moment, is plotted in Fig. 5.18, when the noise

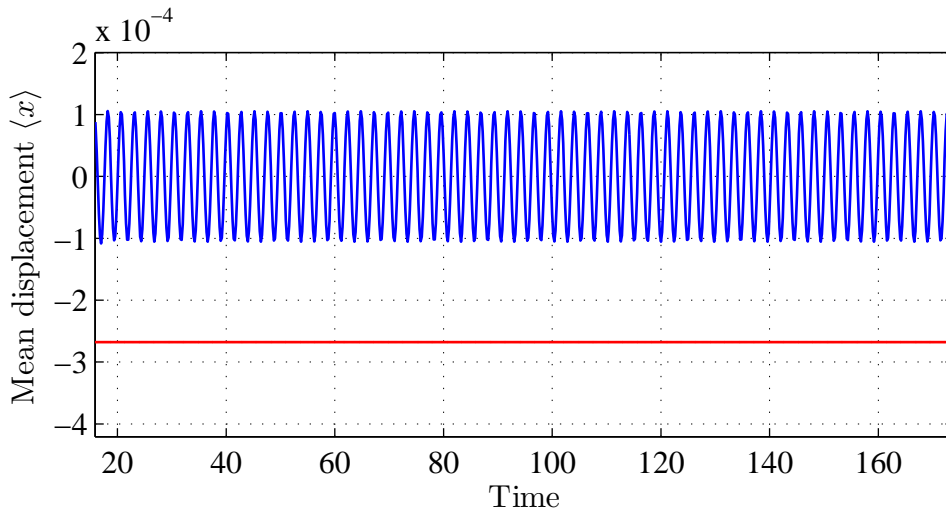


Figure 5.18: Time evolution of the first moment (mean displacement) for $\sigma = 0$.

The solid line at the bottom represents the sample location.

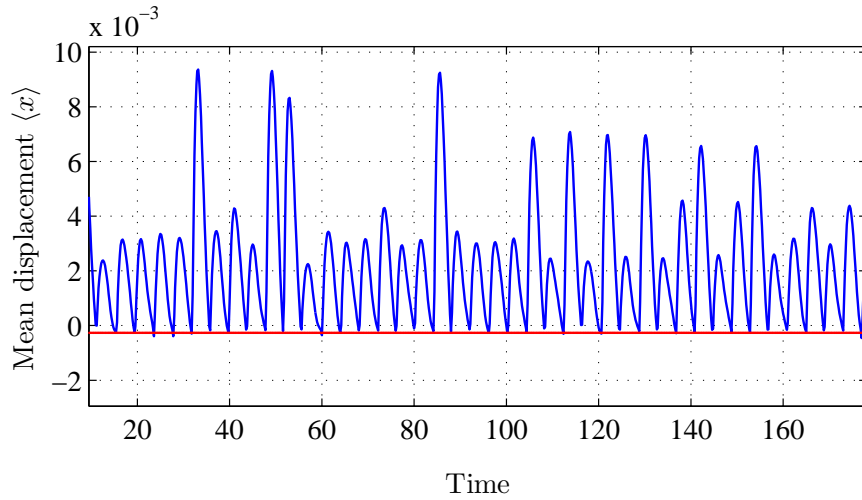


Figure 5.19: Time evolution of the first moment (mean displacement) for $\sigma = 0.03$. The solid line at the bottom represents the sample location.

strength $\sigma = 0$. It is observed that the mean value of the displacement does not cross the surface boundary, denoted by the solid line. This observation is consistent

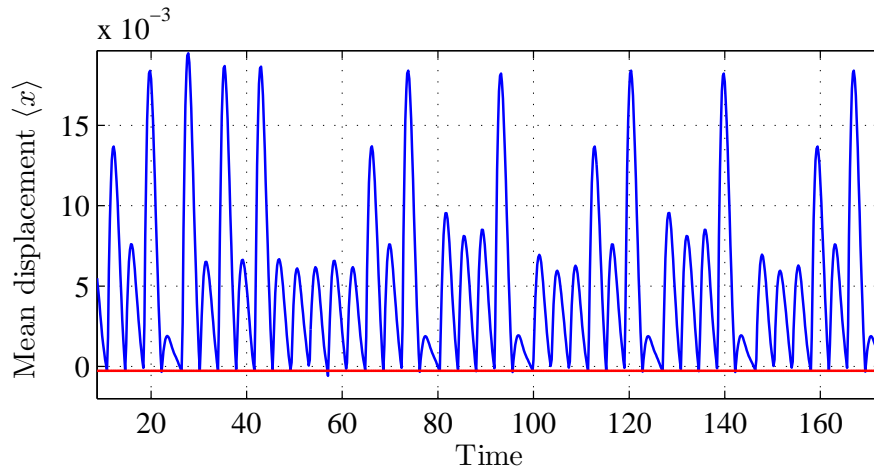


Figure 5.20: Time evolution of the first moment (mean displacement) for $\sigma = 0.04$. The solid line at the bottom represents the sample location.

with the previous numerical observation, wherein the tip does not make contact with the sample surface when there was no noise addition. The mean tip displacement is plotted in Fig. 5.19, when the strength of the noise $\sigma = 0.03$. In this case, it is observed that the displacement magnitude is much higher than that seen in Fig. 5.18 and the evolution of the mean value of the displacement suggests that contact between the tip and the sample takes place due to the introduction of noise. The evolution of mean of displacement is plotted in Fig. 5.20, when the strength of introduced noise $\sigma = 0.04$ is higher than the noise strength in the previous case. From a comparison of results shown in Fig. 5.19 and Fig. 5.20, it is clear that the magnitude of the displacement value becomes higher with increase in the noise strength. For these simulations, the probability distribution has been modeled as a sharp Gaussian distribution with the mean of 0.01 and variance of 0.0625. The numerical evolution of moments show qualitatively the same behavior as that seen in the direct numerical simulations. It is noted that the noise addition to the deterministic input facilitates contact, when previously there was no contact.

5.8 Summary

In this chapter, the effects of additive noise in a macro-scale system involving a base-excited cantilever with nonlinear tip interaction forces and a micro-scale system used in tapping mode atomic force microscopy is described. It is observed experimentally that the introduction of noise in the base excitation promotes contact between the tip and the surface, when there was previously no contact in the absence

of noise. The addition of a threshold amount of noise moves the response to a higher energy level. It is observed that qualitative changes take place due to the addition of noise. Numerical studies are conducted by using a reduced-order model with long-range attractive forces and DMT contact forces at the cantilever's tip, wherein the base excitation is passed through an additive Gaussian white noise channel. An analytical framework is developed to study the stochastic system dynamics by deriving the Fokker-Planck equation for the system. The stochastic quantities are studied by solving the moment evolution equations obtained from the Fokker-Planck equation. The evolution of the mean value of displacement shows that contact between the tip and the sample can be facilitated by adding noise to the system input. The findings obtained in studies with the macro-scale system are applied to a micro-scale system encountered in dynamic atomic force microscopy. It is observed through the numerical studies that the results obtained in the macro-scale studies are scalable to the micro-scale system; that is, the addition of noise in the input facilitates contact between the tip and the sample in the considered micro-scale application, as observed in the experimental and numerical studies of the macro-scale system.

Chapter 6

Effects of Noise on Sticking Motions

In this chapter, the effects of added noise on the macro-scale cantilever are studied, wherein the cantilever tip sticks with the base magnet due to high attractive forces. The work presented in this chapter follows the published work by Chakraborty and Balachandran (2011d). The experimental arrangement described here is slightly modified than that used in the previous set up. A different (stiffer) cantilever is used, and the magnetic interaction forces are also modified to have a higher attractive force at the tip. In this study, all the investigations are carried out for excitation frequencies around the first natural frequency of the system.

As in the previous studies, the experimental arrangement consists of a base-excited elastic cantilever beam with long-range attractive forces from attractive magnets and short-range repulsive forces from contact interactions. The strength of the attractive forces is higher than that used in the previous experiments described in Chapter 2; the strength of the magnetic force is increased by changing the magnets. The repulsive contact forces arise due to intermittent contact between the tip magnet and a thin layer of compliant material that covers the base magnet. The potential function of this cantilever-sample combination has a double well characteristic. It is observed that the tip sticks to the base magnet, when the excitation is purely harmonic. In this case, the response of the cantilever is trapped in one potential

well due to a high attractive force. Next, Gaussian white noise is added to the deterministic harmonic base excitation. The cantilever tip is seen to escape from the situation of sticking and it makes intermittent contact with the base magnet when the signal to noise ratio (SNR) of the input crosses a “threshold” level. In this case, the motion escapes from being trapped in one potential well and the cantilever tip periodically interacts with both of the potential wells. This phenomenon is studied by using a reduced-order numerical model constructed with a single-mode approximation. As in previous studies, the moment-evolution equations are obtained and studied. The numerical results obtained from these equations show qualitative agreement with the experimental and numerical observations.

In the next section, the experimental arrangement and results are provided. The numerical efforts are presented in the subsequent section. Studies conducted with the Fokker-Planck equations and the moment-evolution equations are presented in the following section.

6.1 Experimental studies

The experimental arrangement, which is shown in Fig. 6.1, follows that used in previous studies. It involves a base-excited steel cantilever with nonlinear interaction forces acting at its tip. The base magnet is covered by a thin compliant material, which imparts a repulsive contact force to the tip whenever it makes contact with this material. The displacement of the cantilever tip is recorded by an optical displacement sensor. The length of the beam is 0.227 m and the cross-section area

is $1.67 \text{ mm} \times 24 \text{ mm}$. The Young's modulus of the beam material is 207 GPa, and the material density is 8000 Kg/m^3 . The first natural frequency of the structure is experimentally determined as 26 Hz. The mass of the magnet attached to the beam tip is 0.15 grams. The experimental arrangement is oriented in a horizontal plane, so that gravity effects on the bending vibrations of the cantilever structure can be neglected.

The experimental studies are conducted with the excitation frequency at or close to the first natural frequency of the system. The author begins the experiment with a purely harmonic base excitation, as shown in Fig. 6.2(a). The beam tip is seen to stick with the base magnet due to the high attractive force, and no

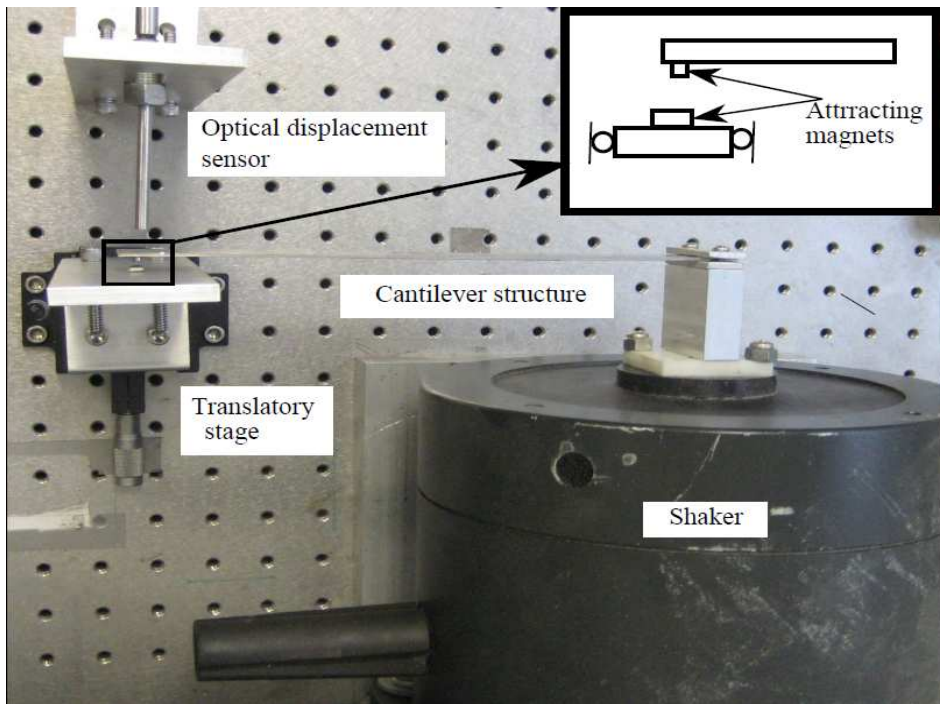
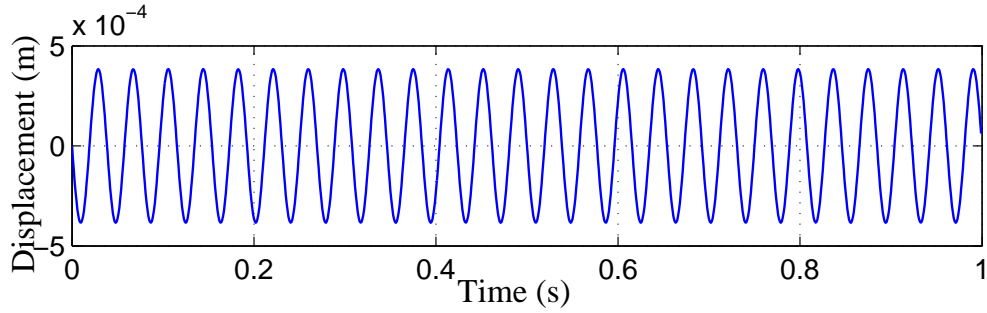
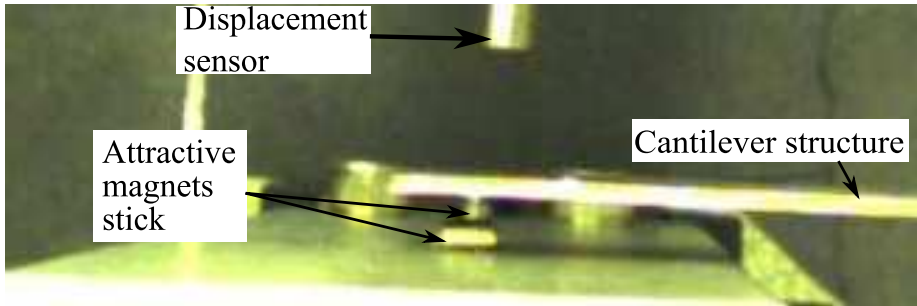


Figure 6.1: Experimental arrangement. Details of the tip arrangement are shown in the inset.



(a)



(b)

Figure 6.2: (a) Purely harmonic input excitation from the shaker. (b) Snapshot of the experimental system depicting the tip magnet sticking with the base magnet.

oscillations are recorded. A snapshot of this scenario is shown in Fig. 6.2(b); the tip magnet of the structure sticks with the base magnet when the base excitation is purely harmonic. The base excitation is seen to be not sufficient to overcome the attractive force at the cantilever tip.

Gaussian noise is added to the base excitation along with the harmonic input. In order to quantify the noise level in the input, the author expresses the noise level in terms of the signal to noise ratio (SNR), as in earlier studies. It is observed that when the SNR of the excitation reaches a threshold level (SNR is calculated to be 50.6 in this case), the tip does not stick with the base magnet, and the cantilever

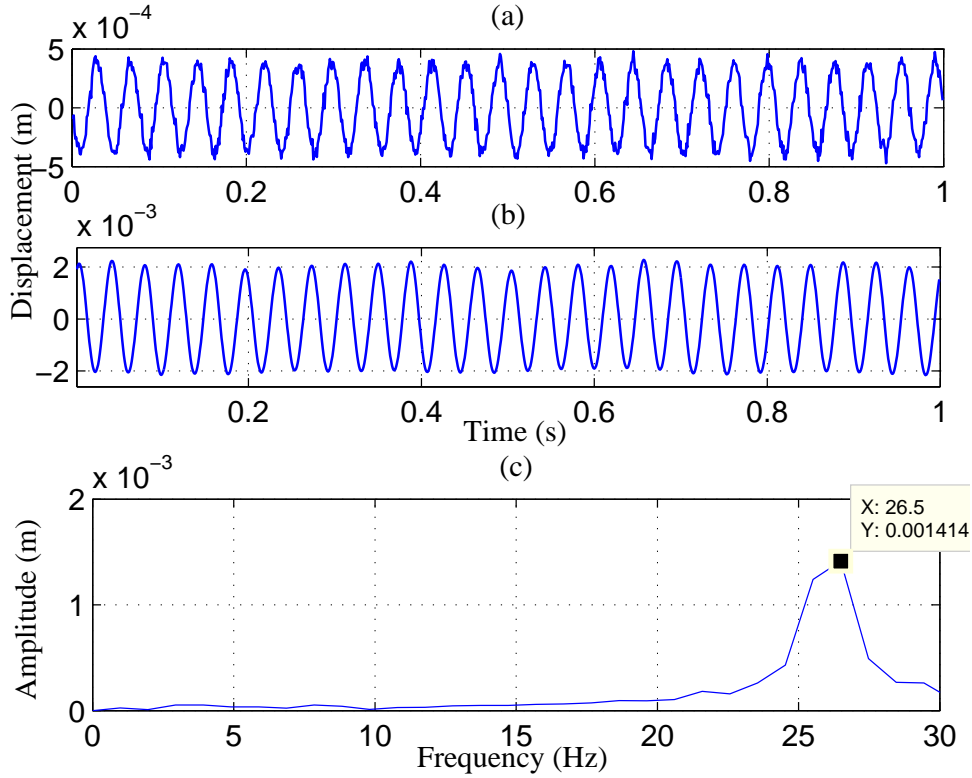


Figure 6.3: (a) Representative combination of white noise and harmonic component used for base excitation in the experiments. SNR for this input is 50.64. (b) Cantilever tip displacement showing intermittent contact between the tip and the base magnet. (c) Response spectrum of the displacement data showing a peak at the excitation frequency.

undergoes harmonic oscillations with intermittent contact.

The experimentally obtained data with the noise addition to the input is presented in Fig. 6.3. The input signal, which is the superposition of the harmonic component and the random component, is shown in Fig. 6.3(a). The cantilever tip displacement and the spectrum of the cantilever tip response are presented in Fig. 6.3(b) and Fig. 6.3(c), respectively. It is seen that the cantilever response has a

dominant component at the frequency of excitation, which in this case, is at the first natural frequency of the system. The addition of noise to the harmonic component in the excitation releases the tip from sticking with the base magnet and the tip makes intermittent contact with the base, instead of sticking with the base magnet as seen previously in Fig. 6.2(b).

6.2 Numerical studies

The response of the impacting cantilever is studied by using a reduced-order model developed through a Galerkin projection of the governing equations of motion, following the studies described in previous chapters.

The contact force along with the magnetic attractive force is given by

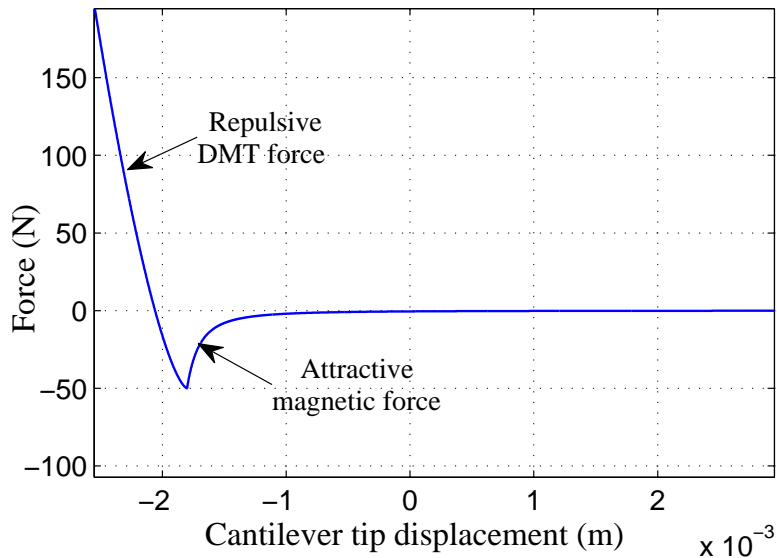


Figure 6.4: Variation of nonlinear tip interaction forces with the cantilever tip displacement.

$$f_{ts}(\bar{z}) = \begin{cases} -\frac{\lambda}{(\bar{z}+\eta)^2} & \text{for } \eta + \bar{z} > \xi \\ -\frac{\lambda}{(\xi)^2} + \kappa(\xi - \eta - \bar{z})^{1.5} & \text{for } \eta + \bar{z} \leq \xi \end{cases} \quad (6.1)$$

Here, \bar{z} is the nondimensional absolute displacement of the cantilever's tip. The other nondimensional quantities are given by

$$\xi = \frac{A_0}{L}, \quad \kappa = \frac{K_E}{\rho A \sqrt{L} \omega_n^2}, \quad \lambda = \frac{K_M}{\rho A L^4 \omega_n^2}, \quad \eta = \frac{d}{L}.$$

Here, A_0 is the compliant material thickness, d is the initial distance between the cantilever tip and the sample, and K_M and K_E are constants related to the attractive and repulsive forces, respectively. The tip-sample forces are modeled by using attractive magnetic forces and DMT contact forces. The forces are plotted in the dimensional form in Fig. 6.4. The potential function arising due to this force in-

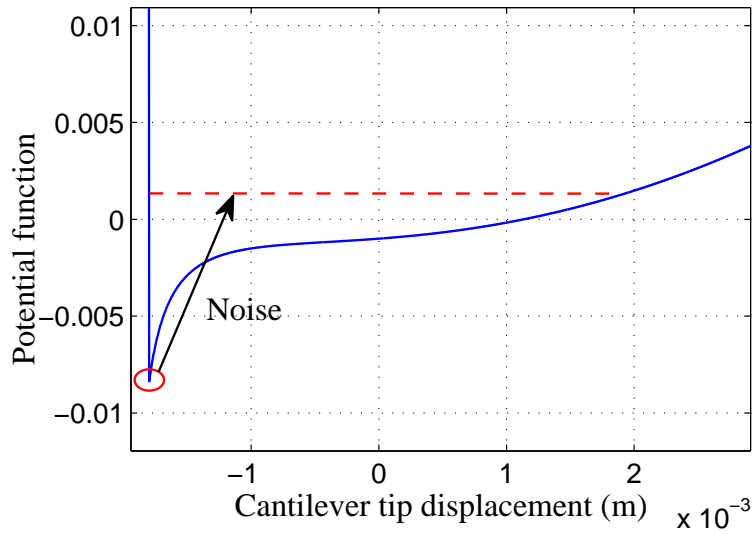


Figure 6.5: Variation of potential function with the cantilever tip displacement. The ellipse and dotted line denote the relative response locations for a harmonic excitation and a combination of harmonic excitation and noise, respectively.

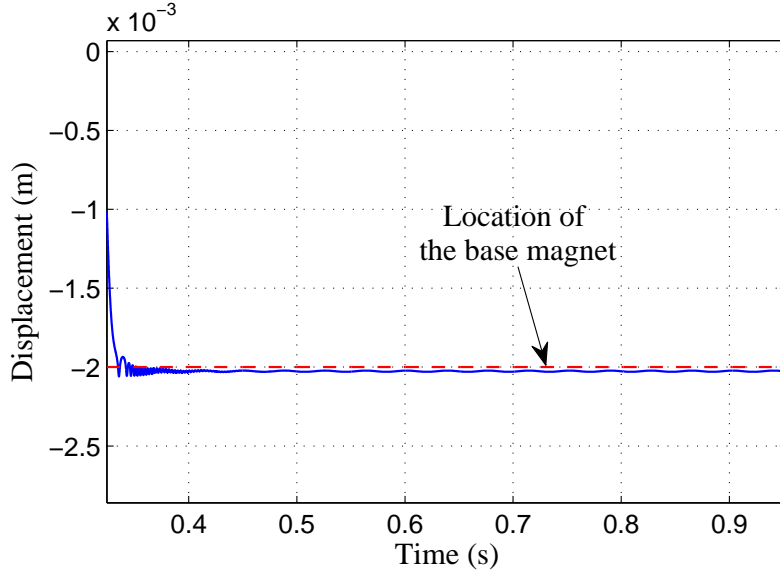


Figure 6.6: Numerically obtained displacement data for a purely harmonic excitation. The dashed horizontal line represents the base magnet location.

teraction can be obtained by integrating Eq. (6.1) and adding the potential of the cantilever to it. The double-well potential for this system is shown in Fig. 6.5.

The numerical model is described by Eq. (2.8) as in earlier studies. An Euler-Maruyama method is used to simulate the response of the cantilever beam in the presence of noise. The Langevin form of the stochastic differential equation is presented in Eq. (5.2) in the Chapter 5. For a time step of dt , the numerical solution of the system assumes the form

$$\begin{aligned}
 u_1(i) &= u_1(i-1) + u_2(i-1)dt & (6.2) \\
 u_2(i) &= u_2(i-1) - \left(\frac{k_1}{m_1}u_1(i-1) + \frac{c_1}{m_1}u_2(i-1) - \frac{1}{m_1}f_b(i-1) + \frac{1}{m_1}f_c(i-1) \right) dt \\
 &+ \sigma dW.
 \end{aligned}$$

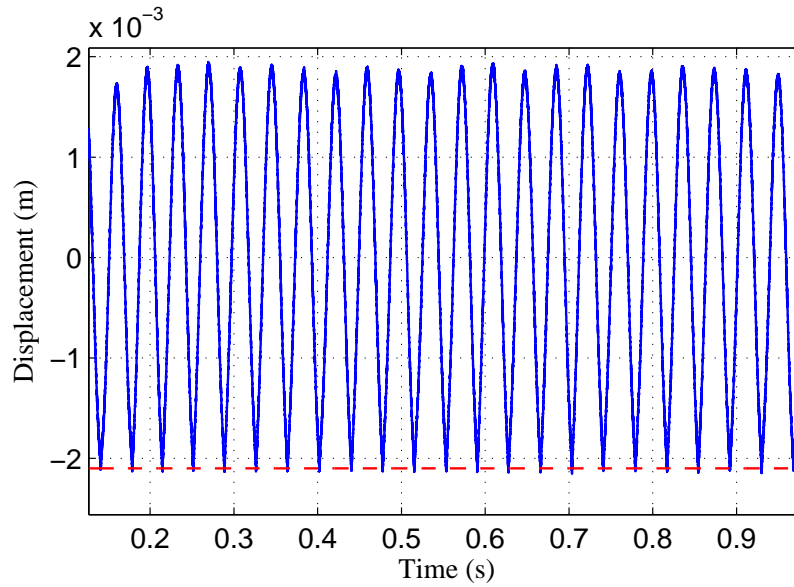


Figure 6.7: Numerically obtained displacement data when noise of SNR 51.00 is added to a harmonic base excitation. The dashed horizontal line represents the base magnet location.

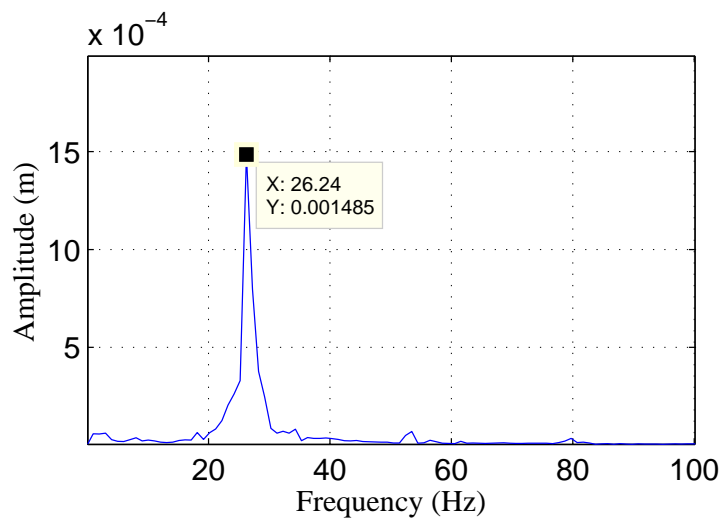


Figure 6.8: Response spectrum for the numerically obtained displacement data given in Fig. 6.7.

Table 6.1: Simulation parameter values.

Property	Value
Beam length (L)	227.00 mm
Beam area (A)	1.67 mm \times 24.00 mm
Material density (ρ)	8000.00 Kg/m ³
Cantilever Young's Modulus (E)	207.00 GPa
Thickness of base-magnet cover (A_0)	0.20 mm
Constant related to magnetic force (K_M)	20.00×10^{-7}
Constant related to elastic force (K_E)	120.00×10^5
Excitation amplitude (X_0)	0.46 mm

Here, dW is the incremental noise with standard deviation \sqrt{dt} , the index i is i^{th} time step, and dt is the step size given by: $t(i) - t(i - 1) = dt$. This numerical framework depicts the dynamics in the experiments, since, the noise is additive, which is the case when white noise is added to the system through the base excitation. Also, through this framework the stochastic dynamics can be studied accurately in the presence of high noise. The numerical simulation results are generated for the parameter values provided in Table 6.1 and presented. The numerically obtained displacement response of the cantilever tip is plotted in Fig. 6.6 when the excitation is purely harmonic. The dotted line represents the location of the base magnet. No detectable response is observed for these conditions. The numerical simulation results imply that the tip sticks to the sample and there is no oscillatory response. This situation

corresponds to the experimental results presented in Fig. 6.2(b). The response of the system is trapped in the first potential well (arising due to the attractive force), as shown in Fig. 6.5.

When noise of SNR 51 is added to the system, the resulting response of the cantilever tip is shown in Fig. 6.7. The dotted line represents the location of the base magnet. The solution for this case (with added noise) is indicated by the dotted line in the double well potential shown in Fig. 6.5. The numerically obtained response amplitude is seen to compare well with the experimental data presented in Fig. 6.3. The response spectrum of this numerically obtained data presented in Fig. 6.8 confirms that the response is dominated by a component at the excitation frequency.

6.3 Analytical framework and numerical results

The effects of noise on sticking cantilevers are studied by the analytical framework developed in Chapter 5. As in previous studies, instead of using the combination of magnetic attraction and DMT force, as done in the direct numerical simulations, the author uses a different force profile to derive the moment equations, as the prior force combination results in the appearance of negative and fractional moments.

This new force profile is given by

$$f_{ts} = (Au_1^2 + Bu_1 + C) h(\alpha - u_1). \quad (6.3)$$

In Eq. (6.3), h represents the Heaviside function, and the parameter α is given by:

$$\alpha = \frac{-1}{\phi_1} (\nu \cos \Omega\tau + \eta - \xi).$$

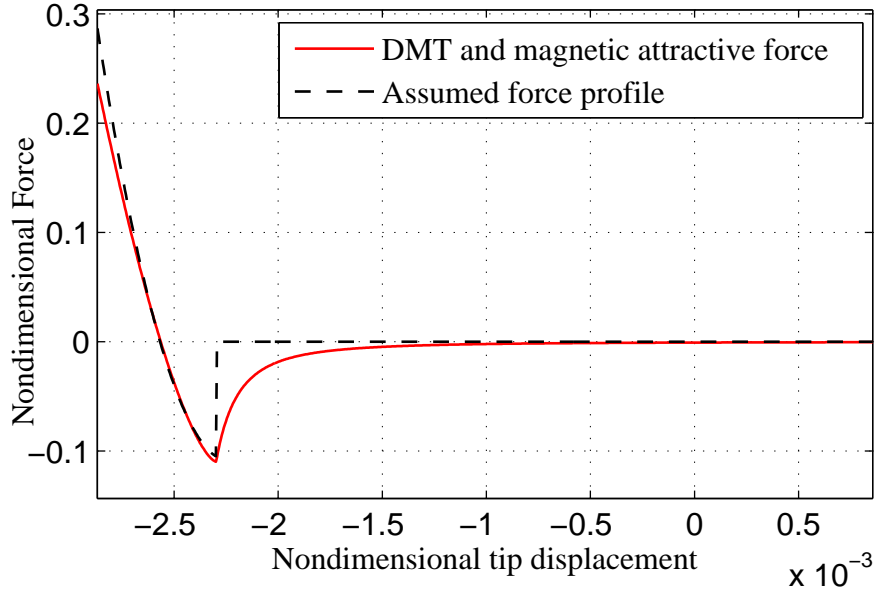


Figure 6.9: Comparison of the assumed force profile with the DMT and magnetic attractive force profile.

The use of Heaviside function accounts for the discontinuous nature of the contact forces experienced by the cantilever tip. Since the assumed force profile has quadratic form, both the repulsive and the attractive regime of tip-sample forces can be successfully modeled by Eq. (6.3). The constants A , B , and C are tuned to get a profile as close to the original force profile as that used in the numerical studies. The selected values of the different parameters are as follows:

$$A = 9.8 \times 10^5, \quad B = 4.4 \times 10^3, \quad C = 4.8.$$

The assumed force profile given by Eq. (6.3) and the combination of magnetic attraction and DMT contact forces, which is given by Eq. (6.1), are compared in Fig. 6.9.

The moment-evolution equations are obtained by multiplying both sides of Eq.

(5.5) by $u_1^m u_2^n$ and then integrating both sides of the equation over the considered domain. The resulting system has the form

$$\begin{aligned}
\frac{d \langle u_1^m u_2^n \rangle}{dt} = & m \langle u_1^{m-1} u_2^{n+1} \rangle - n \frac{c_1}{m_1} \langle u_1^m u_2^n \rangle \\
& - n \frac{k_1}{m_1} \langle u_1^{m+1} u_2^{n-1} \rangle + n \frac{f_b}{m_1} \langle u_1^m u_2^{n-1} \rangle \\
& + \frac{\phi_1}{m_1} h(\alpha - \langle u_1 \rangle) [An \langle u_1^{m+2} u_2^{n-1} \rangle] \\
& - \frac{\phi_1}{m_1} h(\alpha - \langle u_1 \rangle) [Bn \langle u_1^{m+1} u_2^{n-1} \rangle] \\
& + \frac{\phi_1}{m_1} h(\alpha - \langle u_1 \rangle) [C \langle u_1^m u_2^{n-1} \rangle] \\
& + \frac{\sigma^2}{2} n(n-1) \langle u_1^m u_2^{n-2} \rangle.
\end{aligned} \tag{6.4}$$

In the moment-evolution equations given by Eq. (6.4), since the moments of order n and m involve moments of order $n+1$ and $m+1$, the moment hierarchy grows indefinitely. At this point, the truncation of higher order moments after some order is required, to make the moment equations amenable to a numerical solution. The moments are truncated for moments of order 4 and higher, following the work described in Chapter 5.

Here, moments of order 4 and higher are neglected, which results in a set of 9 coupled ODEs. The variables of the moment equations are given by

$$\begin{aligned}
x_1 &= \langle u_1 \rangle, & x_2 &= \langle u_2 \rangle, & x_3 &= \langle u_1^2 \rangle, \\
x_4 &= \langle u_1 u_2 \rangle, & x_5 &= \langle u_2^2 \rangle, & x_6 &= \langle u_1^3 \rangle, \\
x_7 &= \langle u_1^2 u_2 \rangle, & x_8 &= \langle u_1 u_2^2 \rangle, & x_9 &= \langle u_2^3 \rangle.
\end{aligned}$$

The system of coupled moment evolution equations are given by

$$\dot{x}_1 = x_2 \tag{6.5}$$

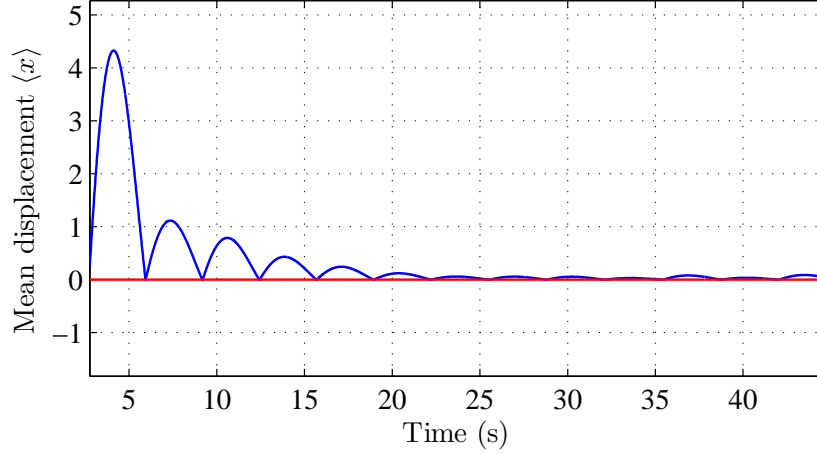


Figure 6.10: Evolution of the first moment with time when $\sigma = 0.00$. The solid horizontal line represents the base magnet location.

$$\dot{x}_2 = -Cx_2 - Kx_1 + F_b + H(Ax_3 - Bx_1 + C) \quad (6.6)$$

$$\dot{x}_3 = 2x_4 \quad (6.7)$$

$$\dot{x}_4 = x_5 - Cx_4 - Kx_3 + F_b x_1 + H(Ax_6 - Bx_3 + Cx_1) \quad (6.8)$$

$$\dot{x}_5 = -2Cx_5 - 2Kx_4 + 2F_b x_2 + 2H(Ax_7 - Bx_4 + Cx_2) + \sigma^2 \quad (6.9)$$

$$\dot{x}_6 = 3x_7 \quad (6.10)$$

$$\dot{x}_7 = 2x_8 - Cx_7 - Kx_6 + F_b x_3 + H(-Bx_6 + Cx_3) \quad (6.11)$$

$$\dot{x}_8 = x_9 - 2Cx_8 - 2Kx_7 + 2F_b x_4 + 2H(-Bx_7 + Cx_4) + \sigma^2 x_1 \quad (6.12)$$

$$\dot{x}_9 = -3Cx_9 - 3Kx_8 + 3F_b x_5 + 3H(-Bx_8 + Cx_5) + 3\sigma^2 x_2. \quad (6.13)$$

In equations (6.5) to (6.13), the different coefficients take the form

$$C = \frac{c_1}{m_1}, K = \frac{k_1}{m_1}, F_b = \frac{f_b}{m_1}, H = \frac{\phi_1}{m_1} h(\alpha - x_1).$$

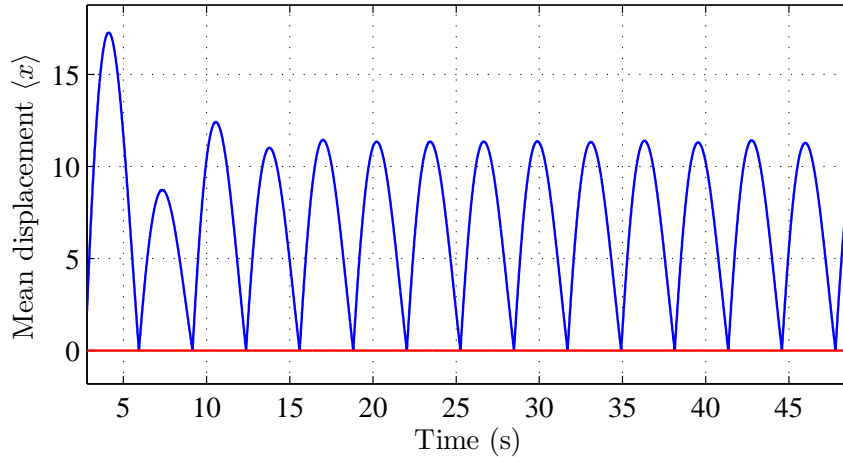


Figure 6.11: Evolution of the first moment with time when $\sigma = 0.06$. The solid horizontal line represents the base magnet location.

The parameter values for the numerical simulations of the moment-evolution equations are identical to those listed in Table 6.1. The mean value of displacement, which is characterized by the first moment, is plotted in Fig. 6.10, when the noise strength $\sigma = 0$. It is observed that the mean value of the displacement stays close to the surface boundary, denoted by the solid line. This observation is consistent with the previous numerical and experimental observations, wherein the tip magnet sticks with the base magnet when there is no added noise.

The mean tip displacement is plotted in Fig. 6.11, when the strength of the noise $\sigma = 0.06$. In this case, the evolution of the mean value of the displacement suggests that intermittent contact between the tip and the sample takes place due to the introduction of noise. For these simulations, the probability distribution has been modeled as a sharp Gaussian distribution with the mean value of 0.01 and a variance of 0.0625. The numerical evolution of moments show qualitatively the same

behavior as that seen in the experimental and numerical studies. It is seen that the noise addition to the deterministic input prevents the phenomenon of sticking of the cantilever tip and allows for a resumption of periodic motions wherein intermittent contact is made by the tip with the sample.

6.4 Summary

In this chapter, a combination of experimental, numerical, and analytical efforts are used to study the effects of additive noise input on the dynamics of a macro-scale elastic cantilever subjected to nonlinear interaction forces at its tip. It is experimentally observed that the cantilever tip sticks with the base magnet when the cantilever base excitation is purely harmonic. The addition of Gaussian white noise to the excitation makes the cantilever tip overcome the strong attractive force and resume its periodic motions. Numerical studies based on Euler-Maruyama method and analytical framework based on a moment evolution approach is conducted, to complement the experimental work. These studies support the finding that the addition of noise of a certain level can help prevent the sticking of the cantilever tip to the sample due to the attractive force. Since, nonlinear phenomena have been observed to be common across different length scales, the present efforts can form the basis for a method to prevent the sticking of micro-scale cantilevers including AFM cantilevers.

Chapter 7

Summary and Recommendations for Future Work

7.1 Summary

This dissertation work is focused on the dynamics of impacting elastic cantilevers at different length scales. A micro-scale (AFM) cantilever and a macro-scale cantilever are studied in detail. Bifurcations related to near-grazing impacts in the context of tapping mode operations of an AFM are examined. The base-excited AFM micro-cantilever is subjected to long-range attractive force and short-range repulsive forces. Effectively, this system behaves as a system subjected to non-smooth interaction forces. Physically, the contact between the tip and the sample accounts for the discontinuous nature of the tip-sample forces in an AFM. The dynamics of this type of non-smooth systems can exhibit various interesting phenomena. Various types of qualitative changes (bifurcations) are observed when the solution of a system grazes or makes tangential contact with the boundary of the discontinuity. A driver for this dissertation is to utilize nonlinear phenomena to propose a method of operation of an AFM, which can help reduce the unwanted repulsive interaction force between the cantilever tip and sample. Period-doubling bifurcations are studied in detail for off-resonance excitation of an AFM cantilever. In order to better understand the system dynamics in the micro-scale AFM system, a macro-scale experimental system is constructed with similar tip-sample interaction forces. This

macro-scale experimental system is used as a tool to understand and predict non-linear phenomena in AFM. A reduced order numerical model is derived for both the macro-scale and micro-scale systems, and the responses of these systems are studied for off-resonance excitation frequencies. Period-doubling bifurcations are studied through experimental and numerical efforts in both the macro-scale and micro-scale systems. Experiments are conducted with a commercial AFM, and period-doubling phenomenon was used to identify near-grazing contact between the tip and the sample. Different force models are used for the tip-sample interaction, and the period-doubling responses are observed for interactions with soft biological samples. Grazing bifurcations are further analyzed with zero-time discontinuity maps. A $3/2$ singularity is observed in the discontinuity map; this is expected in systems where the forces are continuous at the point of grazing contact. The stability of the periodic orbits were analyzed from the local Poincaré maps obtained from an empirical method.

A new method of operation of tapping mode AFM through advantageous use of nonlinear phenomenon is proposed in this work. Period-doubling qualitative changes can be employed to identify near-grazing contact; this can reduce “undesired” levels of repulsive tip-sample forces. This method can also serve as a means to identify contact between the tip and the sample in tapping mode operations.

Another important aspect of this work is the examination of effects of noise on the dynamics of macro-scale and micro-scale systems. The stochastic effects are studied through experimental and numerical methods. Gaussian white noise of a prescribed level is added with the harmonic excitation in the input to examine

the effects of noise. In addition to studying the effects of noise through numerical and experimental means, an analytical framework is developed where Fokker-Planck equations are studied through moment evolution equations. The moment equations are analyzed numerically to obtain the averaged dynamics of the system in the presence of noise. The phenomenon observed in experimental and numerical analysis is verified through the analytical framework developed here. The effects of noise are studied for excitation frequencies at and away from resonance frequency of the system. It is observed that noise can be utilized to induce contact between the cantilever tip and the sample surface from a previously non-contact state. Also, it is shown that noise can be used to avoid the sticking of cantilever tip and sample that can occur due to high attractive forces.

7.2 Recommendations for future work

There can be many extensions of this dissertation work which can proceed along different directions. The off-resonance operation of AFM, described in this dissertation can be applied in the case of tapping mode operation in liquid environments. Repulsive contact forces are harmful for imaging soft biological samples, which are generally imaged in liquid environments. The samples can be destroyed if the repulsive interaction forces are high. The procedure of identifying grazing contact by period-doubling bifurcations can be extended for operation in liquids. The modeling of the tip-sample forces in liquids will be different from what has been described in this work. The response of the micro-cantilever is influenced by

the presence of a liquid and electro-static forces, which come into play between the tip and sample in the long-range. For operations in liquids, the quality factors will have to be appropriately chosen. Numerical methods with fluid-structure interactions can be used to accurately model the dynamics of a vibrating micro-cantilever in liquid.

Another important direction described in this dissertation work is the effects of noise in micro-scale systems. Noise effects are important in AFM operations, and it is seen that noise plays an important role in the response of the system. In this dissertation work, preliminary investigation has been carried out into the effects of noise on sticking. The effects of noise on the phenomenon of hysteresis is important and it can be studied with a goal of applying the findings in AFM operations. In the future, experimental efforts in an actual AFM can be undertaken to study the effects of noise along with a harmonic component in the input signal. Another significant issue which can be considered is the role of multiplicative noise in the system, which might arise from the feedback controller. Building on the current work, the effects of noise on tip-sample forces can be further studied.

Appendix A

Computational Modeling with Multiple Modes

In the Galerkin projection carried out in Section 2.3 of Chapter 2, a single mode approximation is assumed to determine the response of the system. If one assumes the participation of n modes in the response of the cantilever, the cantilever displacement can be expressed as

$$\bar{w}(\bar{s}, \tau) = \sum_{r=1}^n q_r(\tau) \phi_r(\bar{s}). \quad (\text{A.1})$$

The details of the terms in Eq. (A.1) can be found in Chapter 2. Carrying out a Galerkin projection with a multi-mode approximation, the equation of motion assumes the form

$$[M] \{\ddot{q}\} + [C] \{\dot{q}\} + [K] \{q\} = \{f_b\} + \{f_c\}. \quad (\text{A.2})$$

The components of the modal matrices and the force vectors are listed below.

$$M_{ij} = \int_0^1 \phi_i \phi_j d\bar{s} + \gamma \phi_i(1) \phi_j(1) \quad (\text{A.3})$$

$$K_{ij} = \omega_j^2 \int_0^1 \phi_i \phi_j d\bar{s} \quad (\text{A.4})$$

$$C_{ij} = 2\omega_j \zeta_j M_{ij} \int_0^1 \phi_i \phi_j d\bar{s} \quad (\text{A.5})$$

$$f_{b_i} = \left(\int_0^1 \phi_i d\bar{s} \right) \omega^2 \nu \cos(\omega t) \quad (\text{A.6})$$

$$f_{c_i} = \phi_i(1) f_{ts} \quad (\text{A.7})$$

Here, the subscript i stands for the i^{th} mode shape of the cantilever. In Figures A.1 and A.2, the displacements and the velocities obtained on the basis of a single mode

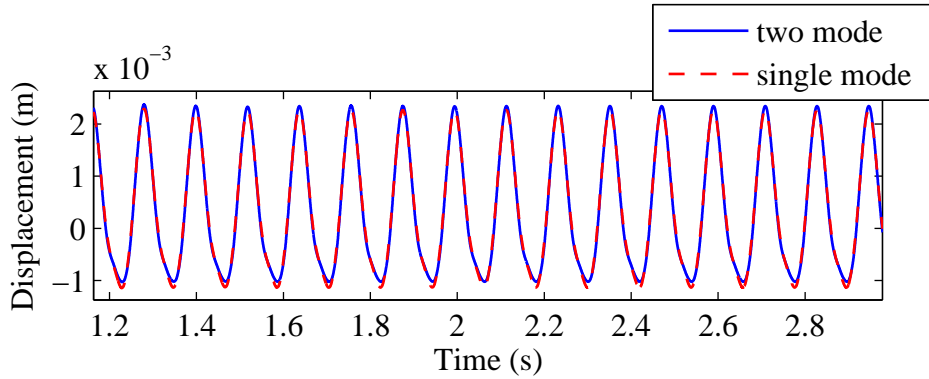


Figure A.1: Comparison of displacements with a single mode and a two-mode approximation for computational studies in macro-scale.

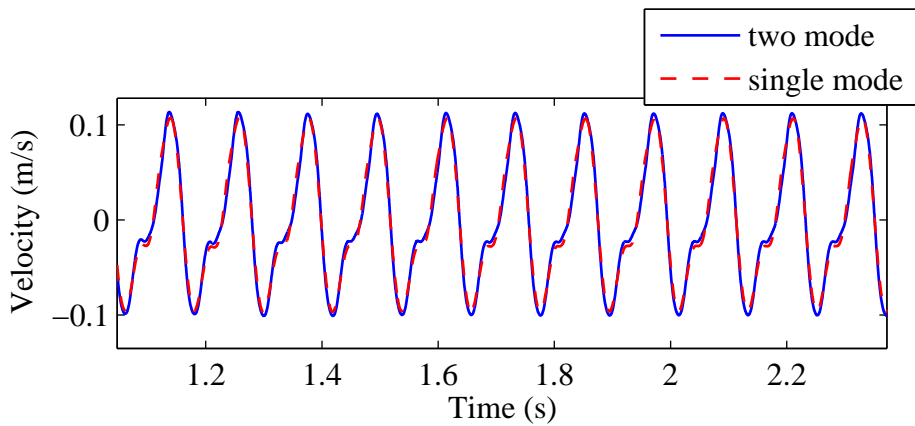


Figure A.2: Comparison of velocities with a single mode and a two-mode approximation for computational studies in macro-scale.

approximation and a two-mode approximation are compared in the macro-scale case. These comparisons are for the constrained case, and it is observed that the higher mode does not account much for the tip response, as reported in Chapter 2. These studies need to be examined further to carefully understand the participation of higher modes in the response.

Appendix B

Derivation of Moment Evolution Equations

The Fokker Planck Equation given by Eq. (5.5) is satisfied by probability density P . Considering $P = P(x, y, t)$, one can write

$$\int \int s \frac{\partial P}{\partial t} dx dy = \frac{d \langle s \rangle}{dt}$$

Multiplying both sides of Eq. (5.5) by $u_1^m u_2^n$ and integrating, it is found that

$$\begin{aligned} \int \int u_1^m u_2^n \frac{\partial P}{\partial t} du_1 du_2 = & - \int \int u_1^m u_2^{n+1} \frac{\partial P}{\partial u_1} du_1 du_2 + \frac{c_1}{m_1} \int \int u_1^m u_2^n P du_1 du_2 \\ & + \frac{c_1}{m_1} \int \int u_1^m u_2^{n+1} \frac{\partial P}{\partial u_2} du_1 du_2 + \frac{k_1}{m_1} \int \int u_1^{m+1} u_2^n \frac{\partial P}{\partial u_2} du_1 du_2 \\ & - \frac{f_b}{m_1} \int \int u_1^m u_2^n du_1 du_2 - \frac{1}{m_1} \int \int u_1^m u_2^n f_{ts} du_1 du_2 \\ & + \frac{\sigma^2}{2} \int \int u_1^m u_2^n \frac{\partial^2 P}{\partial u_2^2} du_1 du_2. \end{aligned} \quad (\text{B.1})$$

Here, each term of Eq. (B.1) will be expanded individually. The left-hand side of Eq. (B.1) can be expanded as

$$\int \int u_1^m u_2^n \frac{\partial P}{\partial t} du_1 du_2 = \frac{d \langle u_1^m u_2^n \rangle}{dt}. \quad (\text{B.2})$$

The first term on the right hand side of Eq. (B.1) will be

$$\begin{aligned} - \int \int u_1^m u_2^{n+1} \frac{\partial P}{\partial u_1} du_1 du_2 &= - \int u_2^{n+1} du_2 \int u_1^m dP \\ &= - \int u_2^{n+1} du_2 \left([u_1^m P]_{-\infty}^{\infty} - \int P m u_1^{m-1} du_1 \right) \\ &= \int m P u_1^{m-1} u_2^{n+1} du_1 du_2 \\ &= m \langle u_1^{m-1} u_2^{n+1} \rangle. \end{aligned} \quad (\text{B.3})$$

It is noted in Eq. (B.3) that the first term after itegration by parts goes to 0, as P is 0 when u_1 or u_2 goes to ∞ . The second term is

$$\frac{c_1}{m_1} \int \int u_1^m u_2^n P du_1 du_2 = \frac{c_1}{m_1} \langle u_1^m u_2^n \rangle. \quad (\text{B.4})$$

The third term is

$$\begin{aligned} \frac{c_1}{m_1} \int \int u_1^m u_2^{n+1} \frac{\partial P}{\partial u_2} du_1 du_2 &= -\frac{c_1}{m_1} \int u_1^m du_1 \int u_2^{n+1} dP \\ &= \frac{c_1}{m_1} \int u_1^m du_1 \left([u_2^{n+1} P]_{-\infty}^{\infty} - \int (n+1) P u_2^n du_2 \right) \\ &= -\frac{c_1}{m_1} (n+1) \int m P u_1^m u_2^n du_1 du_2 \\ &= -(n+1) \frac{c_1}{m_1} \langle u_1^m u_2^n \rangle. \end{aligned} \quad (\text{B.5})$$

The fourth term is

$$\begin{aligned} \frac{k_1}{m_1} \int \int u_1^{m+1} u_2^n \frac{\partial P}{\partial u_2} du_1 du_2 &= \frac{k_1}{m_1} \int u_1^{m+1} du_1 \int u_2^n dP \\ &= \frac{k_1}{m_1} \int u_1^{m+1} du_1 \left([u_1^n P]_{-\infty}^{\infty} - \int P n u_2^{n-1} du_2 \right) \\ &= -\frac{k_1}{m_1} \int n P u_1^{m+1} u_2^{n-1} du_1 du_2 \\ &= -n \frac{k_1}{m_1} \langle u_1^{m+1} u_2^{n-1} \rangle. \end{aligned} \quad (\text{B.6})$$

The fifth term is

$$\begin{aligned} -\frac{f_b}{m_1} \int \int u_1^m u_2^n \frac{\partial P}{\partial u_2} du_1 du_2 &= -\frac{f_b}{m_1} \int u_1^m du_1 \int u_2^n dP \\ &= -\frac{f_b}{m_1} \int u_1^m du_1 \left([u_1^n P]_{-\infty}^{\infty} - \int P n u_2^{n-1} du_2 \right) \\ &= \frac{f_b}{m_1} \int n P u_1^m u_2^{n-1} du_1 du_2 \\ &= n \frac{f_b}{m_1} \langle u_1^m u_2^{n-1} \rangle \end{aligned} \quad (\text{B.7})$$

The sixth term involves the tip-sample forces which includes the tip-sample forces. Here, the tip-sample forces are of the form shown in Eq. (6.3). So the sixth term becomes

$$\begin{aligned}
& -\frac{\phi_1 \bar{\beta}}{m_1} \int \int u_1^m u_2^n (-\bar{a} + u_1^2) h(\bar{a} - u_1) \frac{\partial P}{\partial u_2} du_1 du_2 \\
= & \frac{\phi_1 \bar{\beta}}{m_1} h(\bar{a} - u_1) \left[\bar{a} \int \int u_1^m u_2^n \frac{\partial P}{\partial u_2} du_1 du_2 - \int \int u_1^{m+2} u_2^n \frac{\partial P}{\partial u_2} du_1 du_2 \right] \\
& = \frac{\phi_1 \bar{\beta}}{m_1} h(\bar{a} - u_1) \left[-\bar{a} n \langle u_1^m u_2^{n-1} \rangle + n \langle u_1^{m+2} u_2^{n-1} \rangle \right]. \quad (\text{B.8})
\end{aligned}$$

The last and the seventh term is

$$\begin{aligned}
& \frac{\sigma^2}{2} \int \int u_1^m u_2^n \frac{\partial^2 P}{\partial u_2^2} du_1 du_2 = \frac{\sigma^2}{2} \int u_1^m du_1 \int u_2^n \frac{\partial^2 P}{\partial u_2^2} du_2 \\
& = \frac{\sigma^2}{2} \int u_1^m du_1 \left(\left[u_1^n \frac{dP}{du_2} \right]_{-\infty}^{\infty} - \int \frac{dP}{du_2} n u_2^{n-1} du_2 \right) \\
& = -\frac{\sigma^2}{2} \int u_1^m du_1 \int \frac{dP}{du_2} n u_2^{n-1} du_2 \\
= & \frac{\sigma^2}{2} \int u_1^m du_1 \left([n u_1^{n-1} P]_{-\infty}^{\infty} - \int P n(n-1) u_2^{n-2} du_2 \right) \\
& = n(n-1) \frac{\sigma^2}{2} \langle u_1^m u_2^{n-2} \rangle \quad (\text{B.9})
\end{aligned}$$

The moment evolution equation comes out to be

$$\begin{aligned}
\frac{d \langle u_1^m u_2^n \rangle}{dt} = & m \langle u_1^{m-1} u_2^{n+1} \rangle - n \frac{c_1}{m_1} \langle u_1^m u_2^n \rangle - n \frac{k_1}{m_1} \langle u_1^{m+1} u_2^{n-1} \rangle + \\
& n \frac{f_b}{m_1} \langle u_1^m u_2^{n-1} \rangle + \frac{\phi_1 \bar{\beta}}{m_1} h(\bar{a} - u_1) \left[-\bar{a} n \langle u_1^m u_2^{n-1} \rangle + n \langle u_1^{m+2} u_2^{n-1} \rangle \right] + \\
& \frac{\sigma^2}{2} n(n-1) \langle u_1^m u_2^{n-2} \rangle \quad (\text{B.10})
\end{aligned}$$

Appendix C

Matlab Codes

C.1 Representative Matlab code for macro-scale system

```
% This script is used to compute nondimensional parameters and find out
% where grazing and period doubling bifurcations take place for
% both of the cantilever systems.

%The same code is used for micro-scale system by changing
% the parameters

clear all

close all

clc

%% Different input parameters

global m_tip rho A L;

global KE rho A L omega ;

global M K C ;

global eta xi;

global phiat1 KM ;

global zeta Omega nu phids0to1 Asel phaiat1;

%% Beam specifications
```

```

m_tip = 0.0943e-3;          % mass of the beam tip in macro-scale (Kg);
                               % this will be zero in
                               % micro-scale

rho = 2700;                  % density of cantilever beam material

E = 70e9;                   % modulus of elasticity in GPa

L = 296e-3;                 % beam length in m

h = 0.95e-3;                % beam thickness in m

b = 20e-3;                  % beam width in m

A = b * h;                  % Area of cross section of the beam in m^2

I = (1/12) * b * h^3;       % Area moment of inertia of the beam in m^4

A0 = 5e-3;                  % thickness of foam

%% Contact specifications

Q = 10;                     % Quality factor

KM = 4.3e-10 ; KE =2.3e3;   % Constants related to contact forces

d = 0.7e-3;                 % initial distance between tip and sample

X0 = 0.44e-3;               % Excitation amplitude

nu = X0/L;                  % nondimensional excitation amplitude

xi = A0/L;                  % nondimensional foam thickness

eta = d/L;                  % nondimensional initial distance

beta_initial = 1.875;

beta = fsolve(@eigenproblem,beta_initial); % beta obtained from the eigenproblem

%% find the natural frequency omega from beta

omega = sqrt  ( (beta / L)^4 * ((E * I) / (rho * A)))

```

```

% first natural frequency

omegadr =2.32* omega ;

% excitation frequency

Omega = omegadr/omega;

% nondimensional excitation frequency

%% terms in the equation of motion

gamma = (m_tip / (rho * A * L) );           % nondimensional tip mass

phids0to1 = quadl(@(x)phi(beta/L,x) , 0, 1) ;

M = quadl(@(x)phisq (beta/L,x),0,1)+ gamma* (phi (beta/L , 1))^2;

K = quadl(@(x)phisq (beta/L,x),0,1);

zeta = 1/2/Q;

C = 2 * M * zeta ;

phiat1 = phi (beta , 1) ;

%% Solve for the unconstrained motion:

Asel=1;

dtau_uc = 1e-2;

T_uc = 0:dtau_uc:3*omega;

x0_uc = [.5e-4/L; 0];

[t_uc,x_uc] = ode45(@(t_uc,x_uc)EOM(t_uc,x_uc) , T_uc , x0_uc);

dist_uc = (x_uc(:,1).*phiat1 + nu.*cos(Omega.*t_uc))*L;

% Dimensional displacement

vel_uc = (x_uc(:,2).*phiat1 -Omega.*nu.*sin(Omega.*t_uc))*L*omega;

% Dimensional velocity

```

```

figure(1)

plot(dist_uc(7000:length(t_uc)),vel_uc(7000:length(t_uc)),'r','linewidth',1)

    hold on

%% Solve for constrained motion

r =7000;

Asel=2;

dtau = 1e-2;          % time step

T = 0:dtau:3*omega;

x0 = [.5e-4/L; 0];    % Initial condition

[t,x] = ode45(@(t,x)EOM(t,x) , T , x0);

dist = (x(:,1).*phiat1 + nu.*cos(Omega.*t))*L;

% Displacement in m

vel = (x(:,2).*phiat1 -Omega.*nu.*sin(Omega.*t))*L*omega;

% Velocity in m/s

plot(dist(r:length(t)),vel(r:length(t)),'linewidth',1)

axis([-2e-3 3e-3 -.2 .15])

hold on

boundary=linspace(L*eta,L*eta,10);

boundary_plot=linspace(min(vel),max(vel),10);

plot(-boundary,boundary_plot)

set(gca,'FontSize',12)

xlabel('Displacement (m)','fontsize',12,'fontname','Times')

ylabel('Velocity (m/s)','fontsize',12,'fontname','Times')

```



```

box on

hold on

%% Poincare section to locate period-doubling

dd = dist(r:r+1000);

wer = max(dd);

for i = 1:length(dd)

    rr = dd(i);

    if ( rr == wer )

        h = i;

    end

end

time = T(r:length(t));

disti = dist (r:length(t));

veli = vel(r:length(t));

Tp = 2*pi/omegadr;

time_st_nu = omega * Tp / dtau ;

gt = ceil(time_st_nu);

for i = 1:15

disp(i)=disti(h);

velg(i)=veli(h);

h = h +gt;

end

plot(disp,velg,'k.','MarkerSize',20)

```

```

xlabel('Displacement (m)', 'fontsize', 14, 'fontname', 'Times');
ylabel('Velocity, m/s', 'fontsize', 14, 'fontname', 'Times');

set(gca, 'FontSize', 12);

hold on

dd = dist(r:r+1000);

wer = max(dd);

for i = 1:length(dd)

    rr = dd(i);

    if ( rr == wer )

        h = i;

    end

end

time = T(r:length(t));

disti = dist_uc (r:length(t));

veli = vel_uc(r:length(t));

Tp = 2*pi/omegadr;

time_st_nu = omega * Tp / dtau ;

gt = ceil(time_st_nu);

for i = 1:15

    disp(i)=disti(h);

    velg(i)=veli(h);

    h = h +gt;

end

```

```

        plot(displ,velg,'k.','MarkerSize',20)

        box('on');

        hold('all');

        %% plot the tip-sample forces

N = r;

s = x(N:length(T),1);

tt = t(N:length(T),1);

for i = 1 : length (s)

    Dist(i) = phiat1 * real( s (i) ) + eta + nu*cos(Omega*tt(i));

    magdist = Dist + xi;

if (Dist(i) <= 0)

    Fc(i) = contact_force (Dist(i)) + magnetforce(xi) ;

else

    Fc(i) = magnetforce(magdist(i)) ;

end

end

figure(2)

plot (T(N:length(T)),Fc,'r')

hold on

plot (T(N:length(T)),Dist)

%% plot the FFT

r = 6000;

dt = (t_uc(3)-t_uc(2))/omega;           %divided by omega for renormalization

```

```

fs = 1/dt;

y1 = dist_uc(r:length(dist_uc));

l=length(y1);

F11 = fft(y1)/l;

F11(1) = 0;

fq = linspace (0,fs,length(F11));

subplot(2,1,1)

plot(fq,(2*abs(F11)))

axis([0 30 0 .003])

set(gca,'FontSize',12)

xlabel('Frequency, Hz','fontsize',12,'fontname','Times')

ylabel('Amplitude, m','fontsize',12,'fontname','Times')

box on

dt = (t(3)-t(2))/omega; %divided by omega for renormalization

fs = 1/dt;

y = dist(r:length(dist));

l=length(y);

F1 = fft(y)/l;

F1(1) = 0;

fq = linspace (0,fs,length(F1));

subplot(2,1,2)

plot(fq,(2*abs(F1)))

axis([0 30 0 .003])

```

```

set(gca,'FontSize',12)

xlabel('Frequency, Hz','fontsize',12,'fontname','Times')

ylabel('Amplitude, m','fontsize',12,'fontname','Times')

box on

%% Function : EOM

function xdot = EOM (t,x)

global m_tip rho A L;

global KE rho A L omega ;

global M K C ;

global eta xi;

global phiat1 KM ;

global zeta Omega nu phids0to1 Ase1 phiat1;

Fb = (Omega)^2 * nu * phids0to1 * cos (Omega * t) ;

Dist = phiat1 * x(1) + eta + nu*cos(Omega*t);

magdist = Dist + xi;

if (Ase1==1)

% condition of constrained or unconstrained motion

    Fc=0;

elseif(Ase1==2)

% interaction forces

if (Dist <= 0)

    Fc = contact_force (Dist) + magnetforce(xi);

else

```

```

    Fc = magnetforce(magdist);

end

end

xdot(1) = x(2);

xdot(2) = (1/M) * ( -C * x(2) - K * x(1) + ( Fb + phiat1 * Fc ) ) ;

    xdot = [ xdot(1) ; xdot(2) ] ;

%% Function: magnetforce

Function F = magnetforce(x)

global KM rho A L omega

F = - (KM/ (rho * A * L^2 * omega^2))*(1/x)^2;

function f = contact_force (x)

global KE rho A L omega ;

f = (KE/( rho* A* sqrt( L ) * omega^2 ) ) .* (- x)^1.5 ;

%% Function: eigenproblem

function [sdet]= eigenproblem (beta);

global m_tip rho A L;

gamma = m_tip / (rho * A * L);

% this program determines beta by setting sdet to zero

% which accounts for the third boundary condition

s11 = beta^2*(-sin(beta) - sinh(beta));

s12 = beta^2*(-cos(beta) - cosh(beta));

s21 = beta^3*(-cos(beta) - cosh(beta)) + gamma*beta^4*(sin(beta) - sinh(beta));

s22 = beta^3*( sin(beta) - sinh(beta)) + gamma*beta^4*(cos(beta) - cosh(beta));

```

```

s=[s11 s12;s21 s22];

sdet=det(s);

%% Function: phi

% This function accounts for the mode shape

function z = phi (beta, x)

global L

% first find the constant to orthonormalize the mode shapes

% z_un is the unnormalized mode shape

% the beta considered here is beta*L

% as xi is the nondimensional spatial term xi = x/L

z_orth = quadl (@(x)phisquare_un(beta,x), 0 , L);

C = 1 / sqrt (z_orth) ;

z = C *(sin (beta * L*x) - sinh (beta * L*x) - ...

((sin (beta *L ) + sinh (beta*L ))/(cos (beta*L )...

+ cosh (beta*L )))*(cos (beta *L* x) - cosh (beta * L*x)));

function z_un = phisquare_un (beta, xi)

global L

z_un1 = (sin (beta * xi) - sinh (beta * xi) - ...

((sin (beta*L ) + sinh (beta*L ))/(cos (beta*L )...

+ cosh (beta *L )))*(cos (beta * xi) - cosh (beta * xi)));

z_un2 = (sin (beta * xi) - sinh (beta * xi)...

- ((sin (beta*L ) + sinh (beta*L ))/(cos (beta*L )...

+ cosh (beta *L )))*(cos (beta * xi) - cosh (beta * xi)));

```

```
z_un = z_un1 .* z_un2;  
  
%% Function: phisq  
  
function x = phisq (beta, x)  
  
x = phi (beta, x) .* phi (beta, x) ;
```


Bibliography

- Balachandran, B.** (2003). Dynamics of an elastic structure excited by harmonic and aharmonic impactor motions. *Journal of Vibration and Control* **9**(3-4): 265-279.
- Basak, S. and Raman, A.** (2007). Dynamics of tapping mode atomic force microscopy in liquids: Theory and experiments. *Applied Physics Letters* **91**: 064107.
- Basso, M., Dahleh, M., Mezic, I., and Salapaka, M. V.** (1999). Stochastic Resonance in AFMs. *Proceedings of the American Control Conference*, San Diego, California, June.
- Binnig, G., Quate C. F., and Gerber, C.** (1987). Atomic Force Microscope. *Physical Review Letters* **56**(9): 930-933.
- Butt, H. and Jaschke, M.** (1995). Calculation of thermal noise in atomic force microscopy. *Nanotechnology* **6**: 1-7.
- Chakraborty, I. and Balachandran, B.** (2009). Cantilever dynamics with attractive and repulsive tip interactions. *Proceedings of ASME International Mechanical Engineering Congress and Exposition IMECE* 2009-10330.
- Chakraborty, I. and Balachandran, B.** (2011a). Off-resonance cantilever dynamics in the presence of attractive and repulsive tip interaction forces. *International Journal of Structural Stability and Dynamics* **11**(4): 603-620.
- Chakraborty, I. and Balachandran, B.** (2011b). Noise influenced elastic cantilever dynamics with nonlinear tip interaction forces, *Nonlinear Dynamics* **66**: 427-439, (2011)
- Chakraborty, I. and Balachandran, B.** (2011c). Noise and contact in dynamic AFM, Proceedings of ASME Design Engineering Technical Conference, IDETC 2011-47955.
- Chakraborty, I. and Balachandran, B.** (2011d). Noise influenced responses of elastic cantilevers with nonlinear tip force interactions. *Proceedings of ASME International Mechanical Engineering Congress and Exposition*, IMECE 2011-63207.

- Chakraborty, I. and Balachandran, B.** (2012). Near-grazing dynamics of elastic structures with nonlinear tip interactions, accepted for publication, *Nonlinear Dynamics*, (2012)
- Chin, W., Ott, E., Nusse, H. E., and Grebogi, C.** (1994). Grazing bifurcations in impact oscillators. *Physical Review E* **50**(6): 4427-4444.
- Dankowicz, H.** (2006). Nonlinear dynamics as an essential tool for non-destructive characterization of soft nanostructures using tapping-mode atomic force microscopy. *Philosophical Transactions of Royal Society A* **364**: 3505-3520.
- Dankowicz, H. and Nordmark, A. B.** (2000). On the origin and bifurcations of stick-slip oscillations. *Physica D* **136**: 280-302.
- Dankowicz, H., Zhao, X., and Misra, S.** (2007). Near-grazing dynamics in tapping-mode atomic-force microscopy, *International Journal of Nonlinear Mechanics* **42**: 697-709.
- de Weger, J., van de Water, W., and Molenaar, J.** (2000). Grazing impact oscillations. *Physical Review E* **62**(2): 2030-2041.
- Derjaguin, B. V., Muller, V. M., and Toporov, Y. P.** (1975). Effect of contact deformations on the adhesion of particles. *Journal of Colloid and Interface Science* **53** (2): 314–326.
- di Bernardo, M., Budd, C. J., and Champneys, A. R.** (2001a). Normal form maps for grazing bifurcations in n-dimensional piecewise-smooth dynamical systems. *Physica D* **160**: 222-254.
- di Bernardo, M., Budd, C. J., and Champneys, A. R.** (2001b). Corner collision implies border collision bifurcation. *Physica D* **154**: 171-194.
- di Bernardo M., Feigin, M. I., Hogan, S. J., and Homer, M. E.** (1991). Local analysis of C-bifurcations in n-dimensional piecewise-smooth dynamical systems, *Chaos, Solitons and Fractals*, **10**(11): 1881–1908.
- Dick, A. J., Balachandran, B., Yabuno, H., Numatsu, M., Hayashi, K., Kuroda, M., and Ashida, K.** (2009). Utilizing nonlinear phenomena to locate grazing in the constrained motion of a cantilever beam. *Nonlinear Dynamics* **57**(3): 335-349.

- Dick, A. J.** (2007). Advantageous utilization of nonlinear phenomena in microstructures and macro-structures: applications to micro-resonators and atomic force microscopy. *Ph. D. Dissertation, University of Maryland.*
- Garcia, R. and Perez, R.** (2002). Dynamic atomic force microscopy methods. *Surface Science Reports* **47**: 197-301.
- Gardiner, C. W.** (1983) Handbook of Stochastic Methods, Springer, Heidelberg.
- Hashemi, N., Dankowicz, H., and Paul, M. R.** (2008). The nonlinear dynamics of tapping mode atomic force microscopy with capillary force interactions. *Journal of Applied Physics* 103(9): 09351.
- Hu, S. and Raman, A.** (2006). Chaos in atomic force microscopy. *Physical Review Letters* **96**: 036107.
- Hunt, J. P. and Sarid, D.** (1998). Kinetics of lossy grazing impact oscillators, *Applied Physics Letters*, **72**(23): 2969–2971.
- Ing, J., Pavlovskaja, E., Wiercigroch, M., and Banerjee, S.** (2008). Experimental study of impact oscillator with one-sided elastic constraint. *Philosophical Transactions of Royal Society A* **366**: 679–704.
- Kowalewski, T. and Legleiter, J.** (2006). Imaging stability and average tip-sample forces in tapping mode atomic force microscopy. *Journal of Applied Physics* **99**: 064903.
- Lee, S. I., Howell, S. W., Raman, A., and Reifenberger, R.** (2002). Nonlinear dynamics of microcantilever in tapping mode atomic force microscopy: A comparison between theory and experiment. *Physical Review B* **66**: 115409.
- Lee, S. I., Howell, S. W., Raman, A., and Reifenberger, R.** (2003). Nonlinear dynamic perspectives on dynamic force microscopy. *Ultramicroscopy* **97**: 185-198.
- Legleiter, J.** (2009). The effect of drive frequency and set point amplitude on tapping forces in atomic force microscopy: simulation and experiment. *Nanotechnology* **20**: 245703.

- Long, X. H., Lin, G., and Balachandran, B.** (2008). Grazing bifurcations in elastic structures excited by harmonic impactor motions. *Physica D* **237**(8): 1129-1138.
- Molenaar, J., de Weger, J. G., and van de Water, W.** (2001). Mappings of grazing impact oscillators. *Nonlinearity* **14**: 301-321.
- Nayfeh, A. H. and Balachandran, B.** (1995). Applied Nonlinear Dynamics: Analytical, Computational and Experimental Methods. *John Wiley and Sons Inc.*
- Nordmark, A. B.** (1991). Non-periodic motion caused by grazing incidence in an impact oscillator. *Journal of Sound and Vibration* **145**(2): 279-297.
- Rajaram, R., Salapaka, M. V., Basso, M., and Dahleh, M.** (2000). Experimental study of stochastic resonance in atomic force microscopes. *Proceedings of the American Control Conference.*
- Ramakrishnan, S. and Balachandran, B.** (2010). Energy localization and white noise induced enhancement of response in a micro-scale oscillator array. *Nonlinear Dynamics* **62**: 1-16.
- Raman, A., Melcher, J., and Tung, R.** (2008). Cantilever Dynamics in atomic force microscopy. *Nanotoday* **3**(1-2): 20-27.
- Rutzel, S., Lee S. I., and Raman, A.** (2003). Nonlinear dynamics of atomic-force-microscope probes driven in Lennard Jones potentials. *Proceedings of Royal Society A* **459**: 1925-1948.
- Shaw, S. W. and Balachandran, B.** (2008). A Review of nonlinear dynamics of mechanical systems in year 2008. *Journal of System Design and Dynamics* **2**(3): 611-640.
- Shaw, S. W. and Holmes, P. J.** (1983a). A periodically forced piecewise linear oscillator. *Journal of Sound and Vibration* **90**(1): 129-155.
- Shaw, S. W. and Holmes, P. J.** (1983b). Periodically forced linear oscillator with impacts: chaos and long-period motions. *Physical Review letters* **51**(8): 623-626.

- Solares, S. D (2007).** Single biomolecule imaging with frequency and force modulation in tapping-mode atomic force microscopy. *Journal of Physical Chemistry B* **111**: 2125-2129.
- Stark, R. W., Drobek, T., and Heckl, W. M. (2001).** Thermomechanical noise of a free v-shaped cantilever for atomic-force microscopy. *Ultramicroscopy* **86**: 207–215.
- Stensson, A. and Nordmark, A. B.(1994).** Experimental investigation of some consequences of low velocity impacts in the chaotic dynamics of a mechanical system, *Philosophical Transactions of the Royal Society A*, **347**(1683): 439–448.
- van de Water, W. and Molenaar, J. (2000).** Dynamics of vibrating atomic force microscopy. *Nanotechnology* **11**: 192-199.
- Yagasaki, K. (2004).** Nonlinear dynamics of vibrating microcantilevers in tapping-mode atomic force microscopy. *Physical Review B* **70**(24): 24541.